2009

Applying scanning probe microscopy for the investigation of molecular self-assembly mechanisms and properties of designed nanomaterials

Algernon Tremayne Kelley
Louisiana State University and Agricultural and Mechanical College, akell14@lsu.edu

APPLYING SCANNING PROBE MICROSCOPY FOR THE INVESTIGATION OF MOLECULAR SELF-ASSEMBLY MECHANISMS AND PROPERTIES OF DESIGNED NANOMATERIALS

A Dissertation

Submitted to the Graduate Faculty of the
Louisiana State University and
Agricultural and Mechanical College
in partial fulfillment of the
requirements for the degree of
Doctor of Philosophy

in

The Department of Chemistry

by
Algernon Tremayne Kelley
B.S., Xavier University of Louisiana, New Orleans, 2004

December 2009

DEDICATION

I dedicate this dissertation in memory of my mother, Ethel Pearl Kelley-Roach, and my father, Hezekiah Roach. I miss you both dearly, but I know that you are always with me in my heart. I would also like to dedicate this dissertation to Bishops Willie Hardy and Clarence J. Turner, two true men of God who taught me that nothing is impossible if I keep God first and foremost in my life. To my fiancée, Amanda K. Martin, and my brothers (Antrone, An'dre, Adrian, Alden, and Averill Kelley), I thank all of you for your unwavering support. I also cannot forget to thank Paul E. Quintyne and Dr. Saundra Y. McGuire for giving me words of encouragement and for always believing in me since we met. And lastly, I dedicate this to all family members and friends who have helped me along the way and to the many unnamed heroes who paved the way for me to have this opportunity. Again, I say, thank you.

ACKNOWLEDGEMENTS

First, I would like to give honor to God for blessing me to achieve this wonderful milestone in my life. God has truly been my strength and my shield throughout this process. Next, I would like to thank my research adviser, Dr. Jayne C. Garno, for the guidance she has provided throughout my time at LSU. I will always cherish the time I spent working under your direction. Many a great opportunity has come my way while being a student in your research group. Dr. Garno, you have played an instrumental role in molding my interests in the fields of surface science and scanning probe microscopy. For this and many other things, I say thank you.

I would also like to thank Dr. Tommie Royster, Senior Research Scientist at the Eastman Kodak Company (EKC). I am most grateful for the guidance and direction you gave me during my six-month internship there in Rochester, NY. Additionally, I would like to acknowledge everyone else I worked with at EKC, most especially Ms. Essie Calhoun, Chief Diversity Officer and Director of Community Affairs, for supporting my National Organization of Black Chemists and Chemical Engineers (NOBCChE) Fellowship, as well as Mr. John Bryant, Mrs. Jill Fornalik, Mrs. Paula Alessi, and Mr. Peter Bessey. Lastly, I would like to recognize Mr. Kenneth Johnson and his entire family for making my time in Rochester memorable and for making me and Amanda feel at home.

To Mom and Dad: I thank God everyday that I was blessed to have you as my parents. Even though you are gone, I will always love you and cherish the wonderful memories I have of you. As I now reflect on the many lessons that you both taught me, one lesson in particular stands out: "Whatever you do in life, even if it is sweeping the floor, do it to the best of your ability." I have applied and will continue to apply this lesson to everything that I do in life. As the first doctor on both sides of our family, my achievement is the fruit of your labor of love. To the "A-team", my brothers Antrone L. Kelley, An'dre H. Kelley, Sgt. Adrian D. Kelley, Alden D. Kelley and Averill D. Kelley: Thank you so much for all of your support and for always being a phone call away. Even though neither of our parents ever went to college, our mother always dreamed that, one day, every one of her boys would go to work wearing a white collar shirt and tie with a briefcase in hand. This personal triumph—and our collective triumphs as a whole—is evidence that we are making her dream a reality.

To my fiancée, Amanda Martin (soon-to-be Amanda M. Kelley on 6/12/2010): You have been with me throughout all of my years in graduate school. In addition to giving me your heart, you have also given me your ear whenever I needed to vent about my problems and concerns. You have also given of your time, and you have always encouraged me to keep going (even when I wanted to quit). On many occasions, you have been my backbone when things became almost unbearable.

Thank you for supporting my dream and for sacrificing getting married for three years so that I could achieve this goal. No words can describe my true appreciation. Thank you, and I love you. Love always, your teddy bear (ALA).

To Paul E. Quintyne, Vernon E. Martin, Jr., and Ronald N. Roberts: Since high school, you have all served as my mentors, role models, and my friends. Thank you for all of your support, encouragement, and most of all, for being there no matter how bad things in life became. Aside from my parents, siblings, and other close relatives, the three of you have helped me to become who I am today. In particular, I have to thank you, Paul, for always being someone I could count on to listen, give sound advice, and for treating me as more than just your mentee. In many ways, you served as a father figure, especially after my biological father died. Thank you for making me feel like a son.

To my Xavier University of Louisiana "family": Thank you for teaching me that what matters most is not how you start the race, but that you actually finish the race. Ten years ago, most would have never thought it possible that a "poor black boy from Connecticut" could go to college, start off in remedial math, reading, and English, and graduate with honors in chemistry along with Xavier University's highest honor, to boot. With your help, I not only accomplished all of these things, but have also been able to obtain a Ph.D in chemistry. When others said it was impossible, God made it happen. I would like to especially recognize Professors Maryam Foroozesh, Janet Ann Privett, Warren Ray, Kris Norenberg, J.W. Carmichael, Michael Adams, John Sevenair, and Ms. Reed for exposing me to research and for taking the extra time to teach me the fundamentals of science. Time would fail me to name every individual who has touched my life at this prestigious institute of higher learning. Nevertheless, please know that I will never forget you and will forever appreciate all that you have done for me.

I would like to thank my graduate school committee members, Professors Kermit Murray, Saundra McGuire, Graca Vicente, Lowell Urbatsch, and Julia Chan for serving on my committee and for always having time to talk to me about research or whenever I needed to vent. I would also like to thank Dr. Isiah Warner, Dr. Bilal El-Zahab, and his graduate student, Aaron Tesfai, for collaborating with me in my research. Thanks also goes to Professor Indrajith Senevirathne for imaging many of my nanoparticle samples and for all of the helpful discussions we had during your tenure in our lab.

I am most grateful to all former and current members of the Garno research group—Wilson Serem, Stephanie Daniels, Dr. Johnpeter Ngunjiri, Dr. Jie-Ren Li, Zorabel LeJeune, Kathie Lusker, Jill Fitzgerald, and Dr. Brian Lewandowski—for their help during my time at LSU. I would also like to acknowledge all undergraduates who worked on the various research projects I conducted:

Nickolaus Flurry, Bryan Brown, Craig Sabottke, Shawn Harrington (designing microwave nanoparticles), Edugie Omoregbee (formation of template strip gold), Treva Brown, Lauren Williams (nanografting of alkanethiols), Glenys Castro, Robert Singleton (characterization of nanoparticles and quantum dots), and Clinton Bize (imaging pattern silanes).

Being a graduate student is only for a season, but true friendship will last for a lifetime. This is the best way to sum many of the meaningful friendships I made during my graduate school career. Four special friends I would like to recognize at this time are Dr. Steven O. Lawrence, Aaron Brothers, and Jerimiah Forsythe and Joni Stuart, MD. You have always been there for me whenever called upon, and each of you has shown me in your own way what true friendship really means. Steve, more than anyone else, you have really been there for me, especially during my crazy move to and from New York. And of course, how could I ever forget our wild driving excursions around Louisiana! Thank you, Steve. To Mr. Arara R. Hughes ("Mr. Roy"): Thank you for the many discussions we had about life, sports, and God. Thank you also for always making sure I stayed in line and for threatening me with that yardstick if I even talked about quitting. Finally, I would like to thank the many members of Greater Emmanuel Apostolic Church and Christ Temple Faith Apostolic Church for your many prayers and words of encouragement. To all friends, family members, associates, and unnamed heroes, thank you for all that you have done for me. I could not be here today without your help.

I would also like to recognize the follow agencies, grants and fellowships for funding. Chapter three was funded by ACS Petroleum Research Fund (PRF G43352-G5), the State of Louisiana Board of Regents, Research Competitiveness Subprogram (LEQSF(2006-09)-RD-A-04) and the National Science Foundation Career Program (CHE-0847291). Chapter four was funded by the State of Louisiana Board of Regents, Research Competitiveness Subprogram, (LEQSF(2006-09)-RD-A-04) and the National Science Foundation Career Program (CHE-0847291). In addition, I would like to thank the Eastman Kodak Company for sponsoring a research internship during 2008. Finally, Chapter five was funded by the National Science Foundation Career Program (CHE-0847291).

Stay blessed and take care,

Algernon T. Kelley

TABLE OF CONTENTS

LIST OF TABLES

LIST OF FIGURES

LIST OF ACRONYMS

16-MHA	mercaptohexadecanoic acid
11-MUA	mercaptoundecanoic acid
11-MUD	mercaptodecanol
AC	alternating current
AFM	atomic force microscopy
DDT	dodecanethiol
DLS	dynamic light scattering
DMF	N,N-dimethylformamide
DMSO	dimethyl sulfoxide
DPN	dip pen nanolithography
HT	hexanethiol
HDT	hexadecanethiol
MHA	mercaptohexadecanoic acid
MUA	mercaptoundecanoic acid
MFM	magnetic force microscopy
MFRM	magnetic resonance force microscopy
MILNPs	magnetic ionic liquid nanoparticles
MSM	magnetic sample modulation
NPRW	nanopen reader and writer
ODT	octadecanethiol
OTE	octadecyltriethoxysilane
PGMEA	propylene glycol monomethyl ether acetate
SAMs	self-assembled monolayers
SPM	scanning probe microscopy
SPL	scanning probe lithography
STM	scanning tunneling microscopy
UPA	ultra size particle analysis
UHV	ultra high vacuum
XRD	x-ray diffraction

ABSTRACT

Scanning probe microscopy (SPM) for conducting surface characterizations of nanomaterials and molecular self-assembly processes is emerging as important contributions in nanotechnology, especially towards the design of molecular electronic devices. Another area of importance is the characterization of the properties of nanomaterials for fundamental understanding of structure-function inter-relationships. Understanding the properties and behavior of molecules and finding approaches to control surface self-organization through nanolithography provides essential information for development of workable applications for nanotechnology.

The first part of the dissertation (Chapters 2 and 3) describes the methodologies of AFM for characterizing molecules and nanostructures produced with scanning probe lithography (SPL), such as AFM-based approaches of nanoshaving and nanografting. Automated software for nanografting and nanoshaving produce local nanopatterned surfaces with properties that can be tailored by selected head group chemistries of self-assembled monolayers (SAMs). The modified surfaces can then be used to develop new nanoscale bioassays and nanodevices, or can be used as building blocks for bottom-up development of photovoltaic thin-film devices. Nanografting can be used to control the vertical orientation of *n*-alkanethiols or α,ω-alkanedithiols to exclusively generate layers with a standing-up configuration. Reactive head groups of SAMs, such as carboxyl and thiol groups, also have a role in surface self-assembly, and changes in experimental parameters of concentration are shown to generate thin films of double layers on Au(111).

The second part of the dissertation (Chapters 4 and 5) presents the application of AFM for characterizations of the arrangement, morphology, and properties of systems of

nanopigments and magnetic metal nanoparticles. For thin films of organic dye dispersions composed of pigment nanoparticles, the stability and spectral properties were examined using AFM as well as other established analytical techniques in Chapter 4. Changes in surface aggregation are clearly revealed in the AFM results. Further, the measurements show a direct correlation between spectral properties and the amount of aggregation for pigment nanoparticles. Overall, the development of new protocols and experiments for nanoscale measurements with AFM provide new capabilities for evaluation of the properties of nanomaterials for commercial pigment nanoparticles.

Investigations of magnetic properties of metal nanoparticles is a new direction for AFM investigations, at the level of characterizing magnetic response at the level of single nanoparticle measurements, as discussed in Chapter 5. Mapping the magnetic response of synthesized magnetic nanoparticles was accomplished using a hybrid AFM imaging mode termed magnetic sample modulation (MSM). Mixtures of iron, nickel and iron(III)-nickel nanoparticles were characterized using dynamic protocols of magnetic sample modulation (MSM) combined with contact-mode AFM imaging. Corresponding changes in size versus the amplitude of vibrational response were clearly detected using MSM mode for nanoparticles as small as 1 nm in diameter. The flux of the external AC-electromagnetic field induced $FeNi_3$ nanoparticles to vibrate, and magnetic response was tracked in MSM amplitude and phase channels using a lock-in amplifier. Changes to experimental parameters, such as driving frequency and AC electromagnetic field strength were systematically investigated with MSM to evaluate the selectivity, sensitivity and detection thresholds for sample characterizations.

CHAPTER 1. INTRODUCTION

The overall focus of this dissertation is to gain insight into the self-assembly processes, properties, and mechanisms of model chemical systems and nanomaterials using scanning probe microscopy (SPM). Scanning probe methods are becoming more prevalent for investigations of surface chemistry because of the dual capabilities for obtaining physical measurements and structural information with unprecedented sensitivity. Scanning probe microscopy imaging modes have been used for the study of chemical and biochemical reactions and for investigation of tip-surface interactions,[1, 2] chemical structures,[3-6] and material properties[7, 8] at the molecular level. The capabilities for studying and controlling processes at the nanoscale with SPM are emerging as valuable assets in both fundamental and applied research. Scanning probe instruments not only provide a means for characterizing samples with unprecedented spatial resolution, but they can also be applied for nanoscale measurements of surface properties and as a nanolithography tool for constructing designed surface arrangements of molecules.[9-11] Fundamental understanding of the interactions of surface reactions provides essential information for developing workable applications for nanotechnology. Scientific developments using SPM are providing a foundation for new technologies in areas such as molecular electronics,[12-14] materials engineering,[15, 16] medical diagnostics,[17, 18] and drug discovery.[19]

At present, SPM methods and SPM-based lithographies are primarily used as research tools in laboratories rather than as high-throughput tools for manufacturing. However, when one considers the impact of present-day microfabrication technologies which led to the computer revolution, one can predict that nanoscale technology in manufacturing will likewise make an impact that will benefit society. For example, a few potential applications of nanoscale technologies are the development of a new generation of chemical biosensors, biochips, drug delivery agents, analysis platforms, and devices for molecular electronics. Nanoscale research

will define new directions in areas of material chemistry, biosensing, biomimetic surfaces, and molecule-based electronics.

Nanoscience broadly means the study and manipulation of matter on length scales ranging from 1 nm to 100 nm. The research presented in this dissertation provides new examples of nanoscience measurements developed with SPM. An important theme that is emerging for nanoscience research is to fully characterize and measure things that are very small, thus pushing detection capabilities to the molecular-level and beyond. A detailed overview of the experimental approaches used for dissertation research is presented in Chapter 2. Combining nanoscale lithography with SPM measurements is a practical strategy for nanoscience research, the extent of which is described in Chapter 3. Chapter 4 describes nanoscale measurements conducted in collaborative research at the laboratories of the Eastman Kodak Company in Rochester, New York. A key strategy of this dissertation research is to combine multiple SPM approaches to develop hybrid instruments and new nanoscale measurements. For example, Chapter 5 provides results with a newly developed SPM imaging mode of magnetic sample modulation (MSM) combined with contact-mode atomic force microscopy (AFM). Chapter 6 provides a prospectus for future directions with nanoscale SPM measurements.

1.1 Experimental Approaches

The second chapter of the dissertation provides details of the experimental approaches for SPM imaging modes used for these studies. The imaging principle, hardware, and instrument operation for contact mode and tapping mode AFM will be explained, as well as the corresponding simultaneously acquired channels of frictional force and phase imaging modes, respectively. The imaging principle for a newly developed magnetic imaging mode using magnetic sample modulation (MSM) will also be described.[20, 21]

A wide variety of methods have been developed for creating arrays of nanomaterials on solid surfaces, such as photolithography,[22] piezoelectric dispensing,[23] soft lithography,[24] microspotting,[25] electron beam lithography,[26, 27] and particle lithography.[28-31] Atomic force microscopy (AFM) has become an excellent tool for producing and viewing ordered arrangements of organic nanostructures on flat surfaces such as Au(111) films. Methods such as nanoshaving and nanografting,[32, 33] tip-induced oxidation,[34] local catalysis,[35] and dip-pen nanolithography (DPN)[36] have been developed to write patterns with nanoscale dimensions. Chapter 2 describes the AFM-based nanolithography approaches of nanoshaving[37] and nanografting[38] which were applied in this dissertation for fundamental investigations of the surface chemistry of *n*-alkanethiols and α,ω-alkanedithiol self-assembled monolayers (SAMs).

Microwave heating has been applied for sample extractions, synthesis, and digestions in general chemistry,[39] organic chemistry,[40-44] inorganic chemistry,[45] physical chemistry,[46] and Anal. Chem.[47-49] laboratory courses. In addition, microwave synthesis is rapidly becoming the method of choice for many medicinal, pharmaceutical, and academic laboratories. For example, the United States Environmental Protection Agency (USEPA) recommends microwave-assisted sample preparation as the "best available technology" for many of its prescribed procedures for the analysis of environmental samples. For analytical chemistry applications, microwaves have been implemented for preparation of samples when using ASTM test methods, to validate and prescribe the benchmark practices, and as the best available technology for standard lab procedures.

Two microwave systems from CEM were purchased for teaching and research applications at LSU. The systems are equipped with carousels of 24-40 sample vessels as well as temperature and pressure control sensors for conducting multiple replicate analyses. Microwave systems also promote the development of *Green* chemistry methods to prevent or

minimize the generation of toxic fumes, chemicals, or wastes to the environment; this is due in part because reactants can be scaled down to very small quantities of acids, solvents, and reagents in comparison to traditional methods. Our goal was to develop creative, modern lab exercises to stimulate the interest and participation of undergraduates in chemistry laboratories and during their research internships. The application of new methods using microwave heating for teaching labs is discussed in section 2.7 and in Appendix A. Moreover, the successful synthesis of magnetic iron(III)-nickel composite nanoparticles using microwave chemistry is described in Chapter 5.

1.2 Applying AFM-based Nanofabrication for Measuring the Thickness of Nanopatterns: The Role of Headgroups in the Vertical Self-Assembly of Ω-Functionalized *n*-Alkanethiols

Methyl terminated *n*-alkanethiols form well-ordered monolayers during solution self-assembly over a wide range of experimental conditions. However, under certain conditions, *n*-alkanethiols with reactive head groups of carboxylic acid or thiol-terminal groups were consistently found to produce patterns with a vertical thickness corresponding precisely to a double layer. To investigate the role of head groups for solution self-assembly, designed patterns of ω-functionalized *n*-alkanethiols were nanografted with systematic changes in concentration. Nanografting is an *in situ* approach for writing patterns of thiolated molecules on gold surfaces by scanning with an AFM tip under high force, accomplished in dilute solutions of desired alkanethiol molecules as explained in Chapter 2, section 2.5. The chain length and head groups (i.e. carboxyl, hydroxyl, methyl, thiol) were systematically varied for the nanopatterns and matrix monolayers. Interactions, such as head-to-head dimerization, influence the vertical self-assembly of ω-functionalized *n*-alkanethiol molecules within nanografted patterns. At certain threshold concentrations, double layers were observed to form when nanografting with head

groups of carboxylic acid and dithiols, whereas single layers were generated exclusively for nanografted patterns with methyl and hydroxyl groups, regardless of changes in concentration.

A sample 3D topography image acquired using AFM in liquid is shown for a pair of nanografted cross patterns (Figure 1.1), composed of 11-mercaptodecanol (11-MUD). The nanopatterns measure 200 nm in width and length, and a structural model is shown at the right. The cross patterns are 0.6 nm shorter than the surrounding matrix SAM of *n*-octadecanethiol.

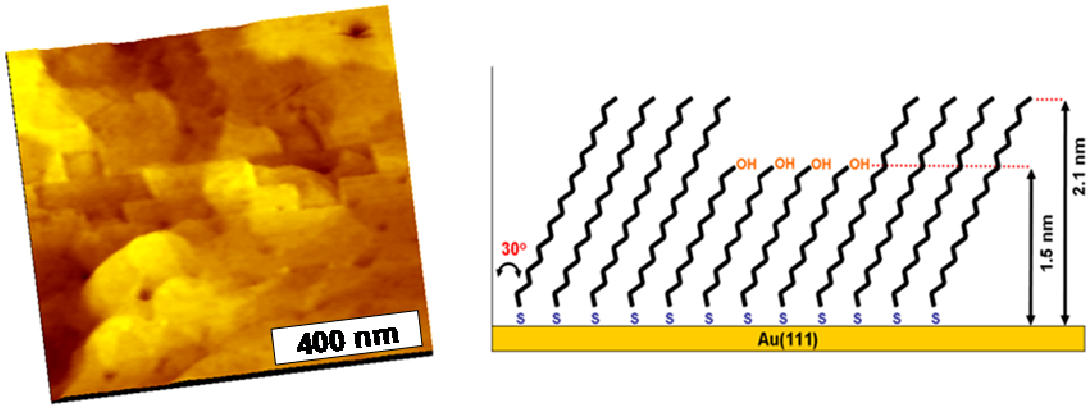

Figure 1.1. Nanografted cross patterns of 11-MUD written into a matrix SAM of octadecanethiol (left) and corresponding structural model (right).

1.3 Investigation and Application of Nanoparticle Dispersions of Pigment Yellow 185 using Organic Solvents

The effects of adding a synergist for the aggregation of pigment nanoparticles in organic solvent dispersions was investigated using AFM imaging and dynamic light scattering (DLS) measurements. The research was conducted at the Eastman Kodak Company research laboratories in Rochester, NY in collaborative research under the direction of Dr. Tommie Royster. Nanoscale AFM characterizations were used to investigate how changes in the surface aggregation of nanoparticles influenced the spectral properties of spin-coated thin films of nano-pigments.

The goal of this investigation was to evaluate the influence of certain dispersants with and without a surface-modifying synergist as well as the influence of solvent polarity on the properties of pigment nanoparticle dispersions. The work focused on spin-coated films of nanoparticles in the size range of 10-30 nm, which is an area not broadly reported for solvent-based systems. A highly stable yellow dispersion with a mean particle size of 12 nm was developed. Characterization of dispersions and nanoparticle films was accomplished using dynamic light scattering (DLS) and tapping-mode AFM. Optical properties of thin films were evaluated with transmission spectroscopy measurements. Optimal performance was achieved using a synergist in combination with a polymeric dispersant and the polar solvent propylene glycol monomethyl ether acetate (PGMEA).

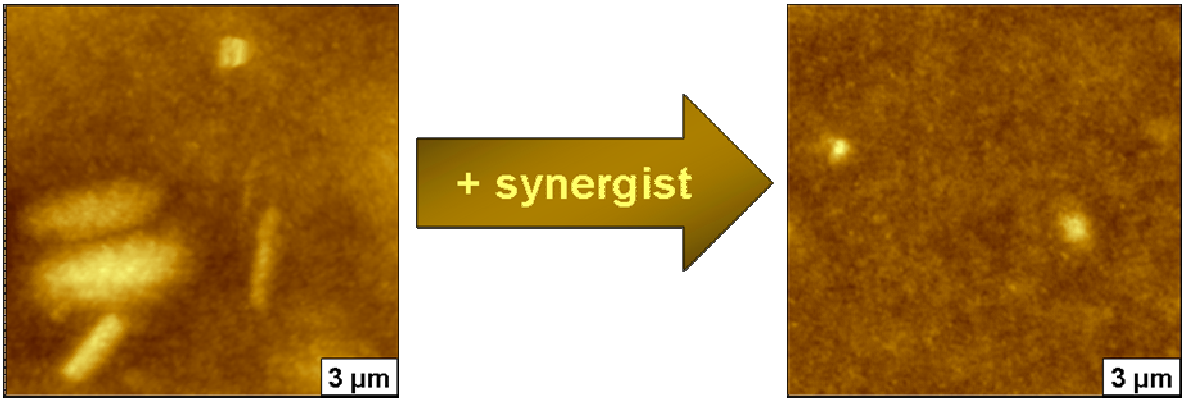

Figure 1.2. Surface morphology of a spin-coated layer of PY-185 pigment nanoparticles on glass with (right) and without (left) synergist, revealed by AFM topography images.

A spin-coated layer of organic dispersions composed of PY-185 pigment nanoparticles and propylene glycol monomethyl ether acetate (PGMEA) coated on a glass surface is shown in the AFM topography image (Figure 1.2), with and without the presence of a synergist. Large clusters of pigment nanoparticles are observed in the left topography image acquired when no synergist added. The right topograph was obtained after the addition of a synergist and reveals that the sizes and amount of nanoparticle clusters are significantly reduced. Self-aggregation of

organic pigment nanoparticles in organic solvents produces poor quality thin-film coatings. The non-uniformity of surface layers produced by dense aggregates within films of nanopigments can be detrimental for light transmission in organic light-emitting diodes (LEDs). Dispersions composed of an organic pigment and an organic solvent must be formulated to minimize self-aggregation for development of high-performance thin films for optical applications, such as LEDs. Comparing the AFM topography images in Figure 1.2 demonstrates that the addition of a synergist can reduce and even prevent the aggregation of pigment nanoparticles. Further experimental results are presented in Chapter 4.

1.4 Response of Iron(III)-Nickel Nanoparticles to a Modulated Electromagnetic Field Detected by Atomic Force Microscopy

Understanding the chemical, magnetic, and physical properties of magnetic nanoparticles is becoming an important research focus. As a model system of composite magnetic metal nanoparticles, samples of $FeNi_3$ nanoparticles were synthesized and characterized, as described in Chapter 5. Magnetic iron(III)-nickel nanoparticles were produced using a hydrothermal process either using a conventional oven or a microwave oven equipped with high pressure Teflon vessels. Microwave synthesis produced magnetic $FeNi_3$ nanoparticles ten-fold faster than conventional radiative heating. Precise control of heating conditions in a microwave digestion vessel was found to produce less polydispersity in the sizes of nanoparticles when compared to samples prepared in a conventional gravity oven. Characterizations with AFM reveal the morphology and size distribution of iron(III)-nickel nanoparticles. Topography and phase images of iron(III) and nickel nanoparticles are displayed in Figure 1.3, acquired using tapping-mode AFM characterizations.

Sample images of $FeNi_3$ nanoparticles prepared on the atomically flat surface of mica(0001) were acquired with tapping mode AFM in Figure 2.4. Frames of the topography and

phase channels are shown for $FeNi_3$ nanoparticles over a $6 \times 6\ \mu m^2$ scan area, for a dilute sample dispersed on mica(0001). A topography image acquired in ambient air is shown in Figure 1.3A with a z-scale of 15 nm, and the simultaneously acquired phase image is shown in Figure 1.3B.

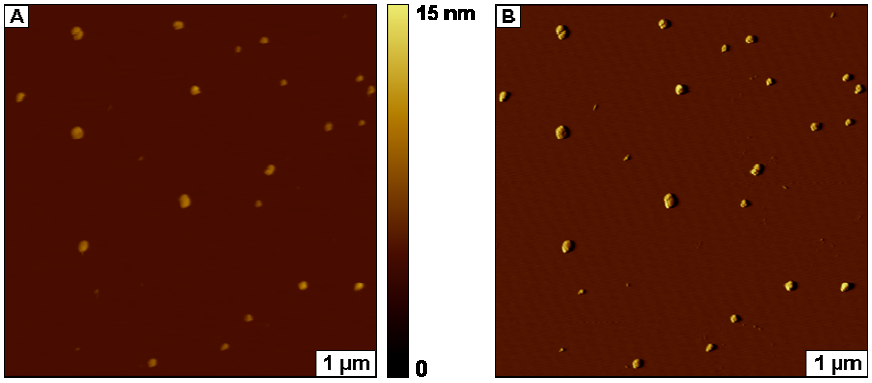

Figure 1.3. Surface views of $FeNi_3$ nanoparticles dispersed on mica[0001], acquired in air using tapping-mode AFM. [A] Topography [$6 \times 6\ \mu m^2$] and [B] simultaneously acquired phase images obtained in ambient air.

The overall goals of the dissertation research were to obtain fundamental insight about the structure, properties, and self-assembly of designed nanomaterials and organic thin films by developing and applying methods of scanning probe microscopy. High resolution SPM imaging and measurements were applied to characterize and visualize processes of chemical self-assembly, surface properties, and nanoscale lithography.

CHAPTER 2. EXPERIMENTAL APPROACHES

2.1 Overview and History of Scanning Probe Microscopy

Methods of scanning probe microscopy (SPM) are emerging as an important and valuable approach for investigations of chemical reactions on surfaces[50, 51] and properties of nanomaterials.[52, 53] Scanning tunneling microscopy (STM) was invented in 1982 by Binnig and Rohrer[54] who were awarded the 1986 Nobel Prize in Physics for this discovery. A conductive or semiconductive surface is required for STM imaging, which relies on the effect of electron tunneling to create atomically-resolved images. In 1986, Binnig, Quate, and Gerber introduced the atomic force microscope (AFM),[55] which can be used to image insulating surfaces and does not require current for the imaging mechanism. Atomic force microscopy (AFM) is a high-resolution imaging technique that enables views of surfaces in great detail. Unlike traditional optical microscopes, AFM techniques use a sharp probe affixed to a cantilever to "feel" the surface, therefore the resolution is not limited by the wavelength of light. The interactions between the tip and the sample are recorded and processed to form an image. The surface structure of materials can be observed in real time on a scale from microns down to nanometers. The lattice arrangement of atoms can be visualized with both AFM and STM, and views of molecular and atomic vacancies can be routinely achieved with STM.

A wide range of different imaging modes have been developed using AFM to characterize the physical properties of samples with nanoscale resolution.[56] In typical contact mode AFM, a sharp tip is scanned across a sample and the deflection of the laser is monitored to provide 3-D information of surface topography.[55, 57, 58] There are several advantages to using AFM compared to other microscopy techniques. Images generated by AFM are true three-dimensional surface profiles. Samples do not require special treatments or coatings which alter their composition, as required for electron microscopy samples. Both conducting and insulating

materials may be imaged. A vacuum environment is not required for AFM imaging, and samples can be imaged in ambient conditions in air or in liquid media. The various AFM imaging modes require certain changes to the instrument configuration, such as oscillating the AFM probe/sample, or changing the positional feedback loop. Rich structural and mechanical information about samples can be obtained for the different imaging modes, such as characterizations of elasticity, adhesion, conductivity, electronic properties, and magnetic forces.[50, 52, 59]

This chapter presents the operating principles for several AFM imaging modes used for the research investigations of this dissertation. The general principles and operation for contact mode, frictional force imaging, tapping mode, phase imaging, and magnetic sample modulation (MSM) AFM are described. Details of the chemistry of self-assembled monolayers and approaches used for AFM-based nanofabrication will be outlined along with synthetic approaches for using microwave heating to prepare metal nanoparticles.

2.2 Contact Mode and Frictional Force Imaging

For contact mode and frictional force AFM, the tip is rastered in continuous contact across a surface using a piezoceramic scanner. A diode laser is focused onto the backside of the cantilever and reflected onto a quadrant photodetector as illustrated in Figure 2.1. A surface profile is generated when the AFM-probe is scanned across the surface in an X-Y raster pattern, and attractive and repulsive forces between the tip and the sample cause the cantilever to bend. As the tip moves up or down or experiences torsional twisting, the position of the reflected laser on the photodetector changes accordingly. Images can be simultaneously generated to view differences in frictional forces experienced by the scanning probe. Contact-mode provides high-resolution images and can be used to resolve features as small as an atomic/molecular lattice, provided that the surface is quite flat.

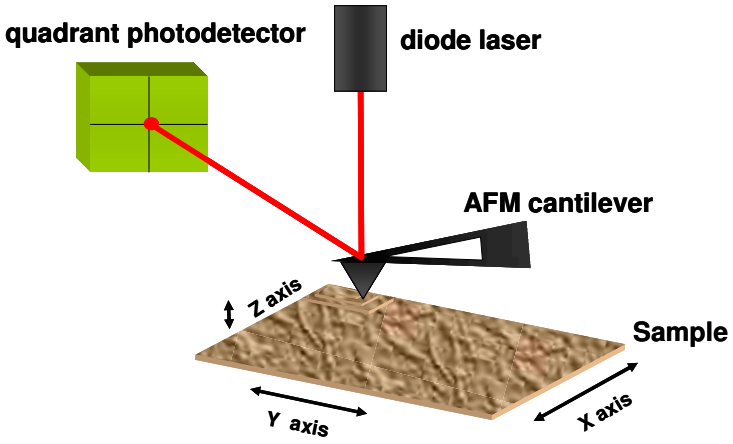

Figure 2.1. Basic imaging principle for contact mode and lateral force AFM.

A feedback loop is used to maintain the initial deflection set-point or load force applied between the tip and sample. For contact mode imaging, the electronic feedback loop adjusts the voltages applied to the piezoscanner to maintain a constant tip deflection. A computer generates a 3-D digital image of the surface topography by mapping the small changes in voltage applied through the feedback loop with the X-Y position of the tip.[55, 60-64]

Nanoscale frictional forces between the tip and the sample produce torsional twisting of the AFM probe as it is scanned across the sample in contact mode. The amount of twisting (detected as changes in the left-right position of the laser signal) is caused by local differences in the surface chemistry of the sample. Lateral force or frictional force microscopy images are acquired simultaneously with contact-mode topography images, which display contrast due to surface friction. Frictional force imaging is useful when studying the homogeneity of sample surfaces and provides a sensitive map of local differences in surface chemistry. Examples of contact mode and lateral force images are shown in Figure 2.2 for a nanopattern 5, 10-bisphenyl-15-20-pyridind-4-yl porphyrin nanografted into a matrix self-assembled monolayer (SAM) of octadecanethiol on Au(111). For the topography frame (Figure 2.2A), the dark areas represent shallow areas and the bright colors correspond to taller features. The image in the center (Figure

2.2B) shows the simultaneously acquired lateral force image. The cross-shaped nanostructure shows clear differences in surface chemistry compared to the surrounding matrix SAM. In the absence of hysteresis, trace and retrace friction images can be digitally subtracted to reveal differences in surface friction for well-aligned scanners.

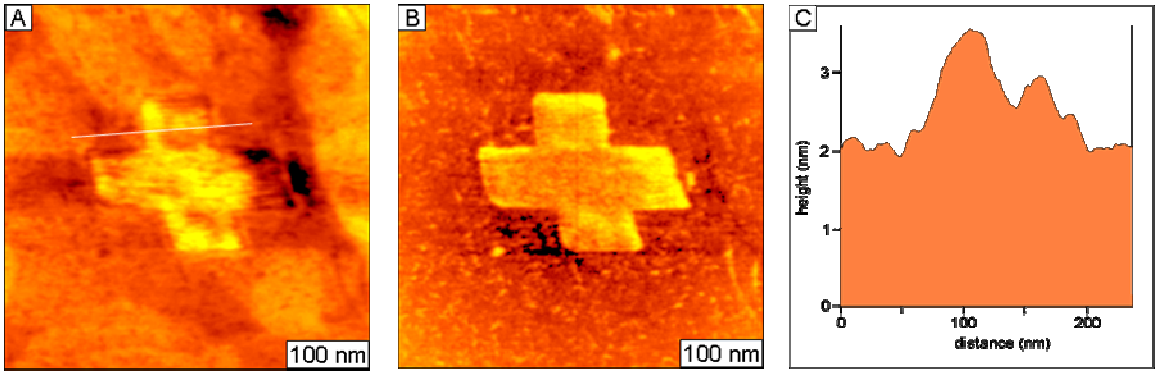

Figure 2.2. Contact and lateral force AFM images of a cross nanopattern of 5,10-bisphenyl-15-20-pyridind-4-yl porphyrin nanografted into an octadecanethiol SAM. [A] Topograph [0.45 x 0.45 μm^2] acquired in ethanol; [B] simultaneously acquired lateral force image; and [C] cursor profile for the line drawn in **A**.

2.3 Tapping Mode AFM and Phase Imaging

Tapping mode uses an oscillating cantilever to minimize stick-slip adhesion during contact between the tip and the sample. A possible drawback of contact mode AFM is that drag forces develop between loosely bound samples and the scanning probe, which can alter or damage the surface under high forces. Tapping mode was developed to overcome this limitation for imaging soft and fragile samples.[65-67] Tapping mode is an intermittent mode of AFM in which the cantilever is oscillated at a certain frequency as it is scanned across the sample. The tip intermittently touches or "taps" the surface as it is scanned. This greatly reduces the dragging forces[68] and is particularly suitable for imaging biological materials.[69-72]

Tapping mode offers advantages for imaging samples that are loosely bound to the surface or for samples that are sticky or fragile. The tip is driven to oscillate at its resonant frequency and is brought close to the sample surface to intermittently "tap" the surface at the

chosen frequency and desired amplitude. For ambient imaging, the typical resonant frequency of tapping mode tips ranges from 160 to 300 kHz, whereas softer tips with resonances below 100 kHz can be used for tapping mode imaging in liquid media. Typically, the tip is attached to a small piezoceramic chip to drive the mechanical actuation for tip vibration (Figure 2.3).

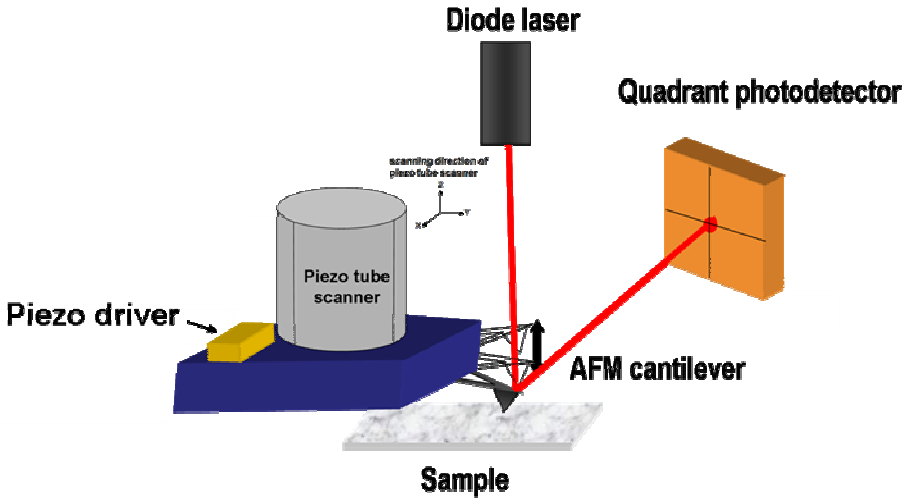

Figure 2.3. Instrument configuration for tapping mode.

As the tip is scanned in intermittent contact with the surface, the feedback loop maintains a constant amplitude of tip oscillation. The voltage changes applied to maintain the amplitude are reconstructed to form an amplitude image. Phase data is obtained from the phase lag between the AC input which drives the oscillation and the cantilever oscillation output. Phase images can be used to view differences in material properties attributable to changes in surface chemistry, adhesion, and softness/hardness properties. Topography, amplitude, and phase data are obtained simultaneously during tapping mode operation. [65, 66, 73-75]

Example images acquired with tapping mode AFM are shown in Figure 2.4. Frames of the topography and phase channels are shown for 100 nm magnetic ionic liquid nanoparticles (MILNPs) over a 20 × 20 μm^2 scan area, for a dilute sample dispersed on mica(0001). A

topography image acquired in ambient air is shown in Figure 2.4A with a z-scale of 110 nm, and the simultaneously acquired phase image is shown in Figure 2.4B.

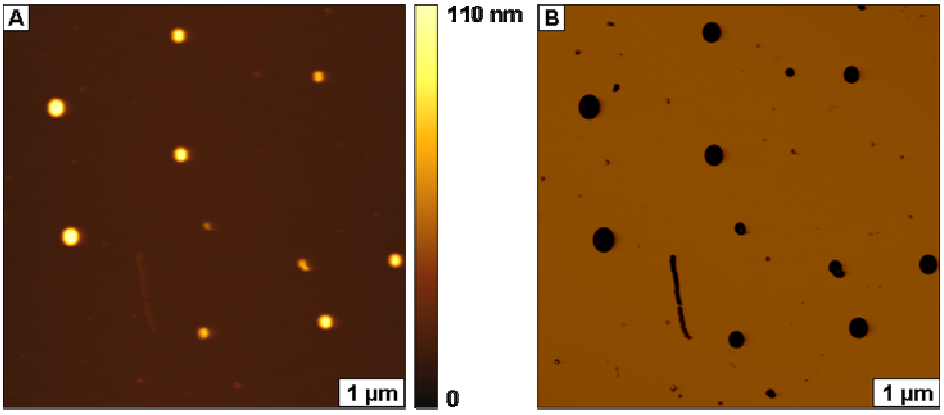

Figure 2.4. Tapping mode images of 100 nm magnetic ionic liquid nanoparticles on mica, acquired in air. [A] Topography 20 x 20 μm^2 and [B] simultaneously acquired phase image.

2.4 Chemistry of Self-Assembled Monolayers of *n*-Alkanethiols and A,Ω-Alkanedithiols

Self-assembled monolayers of *n*-alkanethiols and α,ω-alkanedithiols have been applied for surface modification,[37, 76-78] corrosion inhibition,[79-81] biosensor design,[82-85] and molecular device fabrication.[86, 87] The synthetic flexibility of SAMs provide advantages for designing the chemistry of surfaces with desired spacer lengths and functional groups.[88, 89] Surface properties such as wettability, acidity, and adhesion can be controlled by choosing the functional groups of SAMs. For example, to design the wettability properties of surfaces, SAMs terminated with methyl groups are hydrophobic, whereas SAMs terminated with carboxyl, hydroxyl, or amine groups (moieties that can hydrogen-bond to a polar surface) are hydrophilic.[90, 91] It is well established that SAMs of *n*-alkanethiols form densely packed, well-ordered monolayers on coinage metal surfaces such as gold or silver.[92-95] The packing density of SAMs is shown to change depending on the alkane chain length or terminal chemistry of the molecule.[89]

The basic structure of an *n*-alkanethiol SAM consists of three parts: the tail, the carbon backbone, and the headgroup (Figure 2.5). The tail is composed of thiol molecules for

chemisorptive attachment to surfaces. The thiol is bonded directly to a saturated 2 to 18-carbon chain; the carbon backbone provides a spacer for choosing the vertical thickness of SAM nanopatterns. The carbon chain is capped with a head group which determines the surface properties. A variety of functional groups (esters, alkyls, hydroxyls, carboxylates, amides, etc.) are available, depending on the desired application. Previous reports provide details regarding synthesis, preparation, and characterization of SAMs.[79, 89, 95, 96]

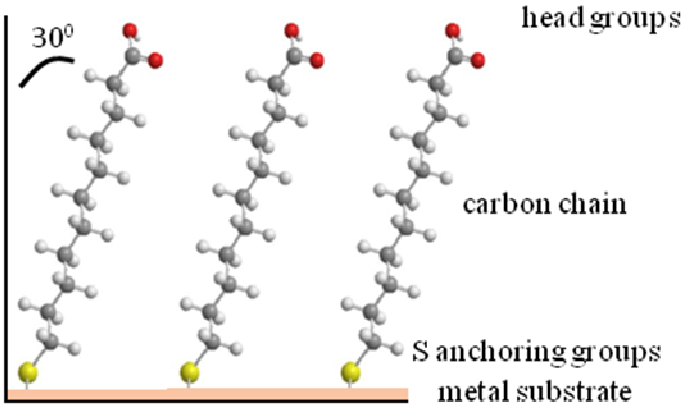

Figure 2.5. General model of a self assembled monolayer on Au(111).

To prepare SAMs of *n*-alkanethiols or α,ω-alkanedithiols, Au(111) substrates are submerged in dilute solutions of alkanethiol dissolved in solvents such as ethanol or 2-butanol for various time intervals. There are a wide range of conditions reported for producing SAMs of methyl terminated *n*-alkanethiols, as summarized in Table 1. The concentration and the amount of time the substrate remains in solution will vary depending on the solubility of the molecule in the chosen solvent and the nature of the SAM headgroups. Controlling variables, such as the solution concentration and intervals of immersion, may inhibit the formation of double layers and ensures sufficient surface coverage to produce mature, densely-packed SAMs.[25] It has also been reported that minimizing exposure to light serves to prevent oxidation of thiols.[97, 98] For UHV studies, vapor deposition has also been used to prepare SAMs.[95, 99, 100]

Table 2.1. Examples of different protocols applied for preparing SAMs.

SAM	Substrate	Concentration (mM)	Time (h)	Temperature (°C)	Solvent	Ref.
n-hexanethiol, *n*-octanethiol, *n*-decanethiol, *n*-dodecanethiol, benzenethiol	Au(111)	0.001 - 1 mM	24 h	25	ethanol	[101]
n-dodecanethiol	Au(111)	1 mM	24-36 h	25	ethanol	[102]
n-hexadecanethiol	Au(111)	0.0002 mM	< 1 h	21	ethanol	[103]
n-octadecanethiol	Au(111)	0.0001 mM	< 1 h	21	ethanol	[104]
n-alkanedithiol	Au(111)	0.01 - 1 mM	12 - 168 h	25	ethanol, 2- butanol	[105]
1,10-decanedithiol	Au(111)	0.1 mM	1 - 24 h	25	2- butanol	[106]

Investigations of the solution self-assembly of α,ω-alkanedithiols on Au(111) were accomplished using contact mode-AFM.[105] Unlike *n*-alkanethiols, SAMs of α,ω-alkanedithiols prepared by solution immersion resulted in a heterogeneous surface morphology.[105] A mixed layer of upright or coplanar molecular orientations with either lying-down or standing-up orientations relative to the substrate was observed in AFM images of α,ω-alkanedithiol SAMs. The majority of α,ω-alkanedithiol molecules were observed to orient to the Au(111) surface with a thickness corresponding to having the backbone of the alkane chain aligned parallel to the surface. Islands of standing molecules were intermixed and scattered throughout the surface. Methyl-terminated *n*-alkanethiols with known dimensions were used as molecular rulers to obtain a relative thickness measurement of α,ω-alkanedithiol SAMs with angstrom sensitivity. Nanopatterns of α,ω-alkanedithiols were shown to directly adopt an upright orientation by nanografting due to spatially constrained self-assembly.[105]

According to studies conducted using IR, near-edge X-ray absorption fine structure (NEXAFS) spectroscopy, and grazing incidence X-ray diffraction (GIXD), the alkyl chains of *n*-alkanethiol SAMs are tilted approximately 30° with respect to the surface normal.[107-111] Thiol atoms of SAMs are considered to bind to the triple hollow site of a Au(111) lattice by chemisorption.[78, 89, 97, 112] The solution self-assembly of *n*-alkanethiol SAMs on bare gold

surfaces is reported to occur in two phases. The stripe phase forms when thiols molecules initially make contact with the gold surface, in which the backbone of the molecules are oriented parallel to the substrate in a lying-down configuration.[113] However, over time the *n*-alkanethiol molecules rearrange into a standing position with the molecular backbone tilted 30^{o} from surface normal.[113] The mature crystalline phase forms an enthalpy favorable, close-packed commensurate $(\sqrt{3} \times \sqrt{3})R30^{o}$ configuration with respect to the Au(111) lattice.[94, 114-116] The exquisite details of the surface structure and long range ordering of *n*-alkanethiol SAMs has been revealed with STM and AFM to enable a direct view of defect sites such as etch pits, steps, and dislocations within films.[94-96] Etch pits are small depressions observed in high resolution images that result from the displacement of atoms of the Au(111) substrate caused by reconstruction when thiols of the alkanethiols bind to the gold surface.

A representative AFM topographic image of a naturally-formed *n*-alkanethiol SAM/Au(111) acquired in liquid is presented in Figure 2.6. High-resolution images obtained with AFM disclose substrates that are not truly smooth and flat; rather, from the atomic perspective, surfaces contain defects such as pinholes, missing atoms, and scars. When AFM images reveal these natural defects, then true molecular or atomic resolution has been achieved. Looking at the AFM images, the surface may appear rather rough and irregular. However, the surface is actually very flat from an atomic perspective. The height of gold steps is only 0.25 nm, and the overall surface roughness of the underlying gold substrates for these samples is less than 1 nm. The topography images in Figure 2.6 display height changes according to color contrast from dark to light, analogous to a height map of the surface terrain. The dark colors indicate shallow features, whereas brighter areas are taller. In the wide view image ($1 \times 1\ \mu m^2$) of an dodecanethiol SAM in Figure 2.6A, the terrace domains of the underlying gold surface are clearly apparent. The AFM image reveal that the step edges of the gold terraces are not smooth;

rather, the uneven and angular profiles at lacey edges reflect the true surface morphology. The SAM-covered surface is decorated with tiny holes, known as etch pits or molecular vacancy islands, which are 0.2 nm deep, corresponding to the depth of one atomic layer of gold. Etch pits are defect sites resulting from the reconstruction of Au(111) during the chemisorption of thiol molecules.[117] A close-up view (500 × 500 nm^2) of a terrace area is displayed in Figure 2.6B, which begins to reveal the molecular domains between areas of etch pits. The size and density of etch pits varies widely for various samples according to sample preparation conditions, such as age and oxidation. Details of the surface morphology of alkanethiol SAMs on Au(111) substrates has also been investigated with STM.[101, 118, 119]

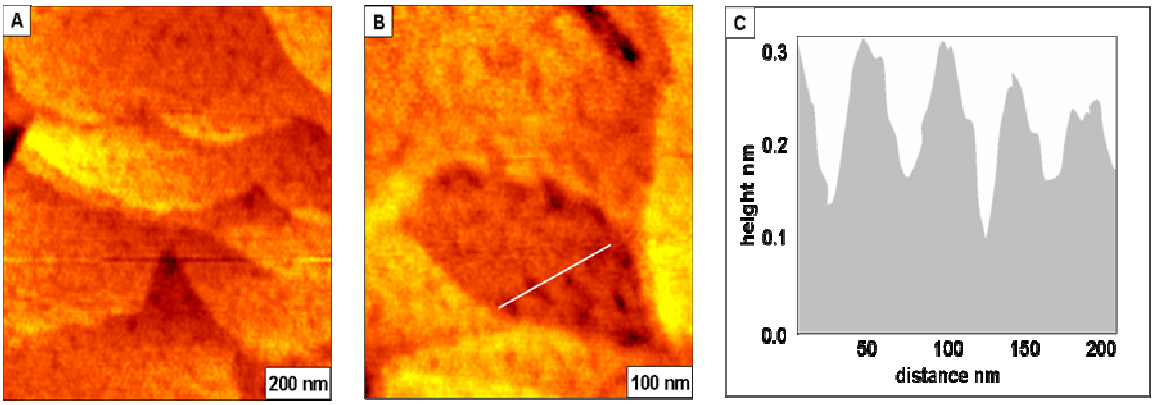

Figure 2.6. Contact mode AFM images of dodecanethiol on Au(111) acquired in ethanol. [A] Topography view of several terrace domains [1 × 1 μm^2] ; [B] zoom in view [C] cursor profile for the line in **B**.

2.5 Approaches for Scanning Probe Lithography

Many promising methods for producing nanostructures of organic thin film materials have been developed, such as x-ray and e-beam lithographies,[120-126] nanosphere lithography,[127-134] and scanning probe-based nanolithography.[9, 135, 136] Scanning probe lithography (SPL) exhibits the highest spatial precision at the level of single molecule resolution. The intrinsic advantages of SPL have triggered rapid developments with approaches advanced for regulating local tip-material interactions to accomplish SPL with biological and organic thin film materials.

Elegant results for manipulating individual metal and noble gas atoms as well as diatomic molecules under cryotemperatures in ultra high vacuum (UHV) using STM demonstrate the atomic-level precision achievable with SPL.[137-140] More commonly, nanoscale lithography using AFM approaches has been used for nanofabrication with SAMs. Examples include tip-directed material deposition,[141] dip-pen nanolithography (DPN),[142, 143] local oxidation nanolithography,[144-146] local chemical or electrochemical lithography,[147] tip-induced catalysis,[148] thermal-mechanical based writing,[149-152] nanoshaving,[37, 153, 154] and nanografting.[38, 155, 156] Recent reviews have furnished in-depth discussions for the SPL approaches of DPN and local oxidation lithography.[142, 143] In comparison to other SPL approaches, STM-based lithography exhibits the highest spatial precision at the level of single organic molecules. Among AFM-based approaches, nanografting and nanoshaving provide *in situ* advantages of high spatial resolution, demonstrating feature sizes as small as 2 nm.[157]

2.5.1. Fabrication of SAMs Using Nanoshaving

Nanoshaving can be accomplished by applying mechanical force to the probe during scans; essentially small areas of the SAM are "shaved" away by the action of a scanning AFM tip.[37] Nanoshaving is used to uncover selected regions of surfaces which are surrounded by a passivating matrix SAM. These uncovered regions are then available for deposition of new molecules and materials. Information about the thickness of molecular layers on surfaces can be derived by using the nanoshaved areas as a baseline for cursor measurements.[38, 158] Nanoshaving was introduced in 1994 for a SAM of octadecyltriethoxysilane (OTE). Changes in the observed lattice were used to confirm that molecules were displaced from the surface.[159, 160]

The process of nanoshaving is accomplished by scanning several times over a small local area of a surface with an AFM tip while applying a higher force than that used for imaging (Figure 2.7). After molecules are removed, the AFM probe can still be used to image the surface

by returning to low force. In nanoshaving, a high local pressure is applied by an AFM tip to the area of contact. This pressure causes high shear forces, and thus displaces SAM adsorbates as the tip is scanned back and forth across the surface. As a result, the bare substrate is exposed. By carefully controlling the amount of force applied, the AFM tip is not damaged during fabrication.

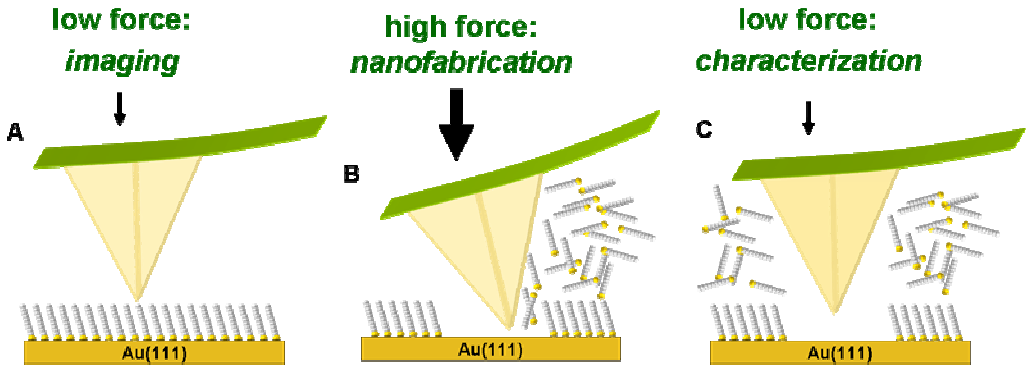

Figure 2.7. Basic steps of nanoshaving. [A] Surface characterization under low force; [B] nanoshaving of local areas of the SAM is accomplished when the force in increased; [C] returning to low force, the nanoshaved area can be characterized *in situ*, using the same tip.

The three basic steps of nanoshaving are shown in Figure 2.7. The first step uses an AFM tip operated under minimal force (less than 1 nN) to characterize the sample and to locate a suitably flat, clean area for writing. A flat plateau area of the surface with few scars and defects is desirable for shaving patterns. Next, a higher force is applied (ranging from 2-20 nN depending on the monolayer adsorption properties), which causes the AFM tip to push through the matrix SAM to make contact with the surface. The molecules directly under the tip are shaved away to uncover areas of the surface. Sufficient force is applied to the AFM probe to ensure that matrix SAM molecules are removed without disturbing the underlying gold substrate.[37] In the final step, the newly fabricated areas of the surface are characterized with the same AFM tip using a reduced force (less than 1 nN). Thus, nanoshaving enables *in situ* fabrication of SAMs.

It is critical to optimize the amount of force applied to the AFM tip for nanoshaving SAMs. If too much force is applied, the sharp apex of the tip can be broken. Therefore, it is important to find a minimum force to remove molecular layers without damaging the tip. Atomic force microscope controllers provide precise control of the force applied to AFM tips using electronic feedback. The threshold force is determined for each experiment by successively incrementing the amount of force applied during scans. As the force is increased, the tip is pushed though the matrix SAM to contact the underlying substrate. The tip is then rastered several times to sweep molecules from the surface since the actual area of contact is very small between the tip and surface. If too much force is applied, the torsion on the cantilever will cause the tip to twist and produce non-linear movements. At the optimized minimum force threshold, the desired square, linear, or circular geometries will be produced.

The imaging media and the nature of the molecule influence the success of nanoshaving. When imaging in air, displaced SAM molecules often pile up at the sides of the trenches or holes that are uncovered; in liquid media, the molecules dissolve in the surrounding solvents. Nanoshaving has not been accomplished for *n*-alkanethiols with fewer than ten carbons because holes or trenches refill with short-chain molecules. Immediately after the molecules have been removed by the scanning AFM tip, molecules of short-chain thiol SAMs backfill into the uncovered areas. In contrast, SAMs of any chain length of *n*-alkylsilanes are irreversibly displaced by nanoshaving in either liquid or ambient environments.[160, 161]

An example array of nanoshaved patterns produced within an octadecanethiol (ODT) SAM is presented in Figure 2.8. The topographic image displays twelve dark squares written into an ODT matrix in ethanol. The squares correspond to uncovered areas of Au(111). The areas of brighter contrast indicate taller features, whereas the dark areas are shallower. Even when writing with an open-loop AFM scanner, there is very precise alignment of the rows and

columns of the array and well-defined square geometries for nanoshaved patterns. The high-resolution image of Figure 2.8A was acquired after nanoshaving and evidences that, after writing under force, the tip has not become blunt or damaged. The *in situ* topograph clearly exhibits the indicators of a high-resolution image, such as circular gold terraces, concentric circular steps, and line scars. The friction image (Figure 2.8B) provides a spatial map of the changes in chemistry for nanoshaved patterns. The matrix areas of ODT show uniform contrast, which is clearly distinguishable from the brighter nanoshaved areas. Within the nanoshaved squares, the homogeneous color evidences clean removal of the matrix SAM. A cursor profile along the bottom row of nanoshaved patterns reveals the height difference between the ODT SAM and the underlying surface measures 2.0 ± 0.2 nm. This value agrees closely with the expected thickness (2.1 nm) for an ODT SAM.

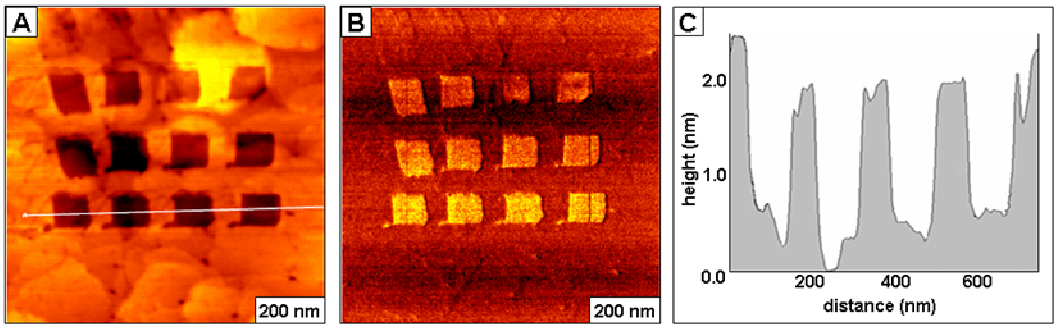

Figure 2.8. Nanoshaved array of 100 x 100 nm^2 squares written in an octadecanethiol matrix. [A] topography; [B] frictional force image; [C] corresponding cursor profile along the bottom row of nanopatterns.

The thickness of the SAM can be measured from cursor profiles across the film and areas of the uncovered substrate. Nanoshaving can be applied to determine the thickness of thin films with angstrom precision by referencing the substrate as a baseline for cursor measurements. In addition to alkanethiol SAMs, nanoshaving has been used for characterizations of molecularly thin films of porphyrins,[162] alkylsilanes,[159, 163, 164] sexithiophene,[165] dimercaptobiphenyl multilayers,[166] α,ω-alkanedithiols,[105] and DNA.[167] After local areas of the surface have been

uncovered by nanoshaving, new molecules or nanomaterials can then be selectively deposited on the exposed areas to form nanopatterns.[168]

2.5.2 Nanografting of *n*-Alkanethiol and A,Ω-Alkanedithiol SAMs

Nanografting was introduced in 1997 by Xu and Liu.[38] A useful analogy for describing AFM-based lithography is to consider the AFM tip as a pen, a matrix SAM on gold as the paper, and fresh *n*-alkanethiols in solution as the "ink" for writing patterns. Nanografting basically uses the same procedure as nanoshaving, except that the steps are accomplished while the tip and the sample are immersed in a dilute solution of thiol molecules chosen for writing (Figure 2.9). The matrix SAM is first characterized in liquid media by applying a low force, less than 1 nN. Imaging in liquids enables one to achieve high resolution with low, nondestructive forces.[169, 170] After choosing an area for writing, a greater force (1-10 nN) is applied to the AFM tip (*pen*) to shave the matrix molecules from the gold substrate. The SAM molecules which are removed from the surface (*paper*) are either deposited at the edges of the nanopatterns or are dissolved in the surrounding solvent. New thiol molecules from solution immediately self-assemble onto the shaved areas following the scanning track of AFM tip. The written patterns can then be characterized *in situ* without changing tips by returning to low force.

For nanografting, it is critical to control the amount of force to ensure that the tip remains sharp after writing nanopatterns. Unfortunately, the microfabrication processes used to manufacture tips have not yet achieved nanoscale reproducibility for the shape and spring constants for each lever, thus, an *in situ* approach is useful to derive the optimized threshold force for each AFM tip. To optimize the writing force, a simple computer script can be used to write several patterns at incrementally increasing force. The lowest force at which a complete pattern is observed is then chosen as the optimized force for nanografting. When too much force

is applied to the AFM probe while scanning, it is possible to scratch away the underlying surface or to break the apex of the probe. If the selected threshold force is too great, the torsion on the cantilever will cause the tip to write irregular shapes and produce stray lines and marks around the patterns.

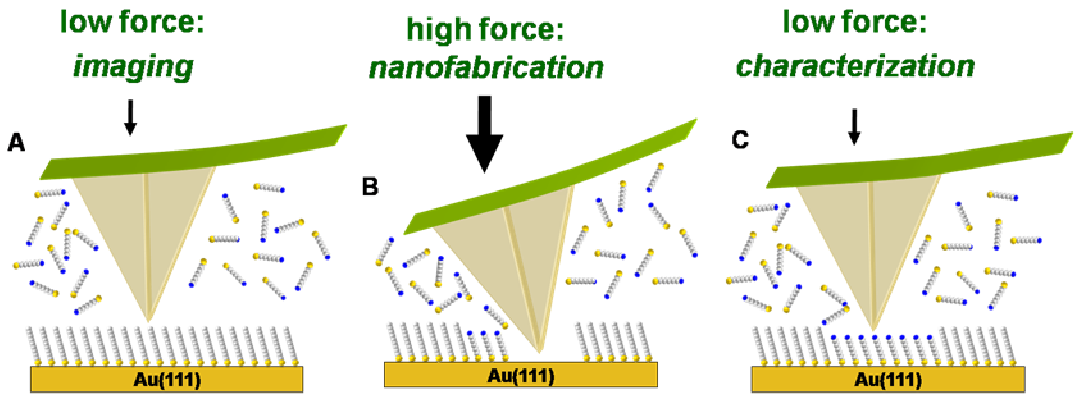

Figure 2.9. Principle of nanografting. Molecules self-assemble from solution following the scanning track of an AFM tip.

When a minimum force is used for nanografting, hundreds of patterns can be written with the same AFM tip without sacrificing topographic resolution. In fact, often the resolution of AFM imaging is improved by the sharpening process or cleaning of the tip by scratching the surface.

Depending on the choice of molecules, nanografting can generate patterns that are taller or shorter than the SAM matrix. For example, a cross-shaped pattern of 11-mercaptoundecanol (MUD) was written into matrix of ODT in Figure 2.10A. The simultaneously acquired frictional force image exhibits dark contrast for the MUD areas of the cross, which are terminated with hydroxyl groups (Figure 2.10B). The surrounding methyl-terminated matrix areas of ODT exhibit lighter frictional contrast, clearly distinguishing the differences in surface chemistry after nanografting. The line profile of Figure 2.10C indicates the nanostructure is 0.7 ± 0.3 nm shorter than the matrix SAM, in close agreement with the theoretical differences in thickness (ODT measures 2.1 nm, MUD is 1.5 nm). The measurements of film thicknesses with nanografting are

highly dependent on the flatness of the surface; in this example, the error term for the nanografted domains take into consideration the roughness of gold step edges (± 0.25 nm).

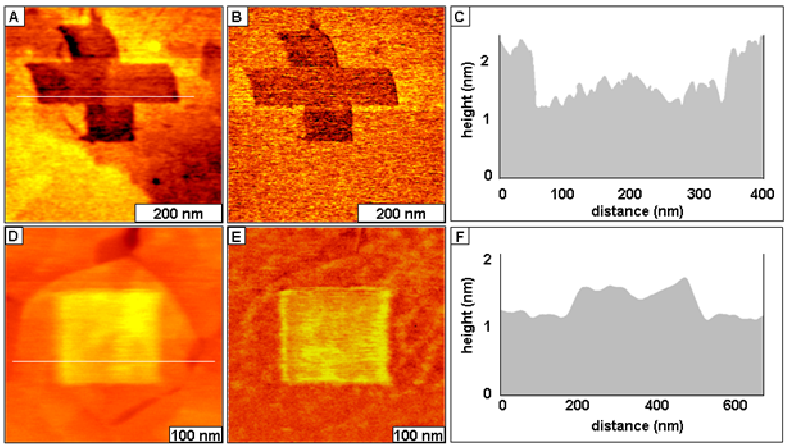

Figure 2.10. Nanografted patterns of self-assembled monolayers. [A] Cross-shaped pattern of 11-mercaptoundecanol fabricated within a matrix of octadecanethiol; [B] corresponding frictional force image; [C] cursor profile for the white line in **A**. [D] Mercaptohexadecanoic acid forms a taller pattern within a dodecanethiol matrix, the square has bright contrast; [E] friction image; [F] cursor profile across the nanopattern in **D**.

An example is presented for a positive height pattern of 16-mercaptohexadecanoic acid (MHA) in Figure 2.10D. The square nanopattern (200 x 200 nm^2) was written within a dodecanethiol matrix and is well-centered on a terrace step of Au(111). The friction images provide additional information about the chemical changes on the surface which have taken place after writing new molecules (Figure 2.10E). The corresponding friction image shows bright contrast for the carboxylic acid areas of the square pattern, whereas the surrounding methyl-terminated matrix has dark contrast. There is adhesion between the tip and surface of the square nanopattern, which caused line spikes only on the patterned area along the horizontal direction of the scanning AFM tip. The line artifacts are clearly visible in the friction image. In contrast, the methyl-terminated areas do not exhibit the stick-slip adhesion because the methyl groups do not interact as strongly with the tip. The expected thickness for MHA is 1.9 nm, and

for dodecanethiol, it is 1.5 nm. A representative cursor profile (Figure 2.10F) indicates that the pattern is 0.4 ± 0.2 nm taller than the molecules of the matrix, in close agreement with the theoretical height difference. An attribute of the nanografting process with thiol SAMs demonstrated with these examples is the extraordinary angstrom to nanometer precision for edge resolution, even when using open-loop feedback for electronics. Such well-formed regular geometries at the square edges and corners of patterns are routinely achievable with AFM because the piezocontrollers enable exquisite control of small forces applied to the tip.

A key element of nanografting is that *n*-alkanethiols chemisorb spontaneously to surfaces in an upright arrangement to form a crystalline phase, due to a mechanism of spatial confinement.[171] When *n*-alkanethiols assemble naturally, there is a phase transition from a side-on orientation, with the backbone of the molecule oriented along the surface, to a standing orientation in which the molecules adopt a tilted orientation as in Figure 2.5.[95, 100, 113] When nanografting, it is thought that the molecules bypass the lying-down phase and assemble immediately into a standing configuration because there is not sufficient space for the molecules to assemble on the surface in a horizontal direction.[171] A kinetic Monte Carlo model of natural and nanografted deposition of alkanethiols on gold surfaces was developed by Ryu and Schatz, which reproduces experimental observations for the variation of SAM heterogeneity with AFM tip writing speed.[172] The speed of the AFM tip influences the composition of the monolayers formed along the writing track.

2.6 Magnetic Sample Modulation AFM

This section describes a new approach for mapping the magnetic response of nanomaterials by combining magnetic sample modulation (MSM) with contact mode AFM. Several measurement SPM modes have been developed for evaluating magnetic properties of samples. Imaging modes, such as magnetic resonance force microscopy (MRFM)[173-176] and

magnetic force modulation (MFM),[177-180] require the use of tips with a magnetic coating. In contrast to magnetic force microscopy, MSM imaging requires using nonmagnetic probes and evaluates the mechanical response of materials vibrating in response to an external magnetic field to map magnetic domains. This new MSM imaging mode has the potential to advance the resolution of magnetic imaging beyond that which is currently possible with MFM.

This new imaging MSM mode uses a standard soft, nonmagnetic AFM cantilever operated in contact mode to detect the physical motion of nanoparticles which are driven to vibrate by an externally applied AC electromagnetic field. Magnetic probes can be problematic, however, since the magnetic properties of the thin metal films which coat the underside of the probes diminish over time, requiring remagnetization. Also, after continuous contact mode scanning, the thin metal films can be worn away. The thickness of the magnetic coatings is on the order of tens of nanometers, which greatly decreases the resolution for imaging small surface features. Intrinsically, the resolution of SPM methods depends on the geometry of the coated probe; metal coatings produce relatively large, blunt tips.

A solenoid is placed underneath the sample stage, as shown in Figure 2.11. When an AC current is applied to the wire coil solenoid, a magnetic field is produced which alternates in polarity. The flux of the alternating magnetic field causes the magnetic nanomaterials to vibrate on the surface according to the desired frequency of the AC current. The periodic motion of the sample vibration can be tracked by changes in the deflection of the tip. As the tip is rastered across the surface in contact mode, the movement of the magnetic nanomaterials causes the tip to vibrate when it touches the vibrating domains. The mechanical motion of the magnetic material is sensitively detected by a scanning AFM tip. Only the magnetic materials vibrate when the alternating magnetic field is applied, providing contrast that is selective for magnetic areas.

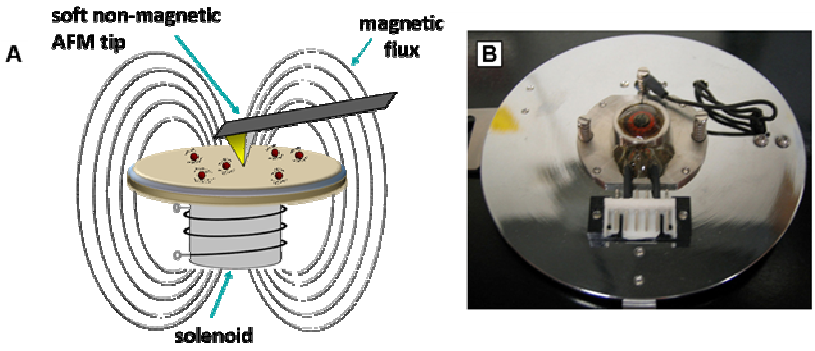

Figure 2.11. Concept for AFM imaging with magnetic sample modulation. [A] Instrument setup; [B] photograph of solenoid located beneath the sample plate.

The instrument setup for MSM is a hybrid mode composed of elements of three AFM imaging modes. The tip is operated in contact mode using a MAC mode sample plate to apply an alternating magnetic field for selective modulation of magnetic domains. Essentially, MSM is a variant of force modulation AFM with selectivity for actuating and characterizing magnetic nanomaterials. To visualize the magnetic domains of a sample, conventional contact mode images are first acquired without applying a magnetic field. Next, the same area of the surface is scanned again with an alternating electromagnetic field applied. The polarity, oscillation, and flux of the magnetic field are generated and controlled by selection of parameters for the AC current applied to the wire coil solenoid, which is located underneath the sample plate embedded within an epoxy resin shown in Figure 2.11 B. When an electromagnetic field is applied to samples, only the magnetic domains are driven to vibrate, providing selective contrast for areas that are in motion. A lock-in amplifier is used to acquire the amplitude and phase components of the deflection signals, which furnishes exquisite sensitivity for slight changes in tip movement. The changes in phase and amplitude as the tip interacts with the vibrating sample are plotted as a function of tip position to create MSM phase and amplitude images. The differences displayed for images with and without an applied magnetic field are used to map areas of magnetic nanomaterials.

Magnetic sample modulation was applied to characterize $FeNi_3$ nanoparticles synthesized using conventional oven heating.[181] Figure 2.12 showcases proof-of-concept MSM images of $FeNi_3$ nanoparticles. A topography image of nanoparticle sample prepared on a mica(0001) surface is shown in Figure 2.12A, and the simultaneously acquired MSM-amplitude and MSM-phase channels are displayed in Figures 2.12B and 2.12C, respectively. The top portion of the images was acquired when an alternating magnetic field was activated. However, after scanning halfway, the electromagnetic field was turned off. Therefore, at the bottom region of the MSM images, no phase or amplitude changes are apparent without the actuation of the external electromagnetic field. Topography images which are acquired by scanning in continuous contact with the surface reveal the presence and shape of nanoparticles regardless of whether an external magnetic flux is applied. Nevertheless, for phase and amplitude channels, sample contrast can only be detected when the samples are vibrating in response to the AC magnetic flux. The MSM images reveal that nanoparticles stopped shaking immediately after the magnetic field is halted.

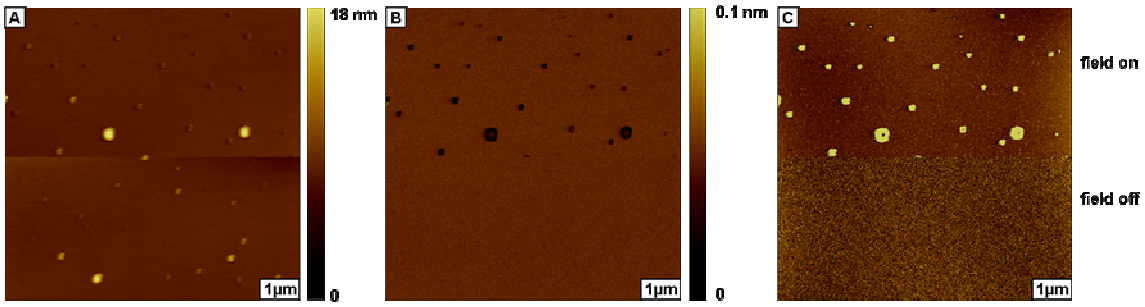

Figure 2.12. Images of $FeNi_3$ nanoparticles in response to the presence or removal of an externally applied AC electromagnetic field. [A] Topography view (6.5 x 6.5 μm^2), [B] MSM-amplitude, and [C] MSM-phase channel.

2.7 Synthesis of Nanoparticles with Microwave Heating

The advanced technology of microwave heating is readily available in most homes and restaurants in the United States, and it seems sensible to use microwaves in our chemistry laboratories. Microwaves are widely used commercially in industrial and research labs because

they are fast and efficient. Many organic solvents and chemicals produce dangerous vapors which can ignite or explode when heated. Microwaves for chemistry are designed with explosion-proof safety features and use computer-controlled fiber optic temperature and pressure sensors to carefully regulate reaction conditions. On the other hand, chemistry microwaves are extremely efficient, producing higher percentage yields in a matter of minutes for reactions that conventionally would require many hours or days to evolve, and reach completion using a hot-plate. The benefits of using microwave ovens for sample preparation and synthesis include improved safety, smaller reagent volumes, speed, increased yields, and cleaner Green chemistries.

Our goal was to implement microwave heating for undergraduate chemistry laboratories and research internships and to develop more efficient, safe, and rapid approaches for sample digestions, extractions, and synthesis.

For example, a laboratory exercise for the analysis of heavy metals in cereals using atomic absorption spectrophotometry was developed using microwave heating for acid digestion. The microwave method was accomplished with only twenty minutes of heating, using far smaller amounts of concentrated solutions of acids in sealed vessels as compared to the hot-plate approach which required heating open containers of boiling hot liquids that evolved acid fumes. The full details of the experiments that were developed are described in Appendix A. In addition, students were encouraged to incorporate microwave protocols in their senior research projects for Chemistry 4553. For example, one group of students studied the leaching effects of heavy metals from alumina, copper, and cast iron cooking pots and used microwave heating to extract metal leachates from food prepared in metal pans.

Microwave systems were also used for graduate student research. In particular, synthesis of $FeNi_3$ nanoparticles was accomplished using microwave heating to control the size dispersity,

and these results are discussed in Chapter 5. Iron and nickel nanoparticles synthesized using microwave heating were imaged with tapping mode AFM (Figure 2.13). Topography and phase images are shown for a 4 × 4 μm^2 scan area, revealing the spherical shape and compositional differences of Fe, Ni, and $FeNi_3$ nanoparticles. The topography image (Figure 2.13A) with a z-scale of 12 nm and corresponding phase image (Figure 2.13B) were acquired in ambient conditions using tapping-mode AFM. A height histogram generated from cursor line profiles of individual nanoparticles reveals polydisperse sizes for the mixture of different nanoparticles (2.13C). Further AFM characterizations comparing the size and composition of nanoparticles prepared by oven heating in a digestion bomb versus nanoparticles prepared with microwave heating in a controlled pressure vessel are described and characterized in Chapter 5.

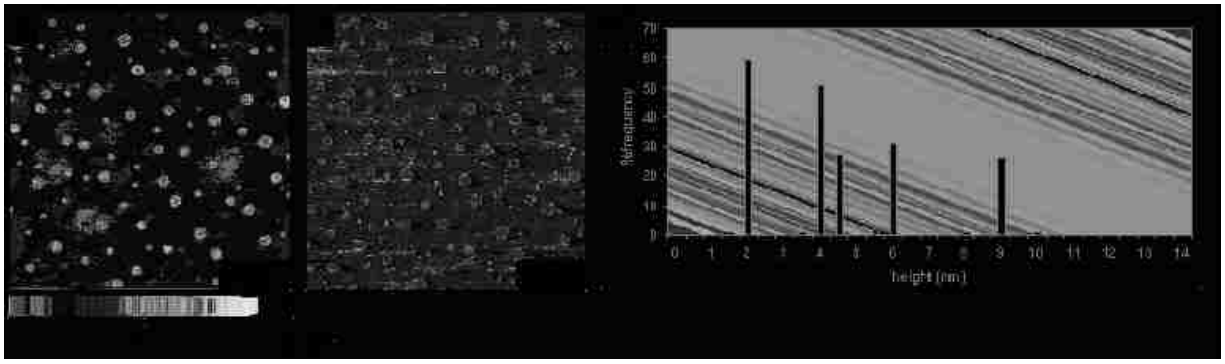

Figure 2.13. A mixture of iron and nickel nanoparticles was produced by microwave heating at low pressure. [A] AAC-mode topograph; [B] corresponding phase image; [C] size distribution of nanoparticles.

CHAPTER 3. APPLYING AFM-BASED NANOFABRICATION FOR MEASURING THE THICKNESS OF NANOPATTERNS: THE ROLE OF HEADGROUPS IN THE VERTICAL SELF-ASSEMBLY OF Ω-FUNCTIONALIZED *N*-ALKANETHIOLS

3.1 Introduction

Methyl-terminated *n*-alkanethiols have been extensively studied and are known to form well-ordered commensurate monolayers over a wide range of experimental conditions (e.g. concentration, immersion intervals).[89, 94, 182-184] However, self-assembled monolayers (SAMs) with hydroxyl, sulfur and carboxylic acid head groups have not been as extensively investigated. By using solutions containing two different alkanethiols, it is possible to generate SAMs of mixed composition.[185-193] Little is known at the molecular level about how the relatively bulky head groups of ω-functionalized *n*-alkanethiols influence the vertical self-assembly for SAM nanopatterns. Alkanethiol SAMs have a number of applications such as for surface modification,[37, 76, 194, 195] corrosion inhibition,[79, 196, 197] chemical or biosensing platforms,[198-202] lubrication[203-207] and molecular device fabrication.[208, 209] The synthetic flexibility of SAMs provide advantages for designing the chemistry of surfaces with desired spacer lengths and functional groups.[210] By changing the functional group, surface properties can be controlled, such as wettability, acidity and adhesion.

Useful nanotechnology applications for *n*-alkanethiol SAMs as relief and resist structures for micrometer to nanoscale lithographies have recently emerged. Nanostructures with designed functionality, geometry, and lateral dimensions can be achieved using scanning probe lithography with *n*-alkanethiols, such as with approaches of nanografting,[211, 212] NanoPen Reader and Writer (NPRW),[213] or DPN.[214] At larger micrometer dimensions, SAM structures can be produced using methods such as microcontact printing and photolithography.[215-220] To produce nanostructures of *n*-alkanethiol SAMs, nanografting was introduced in 1997 by Xu and Liu.[38] For writing nanopatterns with nanografting, a high force is applied to a scanning AFM probe to

remove small areas of the matrix SAM. The exposed areas are immediately filled with molecules from solution to inscribe structures within a matrix SAM along the track of the scanning AFM tip.[221] Nanografting takes place under spatially confined conditions which direct the surface assembly of molecules directly into an upright orientation, bypassing the lying-down phase.[222] Small areas of the surface that are exposed by the AFM tip during nanografting are confined by both the AFM tip and the neighboring thiol molecules of the surrounding matrix; thus, incoming alkanethiols are written directly in a standing orientation. Since nanografting is accomplished in dilute solutions of thiolated molecules, a range of different solvents and concentrations can be examined to evaluate the resulting changes in the vertical self-assembly of nanopatterns.

Mature SAMs with methyl head groups form an enthalpy favorable, close-packed $(\sqrt{3}\times\sqrt{3})R30^{o}$ surface structure and also $c(4\times2)$ superstructures as a crystalline chemisorbed phase which is commensurate with the Au(111) lattice.[94, 210, 223] The thiol end groups are considered to mostly bind to triple hollow sites of a Au(111) lattice by chemisorption.[79, 89, 194, 224] For methyl-terminated *n*-alkanethiol SAMs, studies conducted using IR, near-edge X-ray absorption fine structure (NEXAFS) spectroscopy and grazing incidence X-ray diffraction (GIXD), indicate that the alkyl chains of SAMs are tilted approximately 30° with respect to surface normal.[207, 223, 225, 226] For SAMs with different head groups, the molecular-level packing is known to be different as compared to methyl terminated *n*-alkanethiols with the same backbone. For example, SAMs with hydroxyl and carboxylic acid groups exhibit a higher degree of disorder and different chain orientation.[227, 228] For SAMs with aldehyde-termini, the surface morphology is reported to exhibit a smaller domain size, a lesser degree of long-range order, large coverage of disordered areas, and higher density of missing molecules and other point defects within domains of closely packed molecules.[229] These structural differences are mainly attributed to the strong dipole-

dipole interactions among the aldehyde head groups. It has been proposed that disorder is produced by interactions among the head groups, which can disrupt close-packing at the molecular level.[227, 228]

In the present study, we systematically investigate the influence of concentration parameters for nanografting *n*-alkanethiols with –COOH, –SH, –OH and $–CH_3$ head groups. Nanografting provides an *in situ* approach to investigate the vertical self-assembly of molecules in a liquid environment at various concentrations. Essentially, the well-known dimensions of methyl-terminated alkanethiol matrix SAMs provide a molecular ruler for evaluating the thickness of nanografted structures. Changes in the vertical assembly of nanopatterned molecules under varied conditions of solution concentration provide insight on the interactions of head groups for functionalized *n*-alkanethiols.

3.2 Experimental

3.2.1 Materials

Hexanethiol (HT), octadecanethiol (ODT), hexadecanethiol (HDT), 11-mercaptoundecanoic acid (MUA), 16-mercaptohexadecanoic acid (MHA), 11-mercaptoundecanol (MUD), 1,9-nonanedithiol, dodecanethiol (DDT), N,N-dimethylformamide (DMF), 2-butanol, and dimethyl sulfoxide (DMSO) were obtained from Sigma Aldrich (St. Louis, MO, USA) and used without further purification. Ethanol (200 proof) was purchased from AAper Alcohol and Chemical Co. (Shelbyville, KY, USA). Flame-annealed gold coated mica substrates (150 nm thickness) were acquired from Agilent Technologies, Inc. (Chandler, AZ).

3.2.2 Preparation of *n*-Alkanethiol Self-Assembled Monolayers

To prepare SAMs of n-alkanethiols, flame-annealed Au(111) films on mica substrates were submerged in dilute solutions of alkanethiols dissolved in ethanol for time intervals ranging

from 1 to 48 h. The concentration and the amount of time the substrate remains in solution were varied, depending on the solubility of the molecule in the chosen solvent and the nature of the head groups. Controlling variables such as the solution concentration and intervals of immersion prevented double layers from forming and ensures sufficient surface coverage to produce mature, densely-packed SAMs. In preparing SAMs, it has also been reported that minimizing exposure to light serves to prevent oxidation of thiol end groups.[230, 231] After immersion in ethanolic solutions of either HT, DDT or ODT at a concentration of 10^{-7} M for no more than 48 h, the matrix samples of SAMs/Au(111) were stored in fresh solvent in the dark for up to 3 weeks.

3.2.3 Atomic Force Microscopy (AFM)

Experiments were accomplished using contact-mode in liquid with either a hybrid AFM system from RHK or an Agilent 5500 system (Chandler, AZ). For the hybrid system, a PicoSPM scanner from Agilent (Chandler, AZ) was interfaced with electronic controllers and software (XPM Pro v.1.2.1.0) from RHK Technology (Troy, MI). For automated scanning probe lithography, a computer-controlled vector scanning module was used to control the position, force and motion of the AFM tip (VSCAN, RHK Technology).[232] Silicon nitride cantilevers from Veeco Probes (Santa Barbara, CA) with a 0.5 N/m force constant were used for AFM-based lithography and imaging. Picoscan v5.3.3 software was used for data acquisition. Digital images were processed with Gwyddion (version 2.9) open source software which is freely available on the Internet and supported by the Czech Metrology Institute.[233]

3.2.4 Nanografting

Nanografting consists of three basic steps (Figure 3.1), which are accomplished *in situ* while the tip and the sample are immersed in a dilute solution of new thiol molecules chosen for writing. A useful analogy for describing AFM-based lithography is to consider the AFM tip as a pen, a matrix SAM on gold as the paper, and fresh *n*-alkanethiols in solution as the "ink" for

writing patterns. First, the matrix SAM is characterized by applying a low force less than 1 nN (Figure 3.1A). A flat area with few defects or scars is chosen for writing the patterns. Next, a higher force is applied to the AFM tip (*pen*) to shave the matrix molecules from the gold substrate (Figure 3.1B). The forces used for writing patterns ranged from 2 – 9 nN for the examples presented in this report. The SAM molecules which are removed from the Au(111) surface (*paper*) are either deposited at the edges of the nanopatterns, or are dissolved in the solvent media. New thiol molecules from solution (*ink*) immediately assemble on the surface following the scanning track of AFM tip. The written patterns can then be characterized in the final step using the same AFM tip by returning to the non-destructive force used in the first step (Figure 3.1C). Beginning with a low concentration (10^{-9} M), the imaging media was successively replaced with higher concentration solutions (up to 10^{-3} M) to evaluate the threshold conditions for producing double layer patterns.

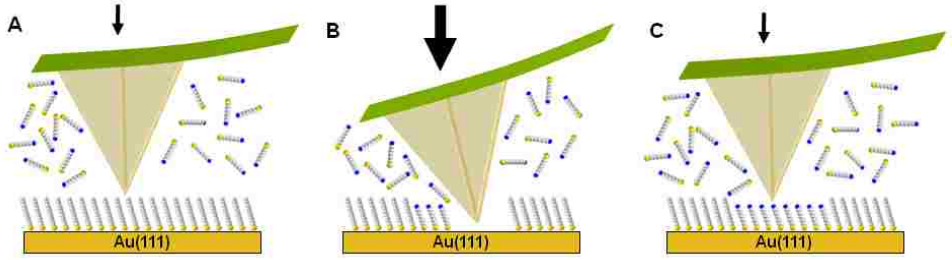

Figure 3.1. *In situ* steps of nanografting. [A] Surface characterization is accomplished while imaging at low force. [B] Nanopatterns are written at high force, thiol molecules assemble in an upright orientation following the scanning track of the AFM tip. [C] Returning to low force, the patterns are imaged *in situ*.

3.2.5 NanoPen Reader and Writer (NPRW)

Nanopatterns of *n*-alkanethiols can be written with NPRW using a coated AFM tip in an ambient environment, as previously introduced by Amro et al.[213] In the first step, an AFM tip is submerged in a 5 mM ethanolic solution of chosen *n*-alkanethiol (ink) for at least 30 min. The thiolated ink molecules adhere to the tip via physisorption, but do not chemically bond to silicon

nitride probes. After the alkanethiol coated probe is removed from solution and dried briefly in air, it is installed on the AFM scanner for imaging. When scanning under low force with the coated probe, the surface of a methyl-terminated SAM is not disturbed and ink molecules remain attached to the tip. Under low force the thiol coating of the tip serves as a lubricant and enables high-resolution imaging to be accomplished.[213, 234] When the force is increased to a certain displacement threshold, nanopatterning is accomplished in air using the same coated probe. Under increased force, matrix molecules directly under the AFM tip are displaced from the substrate and replaced by ink molecules from the tip. The newly inscribed nanopatterns can then be characterized *in situ* by returning to low force for non-destructive imaging. A minimal threshold force for writing is determined by successively increasing the force until nanopatterns are generated with a single pass. By comparing the heights for the matrix SAM of known thickness to the heights of newly inscribed nanopatterns, the local thickness can be measured precisely.

3.3 Results and Discussion

The known dimensions of methyl-terminated *n*-alkanethiols were used as a height reference standard or molecular ruler for comparative measurements of the vertical dimensions of ω-functionalized SAMs (hydroxyl, carboxylic acid, and thiol terminated SAMs). To estimate the heights of *n*-alkanethiols on Au(111), the value for the fully extended molecular length from chemical models of energy minimized structures was determined, and an estimated tilt of 30 degrees was applied to determine theoretical dimensions. Using this approach, the theoretical heights for matrix reference molecules of hexanethiol, dodecanethiol and octadecanethiol are 0.9, 1.5 and 2.1 nm, respectively. The theoretical values are consistent with values reported from experimental measurements using various surface techniques, such as ellipsometry, x-ray diffraction and x-ray photoelectron spectroscopy.[235-238] Nanografting and NPRW provided a

means to generate nanostructures for local thickness measurements, enabling a side-by-side comparison of the heights of ω-functionalized alkanethiols versus matrix monolayers of known dimensions.

3.3.1 Nanografted Patterns with Methyl Head Groups as a Reference Standard

A cross pattern (300 x 300 nm^2) composed of methyl-terminated ODT (10^{-8} M) was nanografted into a DDT matrix (Figure 3.2). The brighter area of the topography frame indicates that the nanografted structure is taller than the surrounding matrix SAM (Figure 3.2A). The cross was written by rastering the AFM tip under high force in the horizontal direction to sweep matrix molecules from the surface with a single pass. The spacing was programmed to advance the tip 2 nm between each linesweep. The cross pattern was written in less than 1 min with a writing speed of 500 nm/second. Since both the matrix and nanopattern are terminated with methyl groups, the lateral force image only reveals subtle differences in surface chemistry at the edges of the nanopattern (Figure 3.2B). Edge effects at the peripheral areas surrounding patterns can often be discerned clearly in lateral force images, which are useful for identifying the local differences in surface chemistry of nanopatterns that were written. Essentially, the tip-surface adhesion for a tip traveling along the side of a molecule is different than when the tip travels across the top surface of the exposed functional group. The lateral force image confirms that the head group chemistry of the matrix and nanografted pattern is the same. A dark circular hole is observed in the upper left region of the nanopatterned cross, which is a pinhole defect of the underlying gold substrate. This landmark is also visible as a bright spot in the corresponding lateral force image. The cursor profile across the center of the cross indicates a height difference of 0.5 ± 0.2 nm (Figure 3.2C). The error term is derived from the height of a Au(111) step (~ 0.24 nm) for the uncertainty of thickness measurements for nanopatterns. The cursor

measurement agrees closely with the expected theoretical values for a close-packed monolayer of *n*-alkanethiols as illustrated in the height model of Figure 3.2D.

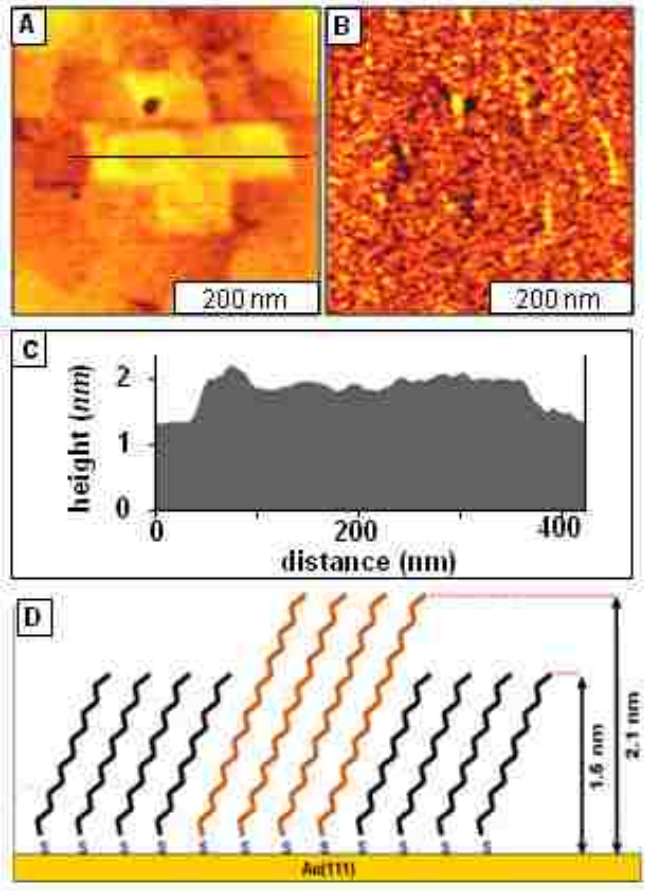

Figure 3.2. A methyl-terminated cross nanopattern written with octadecanethiol in a dodecanethiol matrix. [A] Topography image after writing a pattern via nanografting; [B] corresponding lateral force image; [C] cursor profile for the line in ***A***. [D] Side-view model of molecules of the nanopattern.

Regardless of the concentration of the thiol solution or solvent system chosen, we have observed that methyl-terminated alkanethiols consistently form monolayers when nanografting. Even for concentrations as high as 1 mM, single layers were exclusively produced when nanografting with solutions of methyl-terminated *n*-alkanethiols. Thus, methyl-terminated SAMs provide a convenient, reliable and reproducible height standard for comparative measurements of other systems of ω-functionalized *n*-alkanethiols.

3.3.2 Nanopatterns with Carboxylic Acid Head Groups

For carboxylic acid terminated SAMs, the heights of nanografted patterns were observed to double at higher concentration. A monolayer pattern was produced at relatively low concentration (10^{-9} M) as shown in Figure 3.3A. A cross pattern (300 x 300 nm^2) of MUA was written in ODT with an applied force of 3.4 nN. As expected, the MUA pattern is shorter than the surrounding ODT matrix. The pattern is located on an area which spans three Au terraces; therefore a representative cursor line was selected along a flat area at the upper part of the cross along a single plateau. The MUA pattern is 0.6 ± 0.2 nm shorter than the ODT matrix (Figure 3.3B), which is in agreement with the dimensions expected for a monolayer. A model of the side view of the theoretical heights of the molecules for the cross pattern is presented in Figure 3.3C.

When the concentration of MUA was increased by a factor of ten to 10^{-8} M, nanografted patterns with carboxylate head groups reproducibly formed a double layer in ethanol (Figure 3.3D). Compared to the matrix areas of ODT, a taller height is observed in the topography image of a 4×4 array of nanografted squares (100×100 nm^2), corresponding to the expected thickness of a double layer of MUA. The cursor profile indicates that the nanopatterns exhibit uniform heights, measuring 0.8 ± 0.2 nm taller than the surrounding ODT matrix (Figure 3.3E). This example showcases the capabilities for automation when writing nanopatterns with nanografting, exhibiting nanoscale precision for registry and alignment. Each square of the array was written in ~ 1 min, and the patterns are spaced at regular intervals of 20 ± 10 nm.

For concentrations of MUA below 10^{-9} M, patterns were generated with heights that correspond to a monolayer thickness. At higher concentrations, a double layer forms as a result of head-to-head interactions between carboxylic acid groups. At higher concentration, it is likely that dimers are formed in solution for carboxylate-terminated molecules, which then assemble as a bilayer during nanografting. Layer-by-layer growth was not observed for carboxylic acid

terminated nanopatterns over time, after subsequent prolonged exposure to higher concentrations of MUA, which suggests that dimers formed in solution. For the example of a cross in Figure 3.3A, the *in situ* experiment was monitored in an ethanolic solution of MUA for a period of up to 12 h, to determine if the height would increase with exposure time. Even when the concentration of the imaging media (ODT) was increased 100-fold, the height of the cross pattern did not increase, and a double layer was not observed to attach to the nanografted patterns over time.

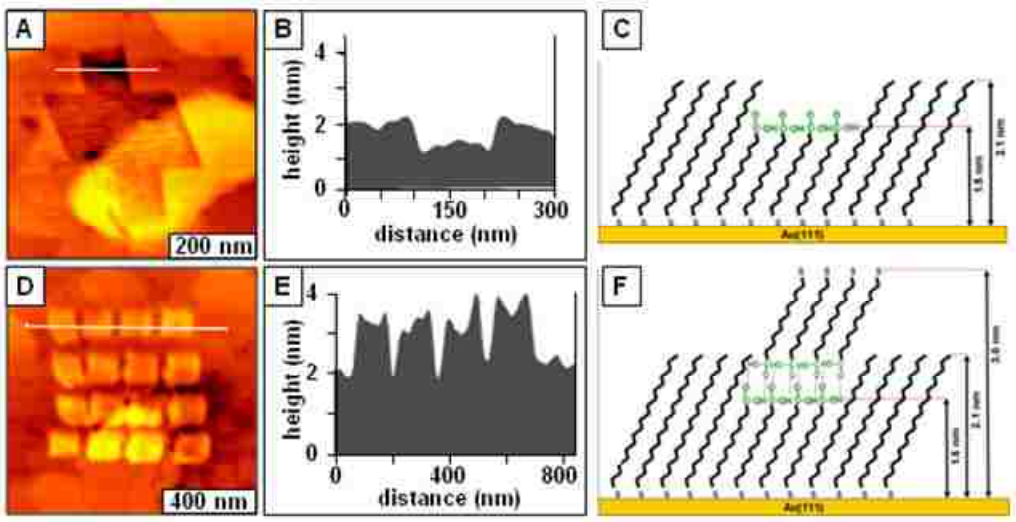

Figure 3.3. Influence of concentration when nanografting carboxyl-terminated SAMs in ethanol. [A] A monolayer pattern of MUA is formed at low concentration. [B] Cursor profile for ***A*** shows the pattern is shorter than the ODT matrix; [C] Model for nanostructure in ***A***. [D] Array of MUA patterns written at high concentration within an ODT matrix; [E] cursor profile for the top row of patterns reveals that a double layer was formed. [F] Model for head-to-head interactions which produce a double layer.

3.3.3 Monolayer or Bilayer Nanopatterns Can Be Formed in Water

Nanografting can be accomplished in aqueous media by adding a small amount of amphiphilic surfactant molecules, such as N,N-dimethylformamide (DMF) or dimethyl sulfoxide (DMSO) to form a mixed solvent.[239] To determine if patterns with double layers are formed when nanografting in aqueous media, a parent solution was prepared by dissolving MUA in DMF. Next, the stock solution was further diluted in deionized water for a final concentration of MUA ranging from 10^{-4} M to 10^{-5} M with less than 1% DMF in water. An array of nanopatterns

of MUA nanografted from aqueous media into an ODT matrix monolayer are presented in Figures 3.4A and 3.4B when using a relatively low concentration (10^{-5} M).

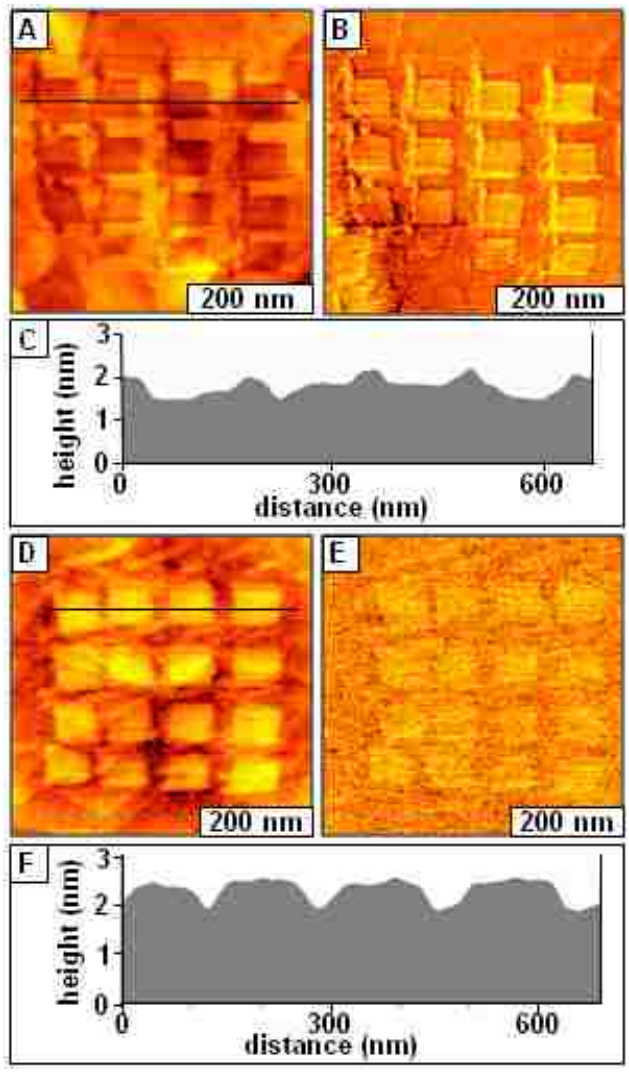

Figure 3.4. Nanografting can be accomplished in aqueous solutions. [A] Topograph of square patterns of MUA nanografted within ODT at low concentration (10^{-5} M); [B] corresponding lateral force image; [C] cursor profile for the white line in ***A*** shows thickness for monolayer patterns. [D] Array of square patterns of MUA nanografted within ODT at high concentration (10^{-4} M); [E] corresponding lateral force image; [F] line profile for ***D*** reveals the pattern thickness corresponds to a double layer

For the nanopatterns in Figure 3.4A, the shapes of 14 patterns are square and regular, while two of the patterns of the array are not clearly inscribed. The missing patterns most likely result from the uneven surface areas at the bottom left corner, which contain deep trenches. The 100 x 100

nm^2 patterns are separated by 30, 40, 50 nm intervals in the horizontal direction, and spaced at 50 nm in the vertical direction. Notice that even at the nanoscale, the rows and columns are aligned in registry with similar interpattern spacing. The programmed distance of 50 nm was not produced precisely, due to the non-linear effects of writing near the furthermost edges of the scan range of the open loop scanner. Stray line patterns measuring 20 x 40 nm^2 were generated at the top left corner of each array element. These regular marks were produced by the sliding movement of the AFM tip as it was placed on the surface. The corresponding lateral force image (Figure 3.4B) exhibits bright contrast for the –COOH terminated areas of the 14 nanopatterns, and the homogeneous color indicates complete replacement of the ODT matrix with nanografted MUA molecules. The cursor profile across the first row of patterns of Figure 3.4A exhibits a thickness which is 0.5 ± 0.3 nm shallower than the ODT matrix (Figure 3.4C), which is consistent with the theoretical difference in chain length for nanografting a single layer of molecules.

As was observed with ethanol solutions, at a certain threshold concentration, double layers of MUA are produced when nanografting in aqueous media (Figure 3.4D). The array of patterns in Figure 3.4D has brighter color in comparison to the ODT matrix, revealing that the nanopatterns are taller than the surrounding SAM. Every pattern of the array formed a double layer, evidencing a reproducible event when nanografting double layers in aqueous media. For this experiment nanografting was accomplished in aqueous solution at 10^{-4} M. All sixteen patterns are visible in the topography image (Figure 3.4D), with uniform and reproducible geometries and heights. The edges of triangular gold steps are visible at the bottom left corner below the patterns, furnishing an *in situ* landmark for height measurement. The locations of the patterns in the lateral force frame are not as clearly distinguishable because adhesion and friction between the tip and surface were minimized when imaging in water. A cursor profile along the

top row of patterns of Figure 3.4D shows the height of the patterns measures 0.6 ± 0.2 nm above the ODT matrix. This correlates well with the expected thickness for a double layer of MUA (Figure 3.4F).

Whether using ethanol or aqueous solutions, double layers are produced at certain threshold concentrations when nanografting with carboxylic acid terminated MUA. For nanografting in aqueous media, the threshold concentration is different than when nanografting in ethanol (10^{-8} M vs. 10^{-4} M). This difference is likely caused by the surfactant effects of DMF in water, which influences the proximity of adjacent MUA molecules in solution. The surfactant serves to lessen the possibility for forming head-to-head dimers of carboxylate groups.

Two orientations are possible for the molecules within the double-layer patterns, either head-to-head or head-to-tail. If head-to-tail conformations were produced, then hypothetically many more successive layers could be formed, which does not match the experimental observations. The AFM results disclose that double layer patterns are produced when using higher concentrations for MUA, which would imply that the exposed groups of the double layer patterns are thiols. The contrast of the lateral force images of Figures 3.4B and 3.4E provide another clue about the nature of the head groups of the nanopatterns. The surface groups of the single layer patterns are known to be carboxylate, yet the contrast of the images in Figure 3.4E are markedly different, even though the images were acquired with the same identical AFM tip and with the same ODT matrix SAM. Since lateral force images reflect changes in adhesive interactions between surface head groups and an AFM tip, matching color contrast would be expected for the nanopatterns if both images present carboxylate head groups at the interface.

3.3.4 Nanografted Patterns Produced with α,ω-Alkanedithiols

To evaluate the vertical self-assembly of α,ω-alkanedithiols, a cross pattern of nonanedithiol (300 x 300 nm^2) was written into a DDT matrix with a concentration of 10^{-6} M in

ethanol (Figure 3.5A). The DDT matrix SAM is only ~0.2 nm taller than nonanedithiol, however the nanografted areas of the cross are easily distinguished in the high resolution topography frame. A few stray marks are apparent in the topograph, indicating areas where the tip was picked up or placed onto the surface under force.

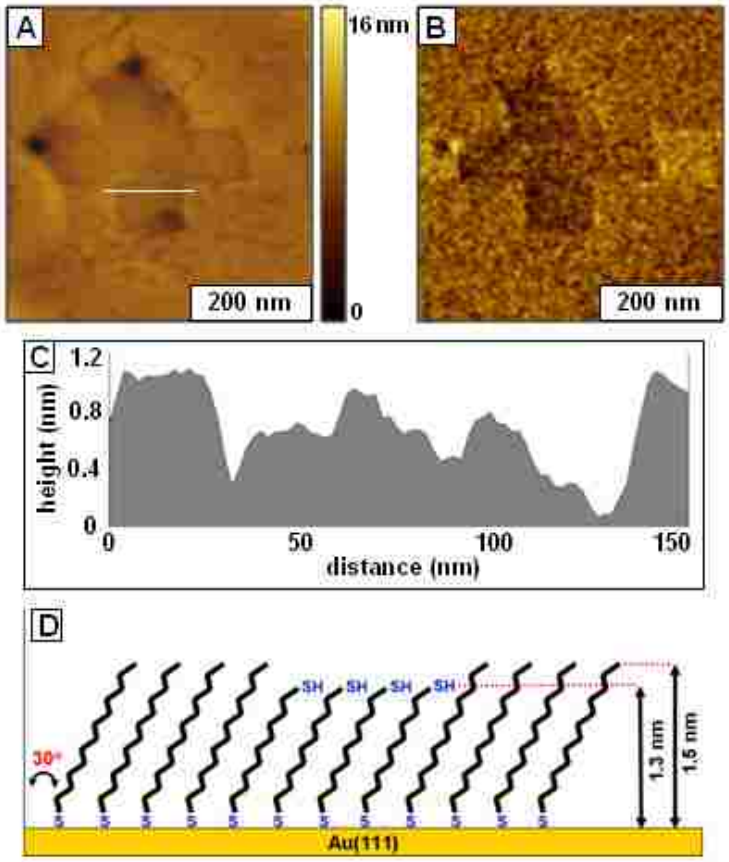

Figure 3.5. A monolayer pattern forms at 10^{-6} M for nonanedithiol when nanografting in ethanol, the pattern is slightly shorter than the dodecanethiol matrix. [A] The shape of the cross pattern viewed with a contact-mode topograph; [B] Simultaneously acquired lateral force image of the nanografted pattern. [C] Cursor for the line in ***A***. [D] proposed height model for nanografting a single layer.

Etch pits or gold vacancy islands are evident on the surface of the DDT SAM surrounding the nanopattern, and three pinhole defects (dark spots) are apparent at the edges of the cross nanopattern. Defects such as holes are commonly observed for evaporated Au(111) thin films, usually tens of nanometers deep. The lateral force image reveals a distinct difference in friction

for the areas within the cross pattern of nonanedithiol compared to the surrounding areas of the DDT matrix (Figure 3.5B). The bright areas of the cross are thiol-terminated, whereas the regions with darker color are methyl-terminated DDT. The cursor profile indicates that the DDT matrix areas are 0.3 ± 0.2 nm taller than the nonanedithiol pattern (Figure 3.5C), which matches well with the theoretical value of a monolayer. A proposed model for the heights of the nanopattern is shown in Figure 3.5D. In this example, the natural roughness of the underlying Au(111) substrate is the same as the expected height difference. Further examples have been published previously for nanografting single layer patterns of α,ω-alkanedithiol SAMs.[105]

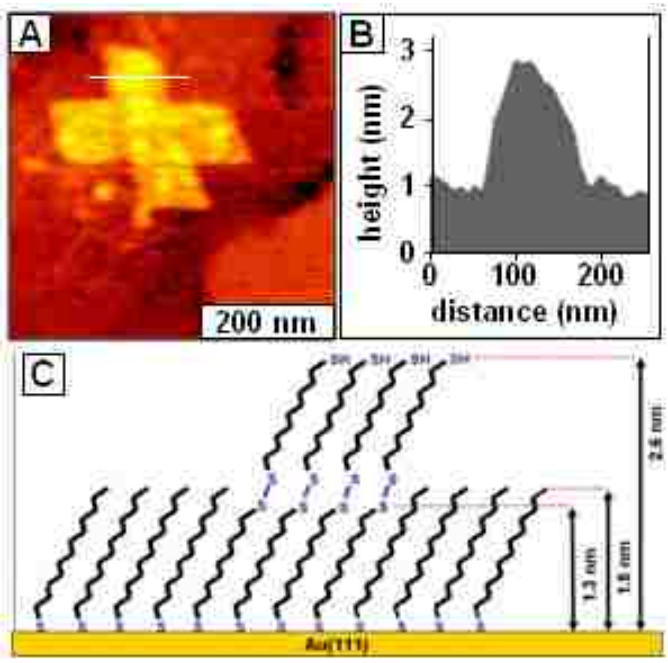

Figure 3.6. *In situ* fabrication of a bilayer nanopattern of an α,ω-functionalized alkanedithiol written within a matrix layer of dodecanethiol. [A] When nanografting at higher concentration (10^{-5} M) nonanedithiol forms a double layer. [B] Cursor profile for ***A***. [C] Proposed model for the double layer.

When the concentration was increased 10-fold to 10^{-5} M, nanopatterns with thicknesses corresponding to a double layer were produced by nanografting with nonanedithiol. The height difference is evident in the topograph of a cross pattern (300 nm x 300 nm^2) composed of nonanedithiol written at higher concentration into DDT (Figure 3.6A). The nonanedithiol pattern

is 1.1 ± 0.2 nm taller than DDT, which extrapolates to a total thickness of 2.6 nm (Figure 3.6B). A molecular model for the height of the double-layer pattern is presented in Figure 3.6C.

An experiment with 1,9-nonanedithiol at high concentration (10^{-3} M) nanografted within a HT matrix is presented in Figure 3.7. Characteristic features of the surface of a mature alkanethiol SAM such as molecular vacancy islands are clearly apparent in the 300 × 300 nm^2 topograph, as well as a staircase arrangement of several overlapping gold steps (Figure 3.7A).

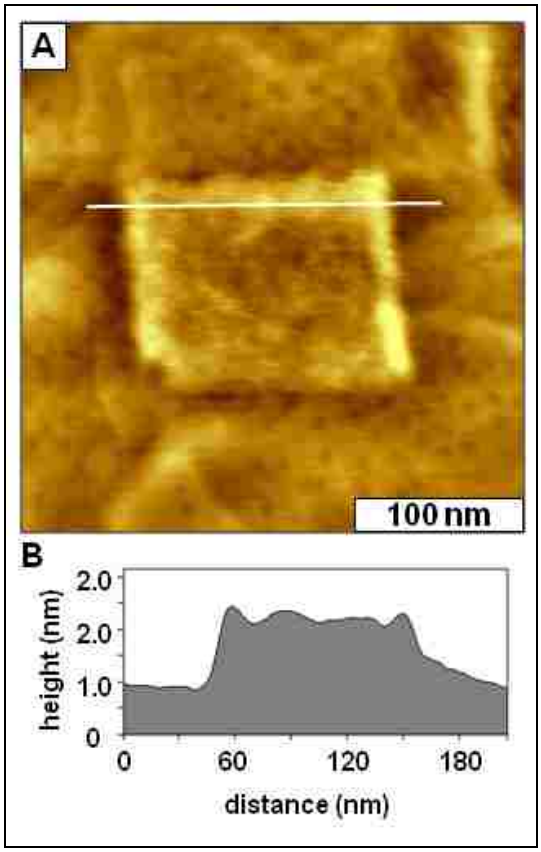

Figure 3.7. Nanografted bilayer pattern of 1,9-nonanedithiol nanografted at high concentration within a HT monolayer. [A] AFM topograph acquired in ethanol; [B] Corresponding line profile across the pattern.

The nanografted pattern measures 160 × 130 nm^2 ($l \times w$) in lateral dimension and is clearly taller than the surrounding HT SAM. A precise measurement of the thickness of the nanopattern is complicated by the presence of multiple step edges near the pattern. The predicted thickness

difference is 1.7 nm between a double layer of nonanedithiol (2.6 nm) and the HT matrix (0.9 nm). A representative line profile (Figure 3.7B) selected near the top of the pattern indicates a height of approximately 1.5 ± 0.2 nm above the HT matrix, which closely matches the expected thickness for a double layer.

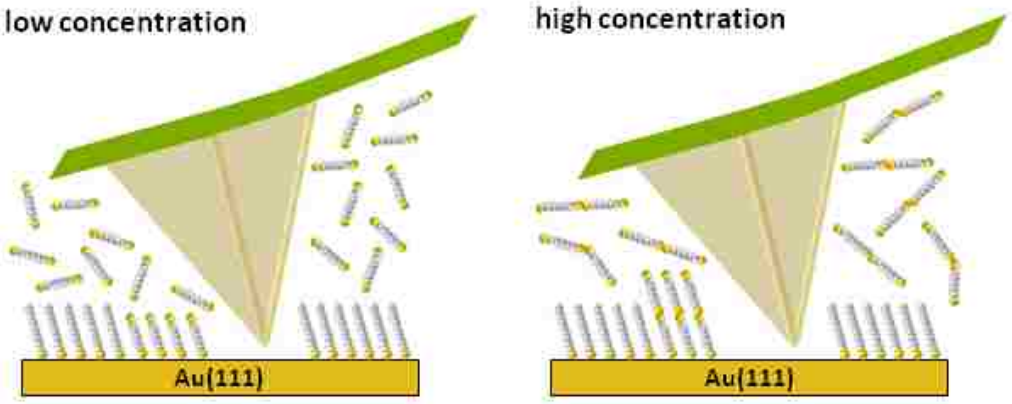

Figure 3.8. Differences in the surface assembly of α,ω-alkanedithiols when nanografting at low versus high concentration.

There are two possible mechanisms to consider for producing double layer nanopatterns by nanografting. Either the dithiol molecules form dimers in solution and then assemble directly on the surface as a bilayer, or the second layer could form successively in separate steps, with the second layer assembling as individual unpaired molecules attach in a sequential adsorption step. To gain insight about the assembly mechanism, monolayer patterns of 1,9-nonanedithiol were first written at **l**ow concentration ($\leq 10^{-6}$ M) and then continuously monitored to determine if double layers form over time. After checking patterns at regular intervals with successive AFM imaging for 3 h, additional changes in pattern heights were not detected. Next the patterns were exposed to solutions at higher concentration (10^{-5} M) and monitored *in-situ*. After 6 h incubation, the heights of monolayer patterns still were not observed to increase. If assembly occurred through successive adsorption of a second layer, then one would expect a bilayer to

eventually form on the exposed thiol groups of the monolayer patterns. Since bilayers were not observed to form over extended time, even with increased concentration of the liquid media the layer-by-layer assembly is not observed. A plausible mechanism for producing double layers at high concentration is that dimerization of α,ω-functionalized *n*-alkanethiols occurs in solution at high concentration due to effects of closer proximity. The proposed assembly model for writing monothiols or dimers directly onto the surface is shown schematically in Figure 3.8 when nanografting at different concentrations.

3.3.5 Nanografting with Hydroxyl-Terminated *n*-Alkanethiols

For concentrations ranging from 10^{-3} to 10^{-7} M nanografting with hydroxyl head groups was shown to form monolayer patterns exclusively (Figure 3.9). A pair of cross patterns of 11-mercaptoundecanol (MUD) were nanografted within an ODT matrix at 10^{-7} M (Figure 3.9A). The darker color in comparison to the surrounding matrix evidences that MUD nanopatterns are shorter than the ODT monolayer. The patterns measure 300 nm in dimension from top to bottom and side to side, and are spaced 300 nm apart. In both the topography and lateral force images (Figures 3.9A, 3.9B), the central rectangular area of the crosses is observed to be darker in comparison to the upper and lower inscribed areas. This is caused by changes in the writing density; the central areas were programmed to be rastered with more linesweeps than the upper and lower areas (Figure 3.9D). Thus, two different gradients of density were produced by a simple modification of the writing parameters. The cursor plot (Figure 3.9C) indicates that the nanopatterns are 0.6 ± 0.2 nm shorter than the ODT matrix, matching the expected height difference between ODT (2.1 nm) and MUD (1.5 nm).

When the concentration was further increased to 10^{-3} M for MUD, monolayer patterns were still produced by nanografting. The letters L, S, and U were nanografted into ODT at 10^{-3} M (Figure 3.9E), generating patterns that are shorter than the ODT matrix. Each letter is 200 nm

in size, with the lines of each letter are 50 nm in width. The thickness difference for MUD and ODT measured 0.6 ± 0.3 nm as shown with a representative cursor profile (Figure 3.9F). A model of the molecular heights is presented in Figure 3.9G.

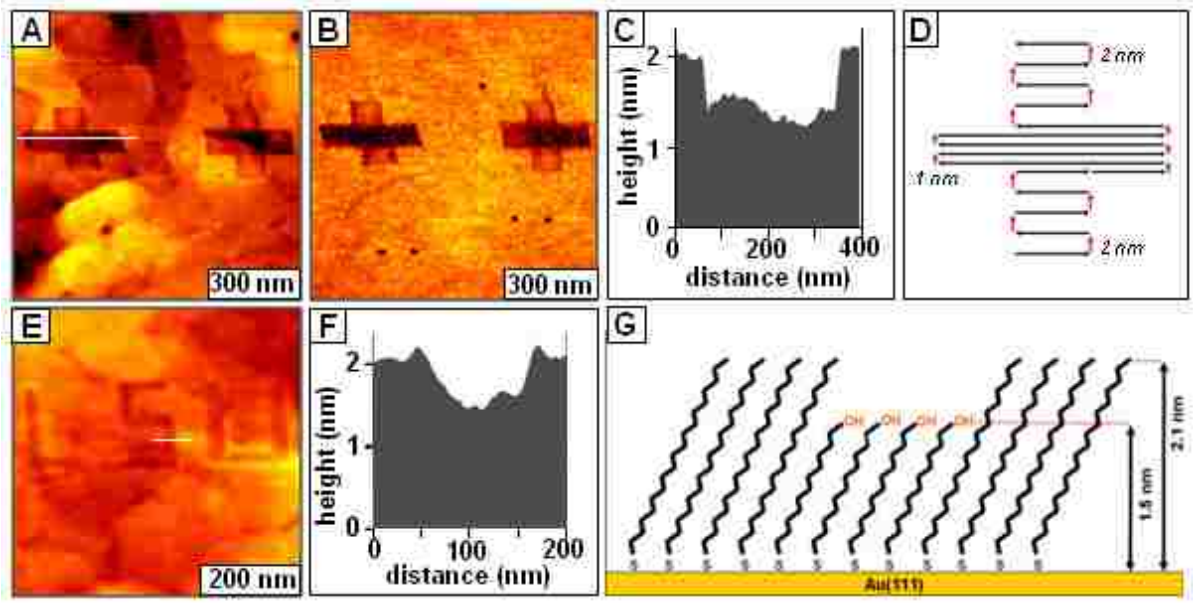

Figure 3.9. When nanografting hydroxyl-terminated SAMs, monolayers were produced regardless of concentration. [A] Topography image of cross-shaped patterns of MUD written into ODT at 10^{-7} M; [B] lateral force image; [C] profile for the white line in ***A***. [D] Raster design for writing the cross patterns. [E] Topograph of nanografted letters of MUD written in ODT at 10^{-3} M. [F] cursor plot for the white line in ***E***. [G] Model of molecular heights.

Unlike dithiol and carboxyl–terminated alkanethiols, nanografting with hydroxyl-terminated alkanethiols consistently produced monolayer patterns regardless of concentration. This suggests that attractive interactions between hydroxyl head groups are not strong enough to form multiple layers. We have found that hydroxyl-terminated groups provide good resist layers for subsequent binding of electrolessly deposited metals, since hydroxyl-passivated surfaces tend to inhibit non-specific binding.[240]

3.3.6 Sequential Nanografting of Monolayer Patterns with Different *n*-Alkanethiol Inks

As demonstrated in previous reports, multiple SAM patterns can be nanografted with different head groups and chain lengths when using an AFM scanner with high mechanical

stability.[221, 241] For example, three monolayer patterns with different molecular backbones and terminal chemistries were written sequentially in Figure 3.10 using a fabrication force of 8 ± 1 nN.

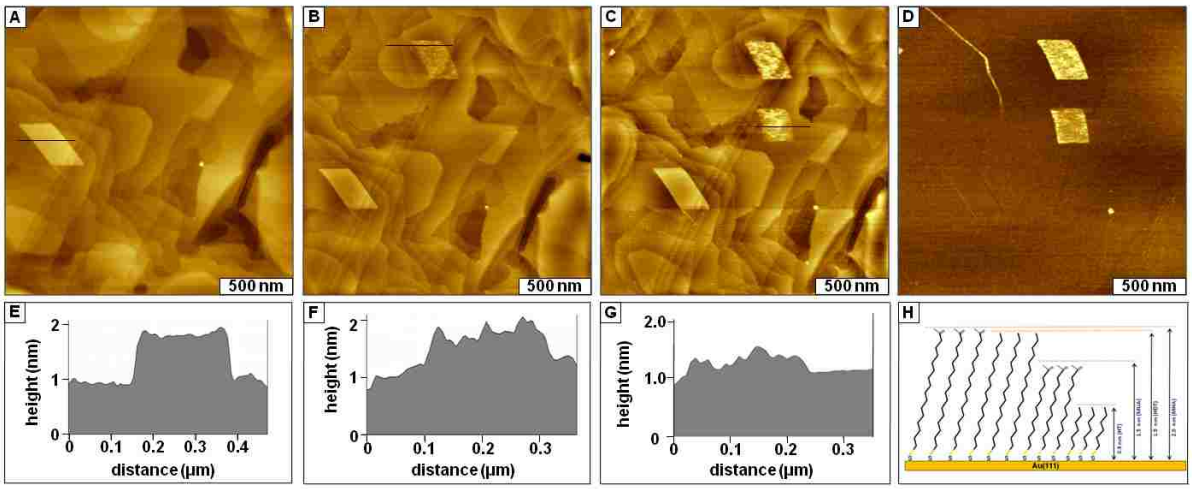

Figure 3.10. Sequential monolayer patterns of different *n*-alkanethiols nanografted within a hexanethiol matrix. [A] First a parallelogram of HDT was written at the left. [B] Next, a carboxylate-terminated nanopattern of MHA was written at the top of the image frame. [C] Finally, a shorter chain MUA nanopattern was nanografted on the right. [D] Corresponding lateral force image for ***C***. [E] Line profile for the nanopattern in ***A***. [F] Height profile for the second nanopattern in ***B***. [G] Line profile for the third nanopattern in ***C***. [H] Height model for the nanopatterns.

Each nanopattern was inscribed within a HT matrix after rinsing the sample cell with clean solvent and replacing the imaging media with different ink molecules; from left to right the patterns are composed of HDT, MHA and MUA for Figures 3.10A, 3.10B and 3.10C, respectively. To generate monolayer patterns, ink solutions were prepared in 2-butanol at a concentration of approximately 10^{-7} M. The concentration threshold for producing double layer patterns in 2-butanol is different than in ethanol by a factor of 10, which is most likely due to intrinsic differences in solvent properties. The lateral force image of Figure 3.10D shows that the second and third patterns with carboxylic acid head groups exhibit a different contrast in comparison to the HT matrix and the pattern of HDT, which are terminated with methyl groups.

The thickness of the nanografted patterns matches well with the expected dimensions of densely-packed monolayers. The representative line profiles in Figures 3.10E, 3.10F and 3.10G indicate heights of 0.9 ± 0.2 nm, 0.8 ± 0.3 nm and 0.4 ± 0.3 nm above the HT matrix for patterns of HDT, MHA and MUA, respectively which is in good agreement with the heights expected for monolayer patterns. The height model of Figure 3.10H depicts the expected differences in chain length for the nanopatterns with respect to the HT matrix monolayer, and the expected thickness differences would measure 1.0, 1.1 and 0.6 nm, respectively for HDT, MHA and MUA.

3.3.7 Bilayer Nanopatterns of MHA Are Produced with NPRW

Intermolecular interactions have important consequences for other nanoscale lithographies which are accomplished in air without solvent dilution. When patterning SAMs in air, the close proximity of molecules in neat parent solutions can generate double layer structures for certain types of α,ω-functionalized thiol SAMs, depending on the nature of the head groups. For example, in a previous report, bilayer nanopatterns were written for rigid rod molecules of biphenyl 4,4'-dithiol with heights corresponding to a bilayer, using the AFM-based approach of DPN which is accomplished in air using a coated AFM tip.[156] We further investigated the vertical assembly of carboxylate-terminated MHA using NPRW in ambient air.

The tip was pre-coated with ink molecules of a neat solution of MHA for writing, however instead of writing on bare gold surfaces the substrate was a methyl-terminated SAM of DDT. When the coated AFM tip is operated under force, the tip displaces the matrix molecules and new thiols from the tip adsorb onto the freshly exposed gold substrate following the shaving track of the tip (Figure 3.11A). The inscribed nanopatterns can then be characterized using the same coated AFM probe under a reduced load since the molecules of the coating are not delivered to the surface unless high force is applied. Two nanopatterns of MHA written in DDT using NPRW are shown in Figure 3.11B, which measure 220 x 280 nm^2 and 270 x 330 nm^2,

respectively. Both patterns were nanofabricated in air using an MHA-coated AFM tip by applying a force of 7 nN. The representative cursor profile in Figure 3.11C indicates the patterns are 2.4 ± 0.3 nm taller than the DDT matrix, which matches the expected dimensions for a densely packed bilayer. A double layer of MHA would measure 4 nm in height if densely-packed; therefore the expected thickness difference would be 2.5 nm compared to a DDT matrix.

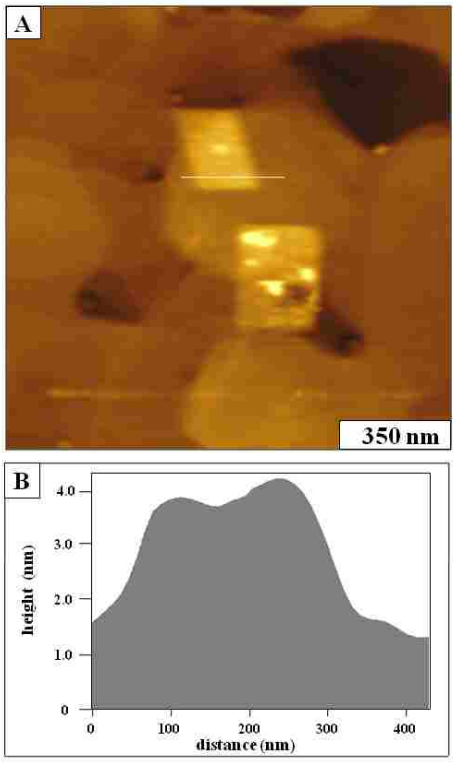

Figure 3.11. Bilayer nanopatterns of MHA were produced by NPRW. [A] Contact-mode AFM topograph of two patterns of MHA written within a matrix of dodecanethiol in air; [B] Corresponding cursor profile for the white line in ***A*.**

3.3.8 Mechanism for Nanopatterning Is Influenced by the Nature of Molecules, Concentration and Solvent Media

Intermolecular interactions in solution predominate when nanografting *n*-alkanedithiols or carboxylic acid terminated alkanethiols on surfaces directly into an upright configuration. At very low concentrations, bilayers did not form when nanografting patterns of alkanedithiols or carboxylic acid terminated alkanethiols. As the concentration was increased to a certain

threshold, the steric effects produce dimers, which can then be reproducibly written as double layers when nanografting. Head-to-head interactions between functional groups of SAMs have previously been observed with STM for lying-down phases of alkanethiols on graphite substrates.[242] The assembly mechanism with nanografting is different than that of solution self-assembly due to spatial confinement.[212, 222] When nanografting, *n*-alkanethiol molecules do not follow a transition from a lying-down to a standing-up phase, rather the molecules assemble directly into an upright or standing orientation. The area exposed by a scanning AFM tip is quite small, and this confined space prevents the assembly of a lying-down phase with the backbone of the molecule oriented parallel with the surface. It appears that double layers form when dimers from solution assemble immediately as a bilayer, connected together by head-to-head interactions between adjacent molecules. Carboxylic acids form head-to-head coupling through hydrogen bonding of head groups. Dithiol molecules, with a typical pK_a of 9-11 are more nucleophilic than alcohols with a corresponding pK_a of 15-19 and therefore dithiols will readily dimerize through oxidative coupling at high concentration.

3.4 Conclusion

Under certain conditions, the intermolecular interactions between molecules in solution, such as head-to-head dimerization can direct the vertical self-assembly of certain α,ω-alkanedithiols to produce bilayers when writing nanopatterns via nanografting or NPRW. For systems tested with methyl, hydroxyl, thiol or carboxylic acid head groups, monolayer patterns of ω-functionalized *n*-alkanethiols can be reproducibly generated when using dilute ethanolic or aqueous solutions. However, as the solution concentration is increased to a certain threshold, nanopatterns are formed with heights corresponding to a double layer when nanografting with carboxylic acid head groups or with α,ω-alkanedithiols. Patterns of nanografted SAMs with

methyl or hydroxyl head groups were observed to exclusively form monolayer structures for a relatively wide range of tested concentrations.

CHAPTER 4. INVESTIGATION AND APPLICATION OF NANOPARTICLE DISPERSIONS OF PIGMENT YELLOW 185 USING ORGANIC SOLVENTS

4.1 Introduction

Pigment nanoparticles or nanopigments are emerging as practical nanomaterials with properties that are intermediate between molecular and bulk materials.[243-246] Increasingly, dispersions of organic and inorganic nanopigments are being applied as inks used in digital printing, colorants for paints or coatings, cosmetics, and color filter arrays for the display industry.[247-257] The advantages of pigment nanoparticles are based upon properties that provide higher optical densities, an increased range of color scales, and sharper spectral features compared to pigments composed of micro particles.[245, 247, 253, 258-260] Additionally, higher transmittance can be achieved for display applications.[247, 260, 261]

For several of the applications, pigment nanoparticles are initially formulated into dispersions. Aqueous systems are predominantly used for dispersions that incorporate organic pigments including applications such as inkjet printing.[243, 249, 259, 262, 263] Eco-friendly solvent-based systems are also beginning to emerge and are more suitable for certain applications.[264] However, dispersing organic pigment nanoparticles that are 50 nm and smaller in organic solvents presents a challenge. Strong interactions between organic pigments and organic solvents (e.g., hydrogen bonding) can be difficult to overcome, resulting in significant nanoparticle aggregation that compromises optical properties.[261] This problem is magnified for dispersions with pigment concentrations in the 10 – 15 % range resulting in high viscosity dispersions. To prevent aggregation of pigment nanoparticles and also reduce viscosity, polymeric dispersants and agents that modify the surface of nanoparticles can be used.[259, 263, 265] Polymer-grafted organic pigments have also been reported to produce stable organic solvent-based dispersions.[266]

However, there are few studies reported that show how dispersants and synergists can be used to disperse organic pigment nanoparticles smaller than 50 nm for non-aqueous systems.

Dispersions composed of organic pigment nanoparticles in organic solvent have been produced by methods such as mechanical milling[267] and supercritical antisolvent processes (SAS).[253, 261] Mechanical milling is the most common method used to produce pigment nanoparticles in organic media. This process often involves use of ceramic milling media for particle size reduction.[267] Organic pigment dispersions prepared by using supercritical antisolvent processes in combination with various organic aprotic or protic co-solvents have been reported.[253, 261] Typically, a fluid is termed supercritical when the pressure and temperature are in a state above the fluid critical temperature and pressure, thereby permitting the gaseous and liquid phases to coexist.[261, 268] A new dry milling process used for organic pigments in the presence of silica nanoparticles produced uniform hybrid core-shell nanostructures.[269, 270] However, attempts to disperse the dry milled nanoparticles in PGMEA resulted in slight aggregation, as determined by DSL measurements combined with transmission electron microscopy (TEM) images.[269]

For pure organic pigments, the resulting particle size achieved using traditional mechanical milling depends upon several variables including the type and size of the milling media, milling speed, dispersant, and solvent type. The typical size range for particles and/or aggregates produced by traditional mechanical milling is 200 nm to 1 μm. The supercritical fluid (CO_2) process produced nanoparticles that ranged from 15 μm to 100 nm.[253, 261] This broad range of organic pigment nanoparticles can be attributed to a host of factors including solvent effects, flow rate, temperature, and pressure. The dry milling of organic pigments with silica nanoparticles produced core-shell nanostructures with an average size comparable to the parent silica nanoparticles (~20 nm) as determined by TEM.

To broaden the potential capabilities and applications for non-aqueous dispersions, more fundamental studies in this area are required. Therefore, our work has focused upon generating a uniform distribution of nanoparticles smaller than 50 nm and dispersing the nanoparticles in an eco-friendly solvent system. Comprehensive studies that cover the desired particle size distribution for organic pigments dispersed in organic solvents have been difficult to identify. Our studies probe the influences of common polymeric dispersants, surface-modifying agents, and changes in solvent polarity on aggregation and dispersion stability. Results demonstrate low viscosity stable dispersions composed of uniform organic pigment nanoparticles smaller than 50 nm and dispersed in an organic solvent. A correlation between nanoparticle aggregation and the resulting spectral properties of thin films fabricated from the solvent-based dispersions was established. Studies and improvements in this area ultimately can contribute to advancements in the optical performance of thin films made from pigment nanoparticles for commercial applications.[271-273]

4.2 Experimental

4.2.1 Materials and Reagents

Commercially available dispersants were used without further purification: Solsperse 22000 from Lubrizol Additives (Wickliffe, Ohio); pigment yellow 185 (PY-185) from BASF Corporation (Florham Park, NJ); and Disperbyk-161 from BYK USA Inc. (Wallingford, CT). Propylene glycol monomethyl ether acetate (PGMEA) and cyclohexanone were obtained from Sigma Aldrich (Milwaukee, WI). The proprietary milling media was procured from Eastman Kodak Company.

4.2.2 Preparation of Dispersions of Pigment Yellow 185

In a typical process, 200 g of dispersion was prepared by combining PGMEA with the dispersant polymer Disperbyk 161 in a 1.0 L stainless steel cold water-jacketed vessel. Then, a

70 mm diameter high-shear Cowles disperser blade connected to a Ross mechanical stirrer (Model HSM-100H2) was submerged in the mixture and operated at 500 rpm. While in operation, PY-185 was introduced, followed by the proprietary milling media. The final mixture was composed of 80% PGMEA, 2% butlyacatate,12% PY-185, and 6% of the active polymer. After adjusting the stirrer to 1000 rpm, the dispersion was milled for 1 h at a mixing rate of 1000 rpm. The dispersion was isolated after vacuum filtering through 5 μm filter media.

4.2.3 Dynamic Light Scattering (DLS)

Particle size distributions of pigment nanoparticles dispersed in fluids were measured using a Nanotrac model 150, previously known as Ultrafine Particle Analyzer (UPA) from Microtrac (Saint-Petersburg, Russia). Nanoparticles, because of their small size (usually <1 μm), undergo random Brownian diffusion. The DLS instrument was operated in the frequency domain and used a frequency spectrum analyzer to measure the particle diffusion over time. Once the distribution of diffusion coefficients of the particle ensemble was measured, the Stokes-Einstein equation was used to calculate a particle size distribution making an assumption of spherical particle geometry (eq 1). The DLS plots presented are averages of multiple scans of each sample. Stokes-Einstein equation:

$$D = kT/(3 \pi \eta d) \quad (1)$$

where η is the solvent viscosity, d is the diameter of the nanoparticles, T is absolute temperature, k is the Boltzmann constant, and D is the diffusion coefficient.[274]

4.2.4 Sample Preparation by Spin-Coating

Dispersions were spin-coated on clean glass slides within 48 h of preparation. The substrates used were borosilicate glass 1.1 mm thickness (2.5 × 2.5 μm^2). Glass cleaning was an automated process performed in a class-100 clean room. Slides were cleaned by rinsing with deionized water and then washed for 30 s in a solution of deionized water with Valtron SP 2500

alkaline detergent solution (Valtech Corp., Pottstown, PA). The glass surfaces were rinsed with deionized water and the cycle was repeated once. After rinsing, the slides were dried under nitrogen for 25 s and exposed to an infrared lamp for 25 s. The glass was then spun at 2500 rpm, followed by a spin dry cycle at 2500 rpm for 25 s. The glass plates were transferred to a vacuum-operated spin-coater before placing ~1 mL of the dispersion onto the plate. The sample was spun for 3 s at 100–500 rpm before the speed was ramped to 2500 rpm for 30 s. The coated plate was then air-dried and cured on a hot plate by heating for up to 40 min at 55 C. The samples were stored for up to 2 months for AFM characterization and optical measurements.

4.2.5 Total Transmittance Measurements

Spectrophotometry measurements of dispersions coated glass plates were made using a CARY 5E UV-Vis-NIR Spectrometer from Varian (Palo Alto, CA) with an integrating sphere attachment, operating in total transmittance mode. The total transmittance mode measures both the diffuse and specular components of the sample. Blank substrates of uncoated glass slides were used for a baseline measurement. The blank slides were subjected to the same cleaning procedure as the coated surfaces.

4.2.6 Atomic Force Microscopy (AFM)

Atomic force microscopy images of dispersions coated glass plates were acquired using a Dimension 3100 scanning probe microscope with maximum scan area of $90 \times 90\ \mu m^2$ (Veeco Metrology Inc., Santa Barbara, CA). Nanoscope v5.12 software was used for data acquisition. Digital images were processed with Gwyddion (version 2.9), which is open source software supported by the Czech Metrology Institute freely available on the Internet (http://gwyddion.net). Commercially available silicon nitride cantilevers with resonance frequencies ranging from 200 to 400 kHz, and spring constants ranging from 20 to 80 N/m were used for imaging in tapping mode (Veeco Probes, Santa Barbara, CA).

4.3 Results and Discussion

Before investigating the capability of blocking aggregation of nanoparticles smaller than 50 nm, a process was needed to generate a uniform distribution of nanoparticles in the desired particle size range. To accomplish this goal, pigment yellow 185 (PY-185) was combined with various dispersing polymers in PGMEA and then mechanically milled using the proprietary milling media developed at Eastman Kodak Company. It was determined from the dispersant screening process that Disperbyk – 161 worked most effectively for generating and dispersing PY-185 nanoparticles while maintaining a low viscosity (10 – 20 cps). The polymeric dispersant contains amine functional groups that can favorably interact (through hydrogen bonding) with surface-exposed amine groups of PY-185. The molecular structure of PY-185 is shown in Figure 4.1.

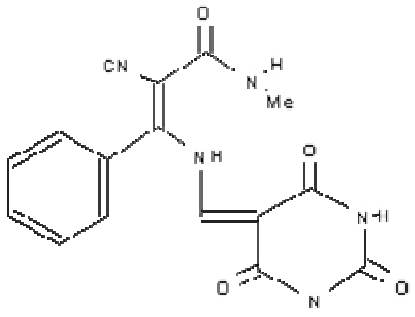

Figure 4.1. Molecular structure of PY-185.

4.3.1 Characterizations of Nanoparticle Samples Prepared in PGMEA

Dynamic light scattering (DLS) measurements were used to assess the particle size distribution and stability of the resulting dispersions. Particle sizing data were collected within 24 h and after 90 days of preparation. Size distribution plots of the reference dispersion, composed of PY-185, PGMEA, and Disperbyk-161, are represented in Figure 4.2. Each plot showed a dominant population of nanoparticles in the 10–50 nm range. A second population

above 100 nm was also observed. However, for the plot acquired after 90 days, a shift toward larger particles was observed, indicating instability and particle aggregation.

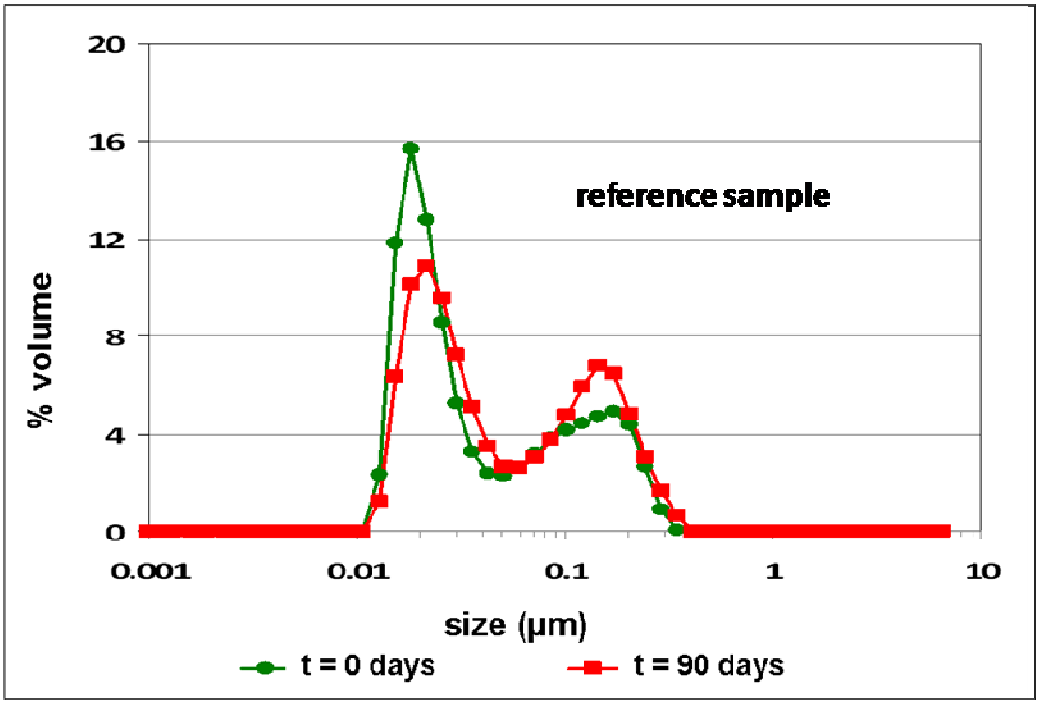

Figure 4.2. Size analysis (DLS) of reference pigment nanoparticles prepared in PGMEA. Analyses were carried out immediately after dispersion preparation and after aging for three months.

A synergist was used as a surface modifier to enhance interactions between pigment nanoparticles and the dispersing polymer. Moreover, to probe the influence of PY-185 surface modification, the yellow synergist Solsperse 22000 was introduced under the same dispersion preparation conditions as the reference dispersion. Size distributions acquired with DLS of the resulting dispersions are represented in Figure 4.3. The plots show a more uniform size distribution compared to the reference control sample in Figure 4.2 with a mean nanoparticle size of 12 nm. There was no significant detection (2.2 %) of particles larger than 100 nm. In addition, no detectable shift in the size distribution was observed after 90 days, indicating stability for the dispersion formulation.

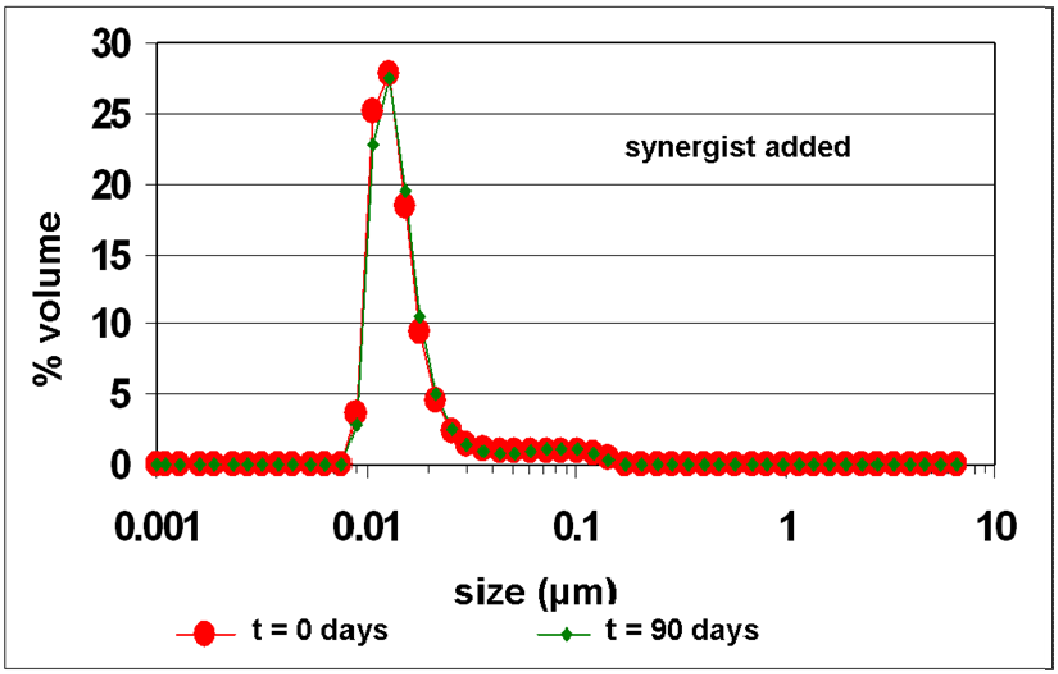

Figure 4.3. Size distribution of pigment nanoparticles in PGME with synergist obtained by DLS. Analyses were carried out immediately after preparing dispersions and after three months.

To elucidate if the improved yellow dispersion formulation translated into improved optical properties of thin films, the preceding dispersions were coated on glass plates and characterized by atomic force microscopy and total transmittance spectrophotometry. Measurements with AFM were critical in determining if the reference dispersion was composed of two particle size distributions or a distribution of dispersed and aggregated nanoparticles. In addition, AFM analysis was useful in evaluating if the improved nanoparticle uniformity of synergist-containing dispersions translated into uniform coatings and with possible optical advantages.

Collected AFM images of the reference dispersion confirmed that uniform nanoparticles were formed with significant aggregation detected. In the topography image shown in Figure 4.4A, approximately eight bright zones of dense nanoparticle aggregates are apparent within the 20 × 20 μm^2 scan, covering 8% of the total surface. The lateral dimensions of these taller

domains ranged from 500 to 2000 nm, and the average height measured 200 nm. A zoom-in view of the central region without the dense clusters is displayed in Figure 4.4A'. The image exhibits a tightly packed arrangement of pigment nanoparticles on the surface; the overall dimensions of the dense areas ranges from 100 nm to 270 nm. The RMS roughness measured 9.1 nm for the area displayed in Figure 4.4A'. The simultaneously acquired phase image in Figure 4.4A" reveals a uniform color for the nanoparticles. The homogeneous color suggests a highly consistent surface composition without evidence of contamination or additives. The corresponding cursor profile of Figure 4.4A'" measured the size of pigment nanoparticles to be 50 nm, whereas the cluster had a height of approximately 150 nm.

Similar to the coating prepared from the reference dispersion, the synergist-containing coating was also characterized using tapping mode AFM. The images are shown in the bottom panels of Figure 4.4. A few small areas of dense nanoparticle clusters are still present in the wide area topography view of Figure 4.4B; however, the areas are considerably smaller in dimension. The overall regions of dense aggregates cover approximately 1.5% of the surface, and lateral dimensions of the dense areas range from 60 to 80 nm. The heights of the bright zones measure 120 ± 26 nm, referencing the shallowest area of the surface as a baseline. A close-up view (Figure 4.4B') more clearly displays the morphology of pigment aggregates, which range from 50 to 150 nm in size. The RMS roughness for the 2.5 × 2.5 μm^2 frame measures 7.9 nm. The corresponding phase image in Figure 4.4B" exhibits interesting surface changes that are not apparent in the topography frames. Two distinct colors are evident; the dark areas identify the synergist material added to the dispersion. The sample contains a well-dispersed molecular adsorbate mixed with the pigment nanoparticles, in contrast to the reference sample image shown in Figure 4.4A". Phase images provide a highly sensitive map for distinguishing differences in the chemical composition of surfaces. The phase data clearly displays the intercalation of the

synergist located at edges surrounding nanoparticles throughout the sample. The line profile presented in Figure 4.4B''' shows a pigment nanoparticle cluster with a height of approximately 120 nm.

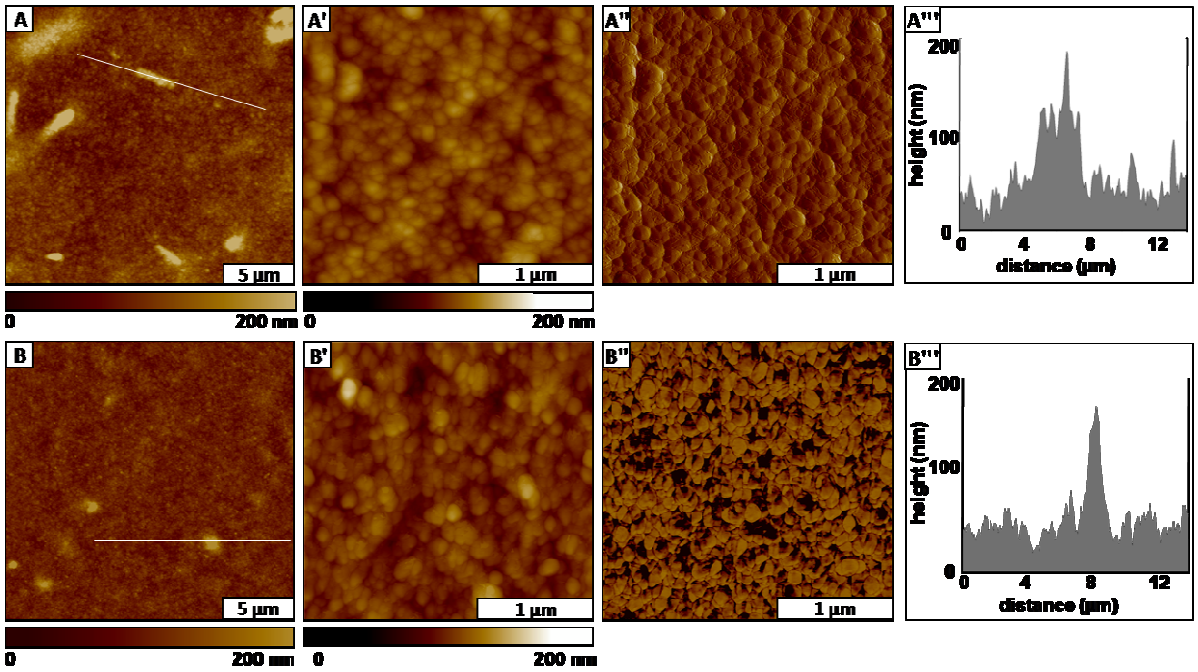

Figure 4.4. Surface views of coated pigment nanoparticles prepared with polymeric dispersant only. [A] Tapping mode AFM topography image (20 x 20 μm^2); [A'] zoom-in topograph (2.5 x 2.5 μm^2); [A''] phase image for **A'**; [A'''] cursor profile of **A.** Images of coated pigment nanoparticles prepared with polymeric dispersant in the presence of a synergist: [B] Wide area topograph (20 x 20 μm^2); [B'] zoom-in view of **B** (2.5 x 2.5 μm^2); [B''] phase image for **B'**; [B'''] profile for the line in **B**.

The amount of nanoparticle clusters or aggregates detected in the AFM images is not entirely consistent with the DLS data because the AFM views display selected local areas of coated surfaces, which may not be representative of dispersions of pigment nanoparticles. Spin coating can induce aggregation as a result of solvent evaporation during the spinning process. However, the influence of the synergist is indicated by smaller aggregates in coatings prepared from synergist-containing dispersions relative to coatings prepared from the reference dispersion. This is supported by the cursor profile of the synergist coating represented in Figure 4.4B'''

showing fewer and shorter clusters compared to the reference coating. In addition, the surface coverage for areas of high density for the synergist coating was reduced from 8.4 to 1.5%. The indicated size of the nanoparticles was consistent between the coatings, however, rms roughness of the surface was shown to decrease slightly from 9.1 to 7.0 nm for coatings containing the synergist. The values of rms roughness were calculated for local areas of the surface, and are not necessarily an indicator of surface changes for the entire sample. The values of rms roughness change considerably from frame to frame, even for the same sample. It should be noted the convolution of tip geometry could affect roughness measurements, as well as the size of the area selected for measurements. Therefore, the rms roughness provides a relative indicator of local changes only for selected areas of the same dimensions, which are representative of areas viewed throughout the surface. The rms roughness can be helpful for local comparisons with AFM, but is not a definitive estimate of macroscopic roughness.

Research on pigment nanoparticles has shown the least aggregated or more dispersed pigment nanoparticles normally leads to sharper spectral features and hence transmits more light.[247, 261] To confirm that reduction in nanoparticle aggregates of the coated dispersions translates into improved optical properties, each coating was characterized by total transmittance spectrophotometry. A comparison of the total transmittance spectra in the visible wavelength region for the coated dispersions is presented in Figure 4.5. Figure 4.5B displays a zoom-in on the 490–525 nm wavelength region to show that the least aggregated coating prepared from the synergist-containing yellow dispersion has the sharpest-cutting total spectral transmittance features. As expected, the coating from the aggregated yellow dispersion made without the synergist has the least sharp spectral cut and transmits the least amount of light, especially in the 490–525 nm wavelength region.

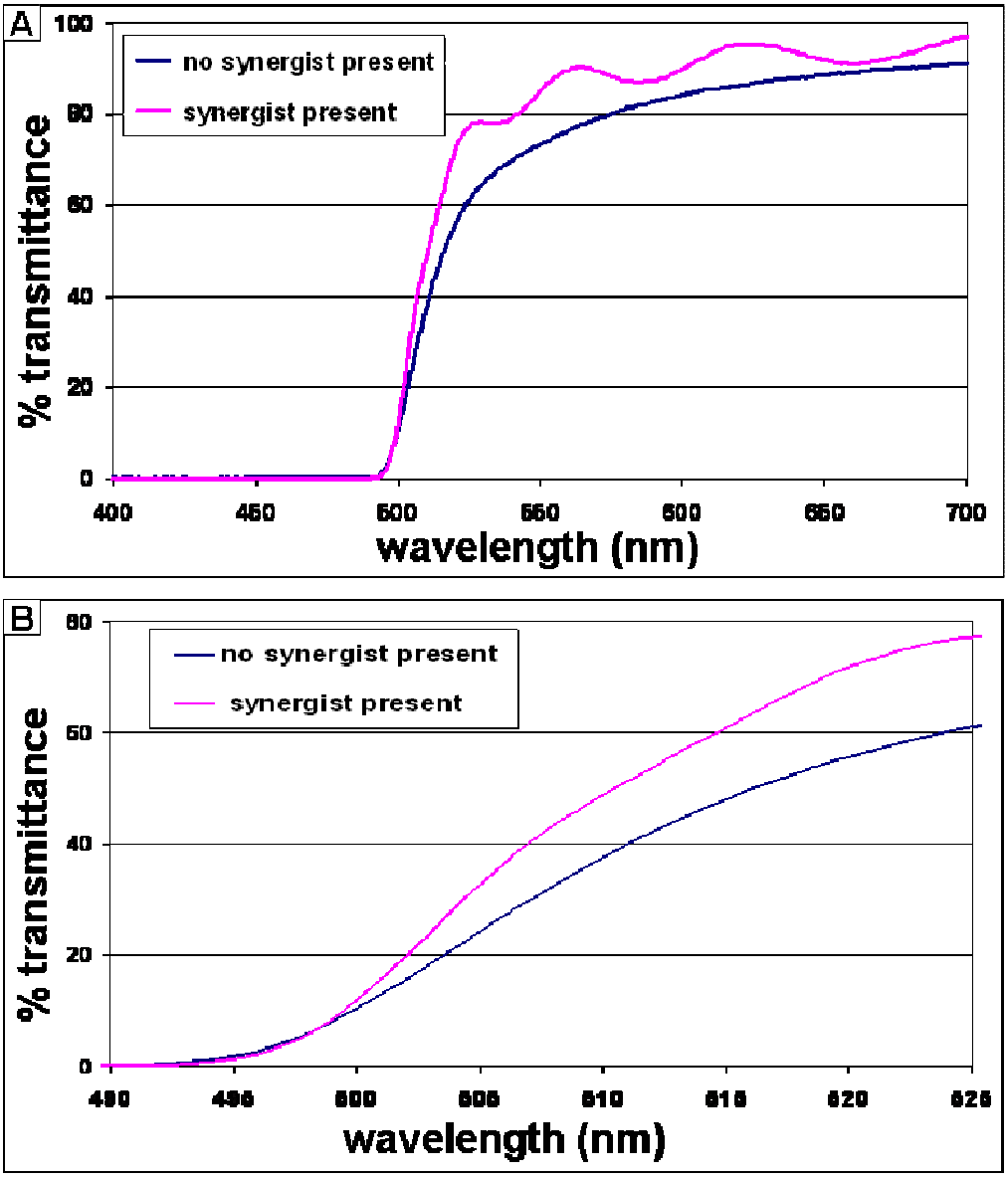

Figure 4.5. Transmittance spectra of coated dispersions with and without synergist present: [A] Visible wavelength region; [B] Zoom-in view of 490–525 nm.

4.3.2 Characterizations of Nanoparticle Samples in Mixed Solvents

To determine the influence of solvent polarity on dispersion properties, synergist-containing dispersions of PY-185 were prepared using solvent mixtures. The standard solvent PGMEA was combined in different ratios with the lower polarity solvent cyclohexanone. Chemical structures of both solvents are illustrated in Figure 4.6.

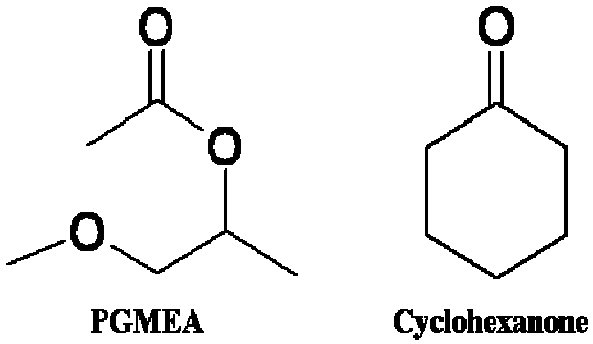

Figure 4.6. Chemical structure of PGMEA and cyclohexanone solvents.

4.3.2 Characterizations of Nanoparticle Samples in Mixed Solvents

Dispersions were prepared using 3:1 and 1: 1 ratios of PGMEA and cyclohexanone, respectively. Size analyses of resulting dispersions were obtained from DLS measurements for the mixed solvent dispersions (Figure 4.7). For the dispersion prepared using a solvent ratio of 3:1, analysis immediately after preparation showed 37% of the nanoparticles ranged from 10 to 43 nm in size and 63% ranged from 43 to 350 nm. After aging, measurements showed a slight shift toward larger sizes. However, overall 36% of the nanoparticles still were within the 10 to 43 nm range. The shape of the second peak became sharper, showing a particle size range of 43 nm to 970 nm. (Figure 4.7B). Results were similar for the dispersion prepared with a 1:1 mixture of PGMEA to cyclohexanone (Figure 4.7A). Three peaks were apparent, showing 3% of the nanoparticles are less than 20 nm in size, 56% ranged from 20 to 125 nm, and 41% covered the size range of 125 to 350 nm. After 90 days, the particle size distribution changed more significantly, showing a greater percentage of larger particles. The DLS distribution showed 43% in the 10 to 125 nm range and 57% ranged from 125 nm to as large as 820 nm. Thus, with a higher percentage of cyclohexanone, the rate of aggregation increased based on the detection of larger particle sizes.

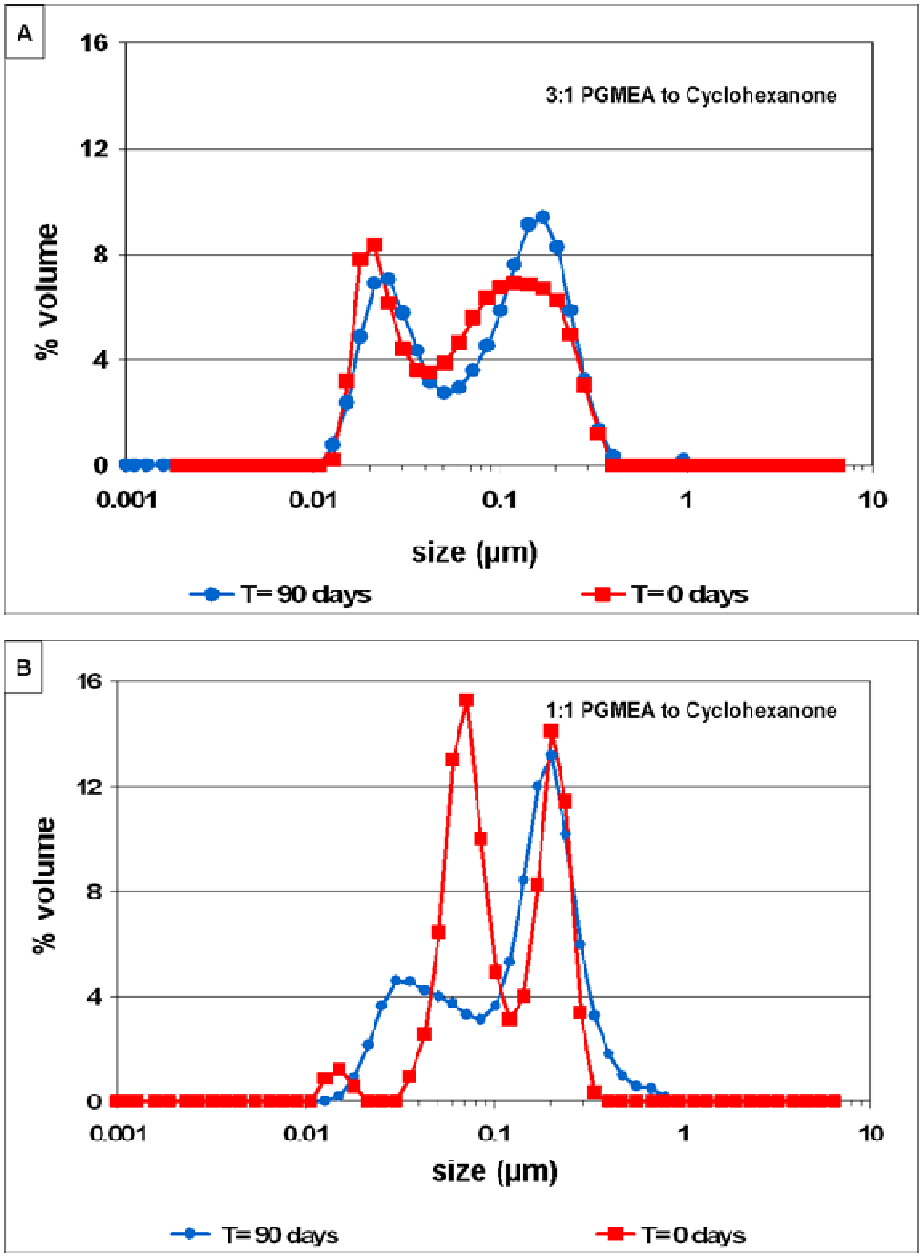

Figure 4.7. Size distribution of pigment nanoparticles prepared with a synergist dispersed in mixtures of PGMEA and cyclohexanone. [A] Data acquired directly after dispersion were prepared with a 3:1 PGMEA/cyclohexanone ratio and after aging for 90 days. [B] Data acquired directly after dispersion was prepared with a 1:1 PGMEA/cyclohexanone ratio and after aging for 90 days.

Samples of the mixed solvent dispersions were also spin coated on glass and imaged with tapping-mode AFM to determine the nanoscale morphology. The coatings from dispersions prepared with a 3:1 ratio of PGMEA to cyclohexanone are shown in the upper panels of Figure

4.8. The lower panels of Figure 4.8 show coatings prepared from the 1:1 solvent mixture. Multiple areas were examined throughout the sample, and the results of Figure 4.8 are representative of the morphologies of the entire surface. Comparing the upper versus lower topography frames for the different solvent mixtures, the samples are mostly indistinguishable. Even for the 2.5 × 2.5 μm^2 zoom-in view, the shapes and arrangements of pigment nanoparticles within the films are quite similar for Figure 4.8A' (3:1 ratio PGMEA:cyclohexanone) as compared to Figure 4.8B' (1:1 ratio PGMEA:cyclohexanone). As a quantitative estimate, the rms value for Figure 4.8A' measured 13 nm compared to 15 nm for Figure 4.8B', which further indicates that the surface morphologies are quite similar for the two samples. Do to extensive aggregation, nanoparticle clusters could not be observed from the mixed solvent coatings. There are two colors apparent within the phase images; there is a dark outline within the grooves and spaces between pigment nanoparticles in Figures 4.8A" and 4.8B", which corresponds to areas with intercalated synergist, as shown previously for the phase image of Figure 4.4B". An estimate of the surface area of the regions containing synergist measured 45 ± 5% and 43 ± 5% for Figures 4.8A" and 4.8B", respectively.

Based on DLS data, introducing the lower polarity solvent cyclohexanone promotes nanoparticle aggregation. A possible mechanism is that a less polar solvent increases the net charge of the dispersed pigment nanoparticles, leading to greater forces for self-aggregation. Cyclohexanone was shown to promote aggregation of nanoparticles and dispersion instability over time

Surface analysis by AFM also indicates the large clusters viewed in solution by DLS do not necessarily persist when the samples are spin-coated on surfaces; the forces of surface adhesion can often break the clusters into smaller assemblies when films are formed under centrifugal force. The sizes of nanoparticle aggregates within surface films are often quite

different than sizes of clusters dispersed in solutions; therefore, when comparing DLS results to AFM measurements, the results often show differences for size measurements.

Changing the polarity of the dispersion solvent was shown to be quite effective for preventing dense zones of pigment nanoparticles from forming within spin-coated films. Whether the solvent composition was composed of predominantly PGMEA or equal parts with the lower polarity cyclohexanone, the surface topologies were indistinguishable for samples prepared. Surface chemistry was unchanged as viewed with phase images, and the rms roughness was quite similar for samples prepared with the two different solvent ratios.

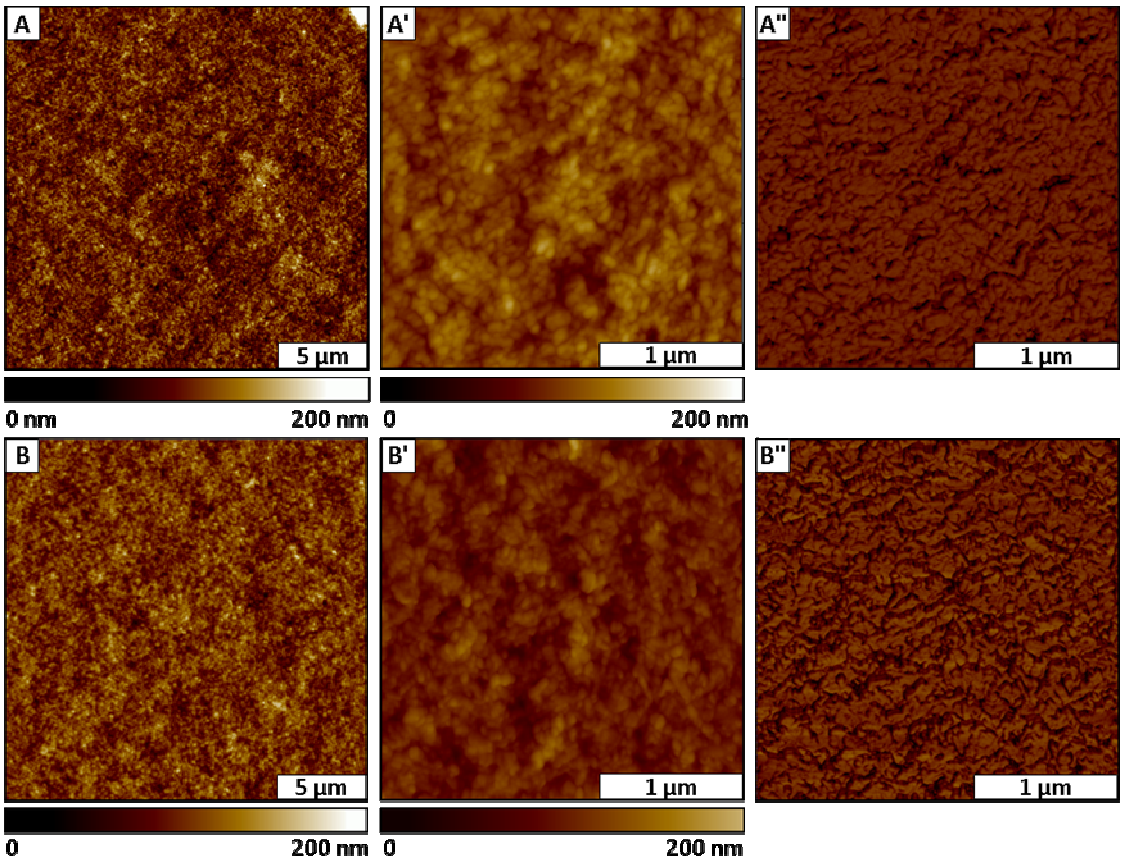

Figure 4.8. Surface views of pigment nanoparticles coated from 3:1 PGMEA/ cyclohexanone ratio. [A] Wide view AFM topograph (20 x 20 μm^2); [A'] zoom-in view (2.5 x 2.5 μm^2); [A"] corresponding phase channel for **A'.** Images of pigment nanoparticles coated from 1:1 PGMEA/ cyclohexanone ratio: [B] AFM topograph (20 x 20 μm^2); [B'] zoom-in view (2.5 x 2.5 μm^2); [B"] phase image for **B'**. Both dispersion mixtures contain synergist.

A comparison of the total transmittance spectral plots of coatings prepared from the mixed solvent dispersions is shown in Figure 4.9. Included in the comparison are the reference non-synergist and the PGMEA only with synergist coatings. Relative to the reference non-synergist coating, a trend of increased transmittance was observed for coatings that contained the synergist Coatings from mixed solvent dispersions with synergist have total spectral transmittance properties that fall in the middle of the reference (without synergist) and the pure PGMEA with synergist coatings.

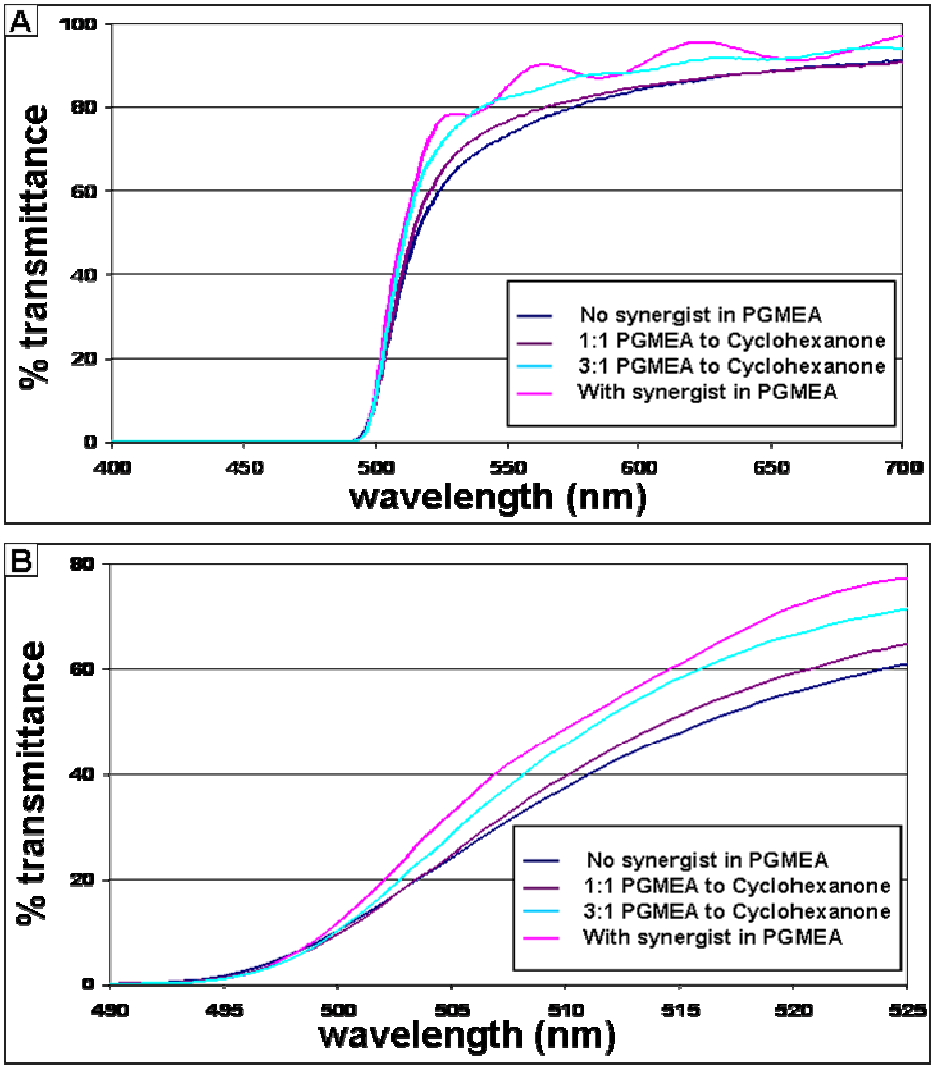

Figure 4.9. Transmittance spectra of coated dispersions showing influence of synergist and solvent systems.

Although AFM images did not distinguish a difference in the degree of nanoparticle aggregation for the mixed solvent coatings, the coating from the 3:1 solvent mixture was sharper cutting in its total spectral transmittance properties than the coating from the dispersion with the 1:1 solvent ratio. The results would be consistent with increased aggregation as the solvent shifts to lower polarity. These spectral studies show the impact of nanoparticle aggregation on the ability to obtain desirable sharp-cutting spectral characteristics and increased transmitted light for thin films prepared from pigment nanoparticles.

4.4 Conclusion

A systematic approach to the design and development of a stable dispersion composed of organic pigment nanoparticles in an organic solvent has been demonstrated. To our knowledge, the combination of dispersion properties produced from this work has not been disclosed from prior studies. Specifically, this study produced a low viscosity dispersion consisting of uniformly dispersed PY-185 nanoparticles in PGMEA with a mean nanoparticle size of 12 nm. These properties were observed for a pigment concentration measured at close to 10-weight %. Key parameters that influence the dispersion properties have been identified and can be used as a guide for future studies. This work demonstrated the correlation of improved optical properties for thin films prepared from dispersions free of significant nanoparticle aggregation. Well-dispersed dispersions of PY-185 yielded coatings with superior optical properties in terms of sharper cutting transmission bands with overall higher transmission. Surface characterizations by AFM were used to evaluate the uniformity of nanoparticle arrangements within spin-coated films prepared on glass. There are several possible factors influencing aggregation. The influence of modifying the dispersion of pigment nanoparticles by introducing a synergist can be considered an enabling technology for achieving desirable dispersion properties. Total transmittance measurements showed the sharpest spectral features and highest transmission from

coatings prepared using the most stable dispersion. Spectral measurements also showed a decrease in transmittance when a less polar solvent was used. However, dispersions without the synergist showed the lowest spectral transmittance. Finally, it can be stated that this work provides useful insight on how to advance the performance of optical thin films that incorporate pigment nanoparticles.

CHAPTER 5. RESPONSE OF IRON(III)-NICKEL NANOPARTICLES TO A MODULATED ELECTROMAGNETIC FIELD DETECTED BY ATOMIC FORCE MICROSCOPY

5.1 Introduction

Nanotechnology has made it possible to synthesize and specifically tailor the magnetic properties of nanoparticles for various applications.[275] Applications for magnetic nanoparticles include high-density data storage devices,[276, 277] ferrofluids,[278-280] and magnetic refrigeration systems.[281] Magnetic nanoparticles are also critical for biomedical applications such as magnetic resonance imaging,[282-284] hyperthermic treatment for malignant cells,[285, 286] magnetic separations,[283, 287] site specific drug delivery[34] and the manipulation of cell membranes.[288]

For scaling effects of nanomagnetic materials, precise knowledge of the relationships between particle shape and size, surface structure and the resulting magnetic properties is incomplete. Magnetic properties with nanoscale dimensions are not fully defined even for simple particles composed of pure materials such as Fe, Co, or Ni, whereas the bulk properties are well understood.[289] Essentially, the physics and properties of magnetic nanostructures cannot necessarily be inferred from scaled down properties of bulk materials.[290] Unique magnetic phenomena are exhibited for nanoparticles which are different than bulk properties. As particle sizes decrease, more of the atoms of a nanoparticle are surface atoms; therefore surface and interface effects predominate.[291] For magnetic materials, surface effects can lead to a decrease of the total magnetization in comparison to the bulk value, such as for oxide nanoparticles.[292] However, an enhancement of the magnetic moment was reported for metal nanoparticles of cobalt.[293]

Iron(III)-nickel nanoparticles have interesting nanoscale magnetic properties and have been shown to enhance recording speed when used as materials for magnetic recording

devices.[294-297] Metal nanoparticles are being applied in energy conversion and electronic devices.[294, 296] As the size of nanoparticles become smaller, the magnetic properties of nanoparticles have been shown to exhibit new phenomena such as giant magnetoresistance (GMR) and superparamagnetism.[294-298] Composite intermetallic nanoparticles of iron and nickel were synthesized either in a conventional oven or in a microwave oven equipped with high pressure vessels, based on a previous method.[296] Microwave systems offer a promising approach for better control of synthetic parameters for size control of during nanoparticle synthesis. Microwaves furnish precise control of temperature and pressure parameters within a sealed container by using a fiber optic thermocouple and a pressure transducer for feedback. Also, the reaction time and reagents can be scaled down for systematic investigations of optimal parameters. The benefits of using microwave ovens for sample preparation and synthesis are improved safety, speed, smaller reagent volumes and increased product yields in comparison to traditional methods which require lengthy heating in an oven.[299-307]

In this report, we demonstrate a new approach for sensitive and selective surface measurements of $FeNi_3$ magnetic nanoparticles using a hybrid imaging mode of atomic force microscopy (AFM). Previously, we demonstrated that the MSM instrument configuration can be used for selective magnetic imaging of electrolessly deposited iron-oxide capped nanostructures formed on organosilane nanopatterns[308] and for imaging nanostructures of ferritin.[309] Contact-mode AFM is accomplished simultaneously with magnetic sample modulation (MSM) to selectively image the motion of $FeNi_3$ nanoparticles. The flux of an oscillating AC electromagnetic field causes the nanoparticles to vibrate during AFM imaging, enabling detection of magnetic response at the level of individual nanoparticles. Changes in the phase and amplitude of the sinusoidal motion of the nanoparticles that are driven to vibrate by MSM can be used to selectively detect and map the positions of magnetic nanoparticles, while the sample is

imaged with a non-magnetic probe in continuous contact-mode. With MSM, responses of the amplitude and phase signal simultaneously with the topographic frame, as well spectra of the vibrational response can be acquired for selected magnetic areas of the surface.

5.2 Experimental Section

5.2.1 Materials and Reagents

Nickel(III) nitrate hexahydrate ($Ni(NO_3)_2 \bullet 6H_2O$, 98%), iron(III) nitrate nonahydrate ($Fe(NO_3)_3 \bullet 9H_2O$, (98%), hydrazine hydrate ($N_2H_4 \bullet H_2O$, 80%), and sodium dodecyl sulfate (SDS) were purchased from Alfa Aesar and used without further purification. Sodium hydroxide pellets were purchased from Mallinckrodt Baker Inc. (Phillipsburg, NJ). Ruby muscovite mica substrates were obtained from S&J Trading Company (NY, USA). Silicon wafers doped with boron were purchased from Virginia Semiconductor, Inc. (Fredericksburg, VA). The silicon surfaces were cleaned with piranha solution, which is a mixture of sulfuric acid and 30% hydrogen peroxide at a (v/v) ratio of 3:1. Piranha solution is highly corrosive and should be handled carefully. Substrates were then rinsed copiously with deionized water and dried in air.

5.2.2 Synthesis of $FeNi_3$ Nanoparticles

Intermetallic nanoparticles ranging from 1 to 15 nm in diameter were prepared by modifying a procedure previously reported by Liao.[13] First, a mixture of 0.1 g iron(III) nitrate nonahydrate and 0.22 g of nickel(III) nitrate hexahydrate were placed into a beaker. Next, 22 mL of deionized water (18 Ω) was added and the solution was mixed until the solid dissolved. The solution was made alkaline by increasing the pH to 11 using sodium hydroxide. A 2 mL volume of hydrazine hydrate (reducing agent) and 0.5 mL of sodium dodecyl sulfate was added to the solution and stirred vigorously. For oven heating, the mixture was placed into a Parr bomb (Parr Instrument Company, Moline, IL) and placed in an oven at 180 C for 15 h. For microwave

synthesis, the solution was placed into a Teflon vessel and tested at various conditions of temperature, pressure and duration. A MARS system from CEM Corporation (Matthews, NC) was used for microwave synthesis. Non-optimized conditions for synthesizing nanoparticles were found by heating at 180 C for 45 min at pressures below 200 psi. Optimal conditions were achieved by increasing the heating time to 1 h and using pressure setting greater than 300 psi.

5.2.3 Powder X-ray Diffraction and Elemental Analysis

To evaluate the composition of the $FeNi_3$ nanoparticles, powder X-ray diffraction was accomplished for dried thin films of nanoparticles with a Bruker DE Advance X-Diffractametor. The diffraction patterns show peaks that are consistent with a mixture of nanoparticles composed of iron oxide, $FeNi_3$ and nickel, with a predominance of $FeNi_3$. Crystallographic parameters and dominant peaks from samples of nanoparticles prepared with oven or microwave heating are shown in Table 5.1.

Table 5.1. Crystallographic parameters and dominant peaks

Heating method	Scan range (2θ)	Dominant peaks	Compound present	Temprature C
Oven	20-80^o	30.5, 36, 44.5, 52, 63, 76	$FeNi_3$, Fe_2O_3	25
Microwave	20-80^o	44.5, 52, 76	$FeNi_3$	25

Powder XRD spectra for the nanoparticle samples are shown in Figure 5.1. The top spectrum was acquired for nanoparticles produced by conventional oven heating (Figure 5.1A) after 15 h, and the bottom spectrum shows results for nanoparticles produced using microwave heating for 1 h (Figure 5.1B). Broad peaks at 44.2 and 52.5 2θ in the spectra of the oven-prepared sample confirms that $FeNi_3$ nanoparticles were produced with a cubic structure, however other peaks observed in the spectra indicates that Fe_2O_3 nanoparticles are also present. Comapared to microwave diffractor pattern, the broard dominate peaks observed confirmed the presence of iron(III) nickel.

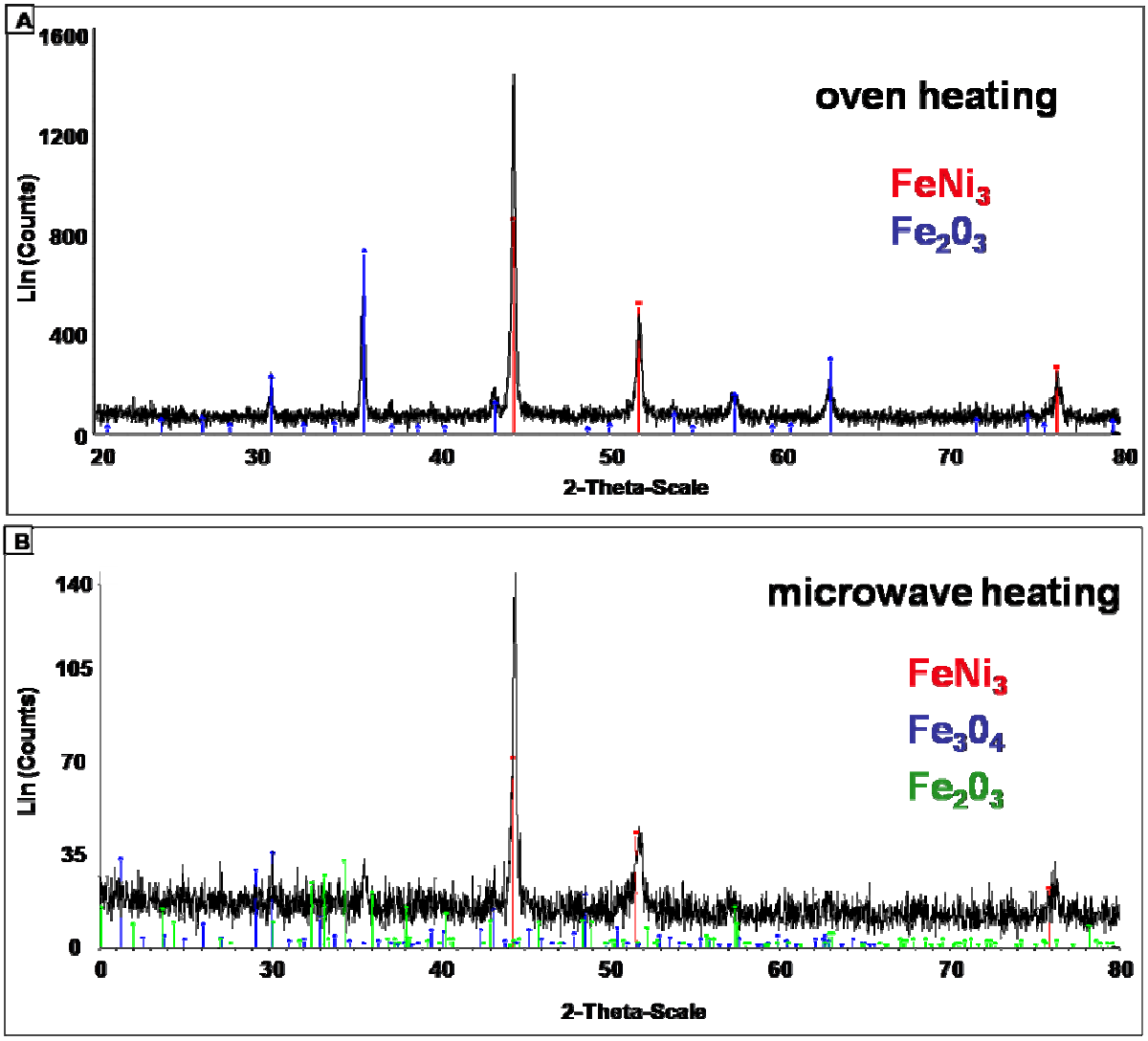

Figure 5.1. Powder X-ray diffraction spectra of iron-nickel nanoparticles. [A] Nanoparticles prepared by conventional oven heating; [B] sample synthesized with microwave heating.

The spectra also reveal that residual unreacted iron forms iron(III) oxide nanoparticles for both oven and microwave heated samples. We observed that when the nanoparticles are analyzed by XRD immediately after being synthesized, less Fe_2O_3 was detected, suggesting oxidation effect occur over time. Broadening of the diffraction peaks indicates the size of the powder is within the nanometer range. For the XRD pattern of iron(III)-nickel nanoparticles produced in an oven, the peaks have a greater intensity and are closer to 2θ values correlating to $FeNi_3$ as compared to the XRD spectra of nanoparticles prepared with microwave heating.

5.2.4 Atomic Force Microscopy (AFM)

Tapping-mode topography and phase imaging was accomplished using acoustic AC mode with an Agilent 5500 AFM/SPM equipped with Picoscan v. 5.3.3 software (Chandler, AZ). Samples were prepared by depositing 10 µL of sample onto either silicon or freshly cleaved mica surfaces which were then dried in air for at least 24 h. Figure 5.2 was acquired using silicon nitride tips from NanoSensors (Lady's Island, SC) with a resonance frequency ranging between 146-236 kHz. Images were processed using Gwyddion v.2.8.[310]

5.2.5 Magnetic Sample Modulation AFM

For magnetic AFM characterizations, the Agilent 5500 AFM scanner was operated for continuous contact-mode imaging while the flux of an alternating electromagnetic field was applied to the sample stage. A solid plastic nose cone without metal components was used as the tip holder assembly for AFM imaging, with soft silicon nitride cantilevers having force constants ranging from 0.5 to 0.1 N m^{-1} (Veeco Probes, Santa Barbara, CA). The MSM set-up is a hybrid of contact-mode AFM combined with selective actuation of magnetic samples (Figure 5.2).[311, 312]

A typical approach for imaging first involves acquiring conventional contact- mode topography images. Next, the same area of the surface is scanned again, however with an oscillating electromagnetic field applied via the sample stage with average field strength ranging between 0.01 to 0.4 T. The differences for images with and without an applied magnetic field are used to map magnetic areas. The polarity and flux of the magnetic field applied to the sample stage is generated and controlled by selection of parameters for the AC current applied to a wire coil solenoid located directly underneath the sample plate. When an electromagnetic field is applied to samples only the magnetic domains vibrate, providing selective contrast for magnetic areas that are in motion. Changes in the phase and amplitude of vibrating nanomaterials are mapped relative to the driving AC signal. Since a lock-in amplifier is used to

acquire the amplitude and phase components of the deflection signals, extreme sensitivity is achieved for slight changes in tip movement.

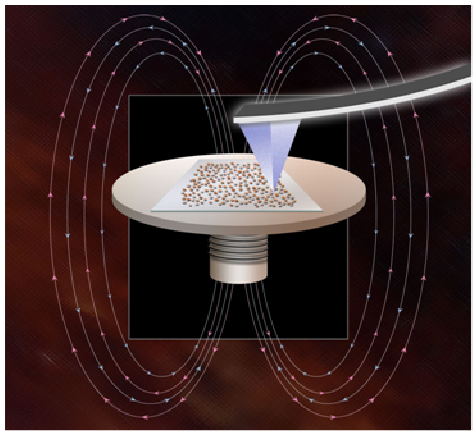

Figure 5.2. Imaging principle for AFM with magnetic sample modulation (MSM).

5.3 Results and Discussion

Although AFM-based characterizations can provide unprecedented resolution for evaluating the 3D morphology of nanoparticles on surfaces, it has the limitation of being chemically blind. For AFM images, relative differences in friction, surface adhesion and elastic compliance of samples can be obtained at the nanoscale, however accurate interpretation of images is contingent upon prior knowledge of the sample composition. Our goal for this investigation was to evaluate whether the newly developed approach for MSM imaging is capable of distinguishing changes in the composition of different systems of magnetic nanoparticles. Tapping-mode AFM provides dynamic characterizations of changes in elastic compliance, tip-sample adhesion and the Young's modulus at the nanoscale. However, tapping-mode does not provide insight about the magnetic properties of metal nanoparticles. For tapping-mode, the tip is driven to oscillate near its resonance frequency, and is brought intermittently into contact with the sample. The motion of the vibrating tip can be dampened by tip-surface adhesion and elasticity, resulting in changes for the amplitude and phase rhythm of

the tip trajectory. Digital images are generated by spatially mapping the changes in phase to provide a picture of the relative differences in surface composition. For this report, results from tapping-mode phase images are presented to corroborate MSM results that disclose compositional differences in mixed systems of nanoparticles.

An ideal, optimized protocol for nanoparticle synthesis with perfect stoichiometry and reaction conditions would achieve 100% yields of the desired composite nanoparticles. However, actual conditions will usually generate a mixture of iron, nickel and $FeNi_3$ nanoparticles, as shown with XRD analysis. We intentionally chose a synthetic protocol which produces a mixture of different magnetic nanoparticles to provide a means to evaluate whether MSM can be used to resolve small changes in the magnetic response of nanoparticles of differing composition.

5.3.1 Characterization of Nanoparticles by Tapping-mode AFM

Iron(III)-nickel nanoparticles were synthesized using either conventional oven heating or microwave synthesis under different conditions. Three different batches were prepared and imaged using tapping-mode AFM, as shown in Figure 5.3. The top panel (Figures 5.3A-5.3C) displays representative topography, phase and height distributions for nanoparticles prepared by oven heating in a pressure bomb. The topography and phase images reveal the shapes of ~ 34 nanoparticles, which have a uniform composition. The samples were diluted in water and dispersed on flat surfaces of freshly cleaved mica to provide local views of isolated nanoparticles. The phase image (Figure 5.3B) shows a homogeneous color for the nanoparticles which is evidence that the nanoparticles within this frame have a uniform $FeNi_3$ composition, and the results are confirmed by XRD spectra shown in Figure 5.1. The sizes of the oven-prepared batch of nanoparticles (Figure 5.3C) ranges from 2 to 12 nm, with a relatively narrow

distribution. Approximately 77% of the nanoparticles fall within the range of 4 to 6 nm in diameter.

When a batch of nanoparticles was prepared in a microwave under conditions of low pressure, changes in material composition became readily apparent with tapping-mode images. Figures 5.3D and 5.3E reveal a mixture of large and small nanoparticles were produced with near-spherical geometries. The phase image of Figure 5.3E displays different colors for the substrate and nanoparticles. The larger nanoparticles are dark whereas the smaller nanoparticles are brighter. The color assignments are assigned arbitrarily for these phase images, and do not reflect which surface is harder or softer. However, the phase images clearly evidence that the small and large nanoparticles have different material composition, which matches the results from XRD analysis. Under low pressure conditions, nanoparticles of both iron or nickel were produced, and the intermetallic nanoparticles were not observed to form. Likewise, the height histogram shows a bimodal distribution of nanoparticle diameters (Figure 5.3F) in which 86% of the nanoparticles are smaller, ranging from 2 to 6 nm in dimension while larger nanoparticles measured 10 nm in size. Analysis by XRD confirmed that $FeNi_3$ nanoparticles were not generated (Figure 5.1).

A third batch of nanoparticles was prepared with microwave heating under high pressure, shown in the bottom panel of Figure 5.3. There are ~ 27 nanoparticles within the $2 \times 2\ \mu m^2$ frames (Figures 5.3G - 5.3H), and the sizes appear to be mostly monodisperse. The phase image sensitively reveals that the smaller nanoparticles have a different contrast and composition. The sizes range from 2 to 8 nm, which is similar to the first batch of nanoparticles prepared by oven heating. Most of the nanoparticles (76%) are 4 to 6 nm in diameter (Figure 5.3I). Analysis of the sample with XRD shows a predominance of $FeNi_3$ nanoparticles were formed, with lesser quantities of iron oxide nanoparticles of Fe_2O_3 and Fe_3O_4.

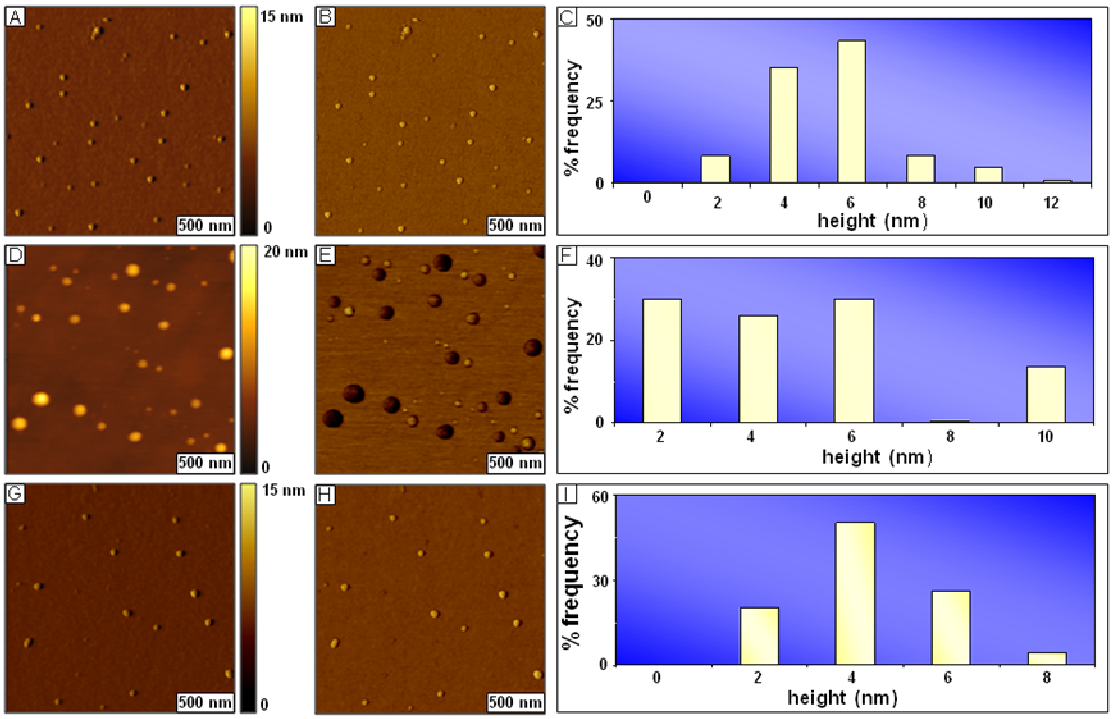

Figure 5.3. Comparison of nanoparticles prepared under different conditions. [A] intermetallic iron-nickel particles produced by heating in a conventional oven viewed with a tapping-mode topography image, 2 × 2 μm^2; [B] corresponding phase frame and [C] height histogram of nanoparticles obtained from cursor measurements, n=150. [D] Mixture of iron and nickel nanoparticles synthesized by microwave heating at low pressure viewed with a 2 × 2 μm^2 topograph; [E] simultaneously acquired phase image; [F] distribution of nanoparticle sizes, n=150. [G] $FeNi_3$ nanoparticles produced with microwave heating under optimized pressure and temperature viewed with a topography image, 2 × 2 μm^2; [H] corresponding phase image and [I] histogram of height measurements, n=150.

A comparison of the histogram data obtained from cursor height measurements of individual nanoparticles is displayed in Table 5.2. Significant differences are observed for the average sizes and distributions for each of the three batches of nanoparticles. A greater standard deviation was observed for the bimodal distribution of iron and nickel nanoparticles for the low pressure microwave synthesis. Interestingly, the average size of nanoparticles prepared by optimized microwave heating (3.5 nm) is smaller than the nanoparticles prepared in an oven after

12 hours of heating (4.7 nm). The larger nanoparticles most likely were generated over time, since the microwave batch was synthesized within only one hour of reaction.

Table 5.2. Comparison of nanoparticle sizes produced by oven or microwave heating

	Conventional heating	Microwave heating under low pressure	Microwave heating optimized
Average size (nm)	4.7	4.4	3.5
Standard deviation (nm)	1.9	2.3	1.5
Largest size (nm)	12	9.8	7.5
Smallest size (nm)	1.2	1.3	1.5
n	150	150	150

5.3.2 Characterizations of Nanoparticles with Magnetic Sample Modulation AFM

Instead of actuating the AFM tip for surface measurements with tapping-mode, the magnetic properties of nanoparticles themselves can be used for dynamic imaging by driving the sample to vibrate with the flux of an external AC electromagnetic field. Proof-of-concept results are presented in Figure 5.4 which illustrates the MSM imaging concept. Metal nanoparticles were imaged without an applied external electromagnetic field in the top panel of Figure 5.4, displaying the simultaneously acquired topography, phase and amplitude frames, respectively for a $5 \times 5\ \mu m^2$ area of the surface (Figures 5.4A, 5.4B, 5.4C). Without an electromagnetic field there is no change in the amplitude or phase of the scanning tip, and likewise the shapes and positions of nanoparticles cannot be distinguished. However, when the same area is scanned with the AC field applied (center panel, Figures 5.4D, 5.4E, 5.4F) the shapes and locations of nanoparticles are readily apparent in both phase and amplitude frames. The area was scanned with an average electromagnetic field strength of 0.2 Tesla with a driving frequency of 38.6 kHz. Both MSM channels sensitively detect sub-angstrom changes in AFM tip motion caused by vibration of nanoparticles. The MSM-amplitude and MSM-phase images clearly display the

prominent larger islands of nanoparticles with dark contrast that are obvious in the topography frames, however the locations and high density arrangements of tinier nanoparticles become readily apparent in MSM frames even with such broad magnification for a micron-sized area.

Spectra for frequency versus amplitude can be acquired for samples by carefully placing the AFM tip in contact with a vibrating area of the sample, as shown in Figure 5.4G under a minimal force. When the tip is disengaged from the surface, there are no prominent peaks detected for the baseline measurement, thus there is no response of the tip to the AC field. When the AFM probe is engaged, provided that the tip is placed in contact with the vibrating magnetic domain of the surface, the frequency can be swept to evaluate the resonance for sample actuation. The amplitude axis correlates directly with the z displacement of the AFM tip, and was found to range from 0 to 1.3 nm. A large broad resonance peak was observed between 35 and 45 kHz, and the frequency selected for MSM imaging was 38.6 kHz for Figure 5.4. Depending on the size of the nanoparticle under the tip, the frequency spectra can be quite variable. Investigations are currently in progress to systematically evaluate changes in resonance spectra versus nanoparticle sizes.

5.3.3 MSM Protocols with Varied Parameters of Frequency and Field Strength

The MSM approach offers unique capabilities to obtain information about the dynamic response of the actuated nanoparticles by changing the modulation frequency or field strength parameters. The driving frequency and magnetic field strength parameters can be systematically ramped to obtain rich information about the magnetic response of individual magnetic nanoparticles over time using MSM imaging. An experiment testing the changes in MSM images with frequency is shown in Figure 5.5.

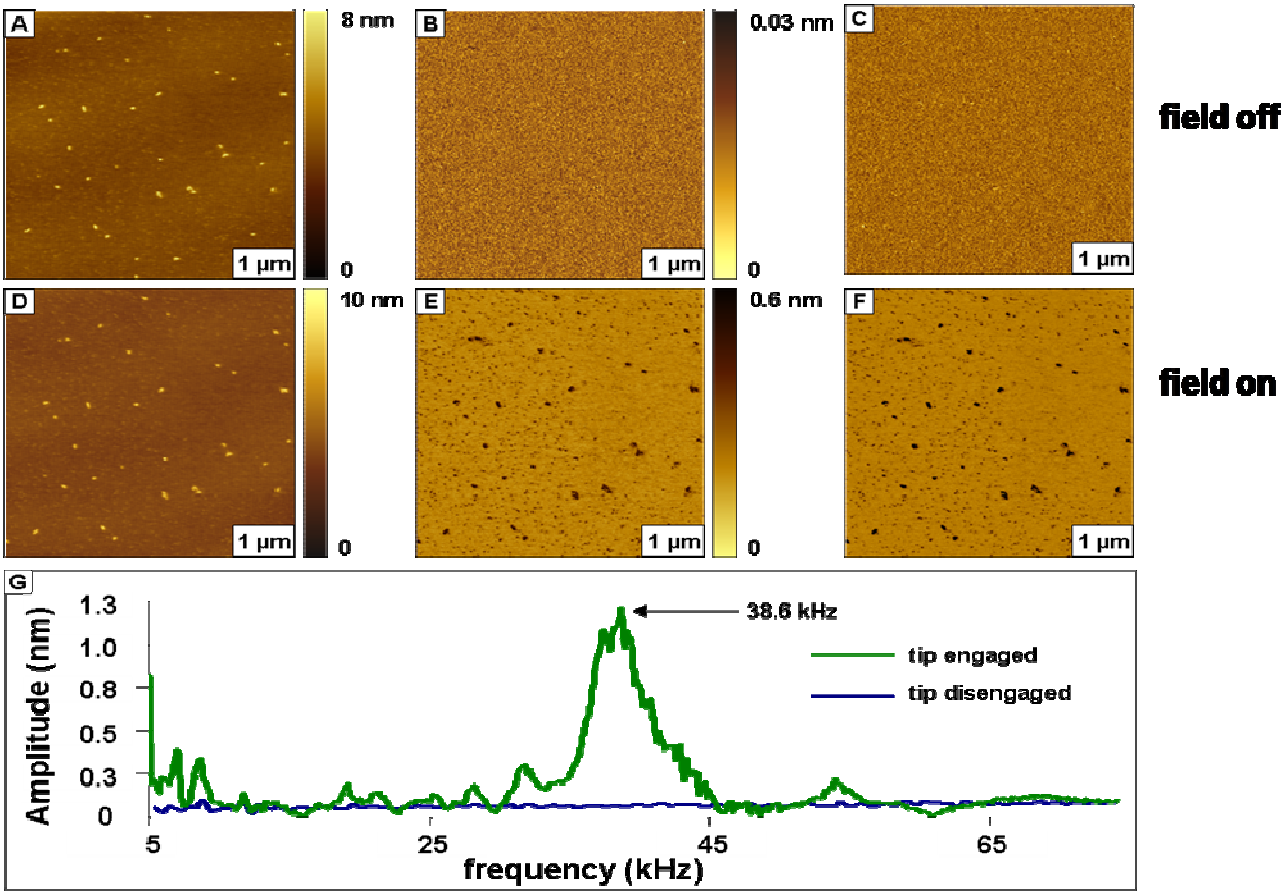

Figure 5.4. Response of iron(III)-nickel nanoparticles to magnetic sample modulation (MSM). [A] When the electromagnetic field is off the corresponding topography, [B] amplitude, and [C] phase images were acquired. Images acquired when an AC electromagnetic field was applied [A] MSM-topography, [B] MSM-amplitude and [C] MSM-phase images. [G] Frequency spectra showing the sample response when the tip is engaged and disengaged.

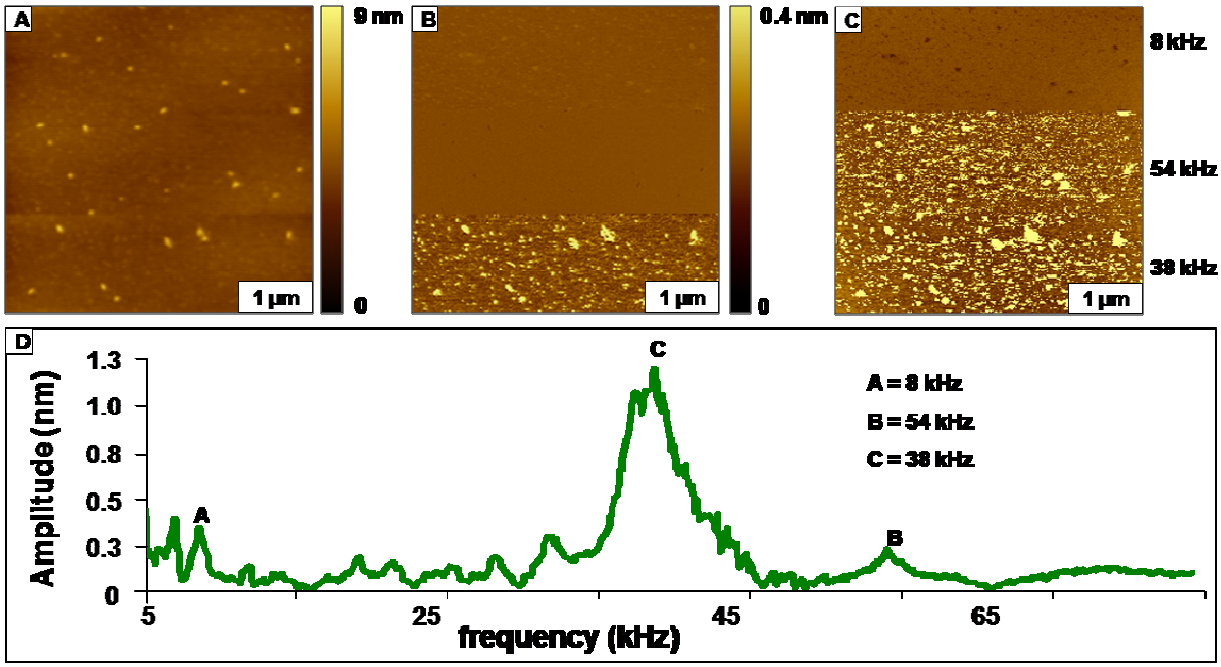

Figure 5.5. Results for MSM imaging using different frequencies to drive the sample oscillation. [A] Topography view (4.2 x 4.2 μm^2); [B] simultaneously acquired MSM-amplitude and [C] MSM-phase images. [D] Frequency spectra obtained for 0.1 T.

As the frequency is changed at designed increments during image acquisition with MSM, the vibrational amplitude of the nanoparticles changes accordingly. The amplitude responses shown in Figure 5.5B scale predictably with the magnitude of the resonances of the frequency plots. Optimized amplitude contrast is achieved at the resonance frequency of 38 kHz. Data for the tallest resonance peaks exhibit more intense vibration in the amplitude images of Figure 5.5B, whereas changes for the phase channel do not correlate directly with the scale of the peak magnitude. The data in Figure 5.5 were acquired with an average magnetic field strength of 0.1 T. Interestingly, the MSM-phase images of Figure 5.5C reveal details and contrast at frequencies that are not coincident with vibrational resonances, which is evidence that extreme local sensitivity can be achieved with nanoparticles with the using MSM imaging, at the level of angstrom level displacements of the AFM tip or smaller.

Changes for AFM images under conditions of different magnetic field strengths were investigated with MSM. The response of $FeNi_3$ nanoparticles to changes in the magnitude of the applied AC field is shown in Figure 5.6. Variations of the field strength between 0.05 to 3 T were captured within a single frame for the corresponding topography, MSM-amplitude and MSM-phase frames. As the field was incrementally ramped, increases in the vibrational response of the nanoparticles produced corresponding changes for both the amplitude and phase channels. As the field was increased, more nanoparticles become detectable for each segment of the phase and amplitude images. The greatest density of nanoparticles became apparent at the highest field strength, at the top sections of the images. Smaller nanoparticles are not detected at the lower field intensities, likely because there is not sufficient vibrational energy to perturb the motion of the tip until greater field strength is applied. The higher the magnetic field strength the greater the nanoparticles vibrate and the smaller nanoparticle deflections are more prominently captured and displayed in MSM-amplitude channel.

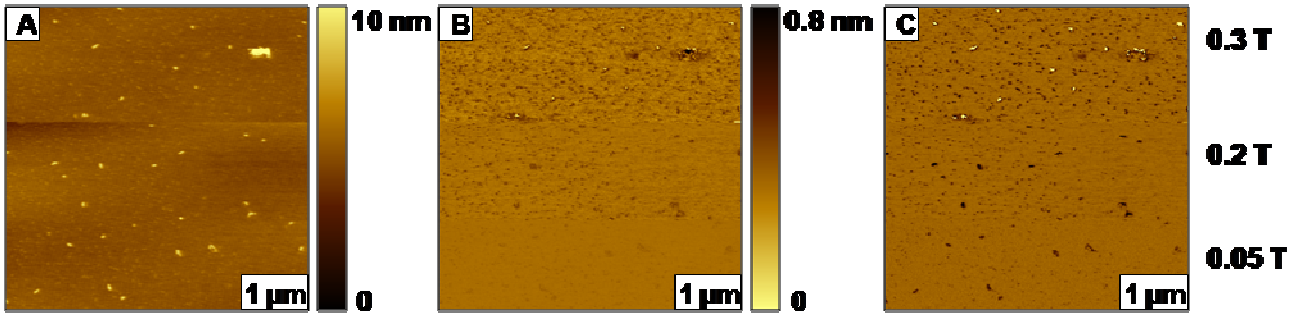

Figure 5.6. Varying magnetic field strength while scanning. [A] MSM-topography; [B] MSM-amplitude; and [C] MSM-phase images.

Interestingly, at higher AC fields of 0.3 T there is a contrast reversal for some of the larger nanoparticles. The colors flip so that the substrate is darker and the nanoparticles are bright, particularly for the larger aggregates of nanoparticles that are clustered together on the surface. This suggests that there is a shift or broadening of the vibrational resonance with greater

magnetization – the properties do not change, rather the resonance of the vibrational response is broader with increased vibrational motion.

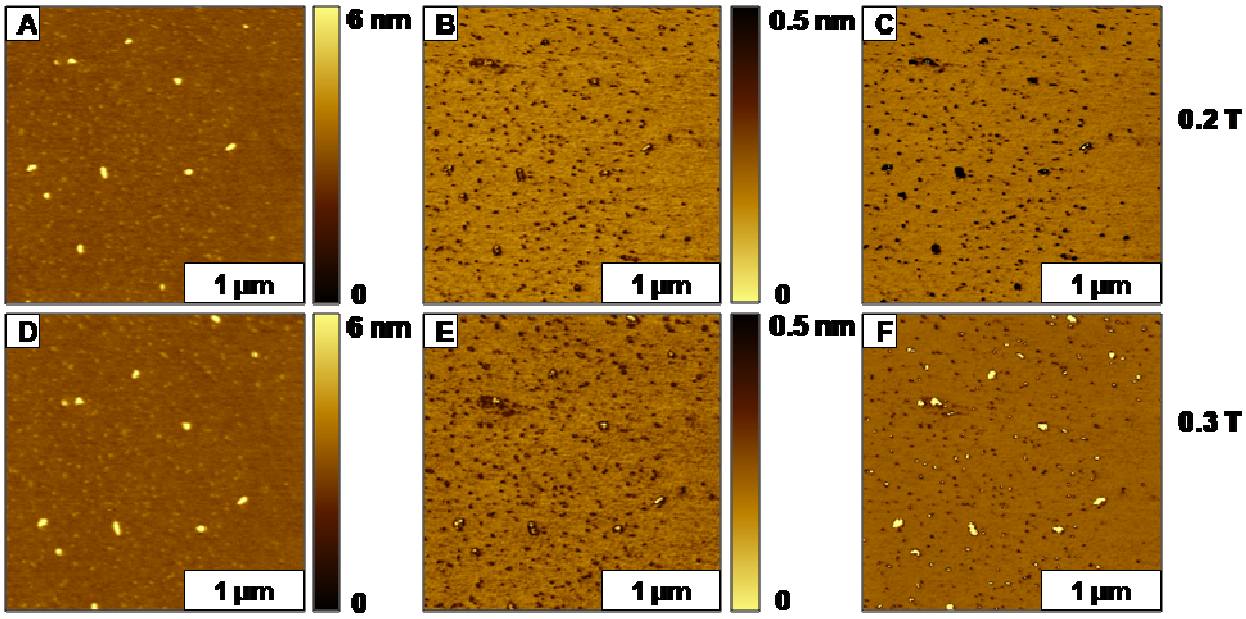

Figure 5.7. MSM images acquired at different electromagnetic field strengths within a 4.2 x 4.2 μm^2 scan area. Top panels were acquired at 0.2 T for [A] MSM-topography; [B] MSM-amplitude; and [C] MSM-phase images. Contrast reversal was consistently detected at higher field of 0.3 T as shown in [C] MSM-topography; [D] MSM-amplitude; and [E] MSM-phase frames of the bottom panel.

Further investigations of the contrast reversal are presented in Figure 5.7, to evaluate the reproducibility of this observation. Characterizations with MSM were accomplished by scanning a 2×2 μm^2 region with an applied average field strength of 0.2 T (Figures 5.6A, 5.6B and 5.6C) and also when using a field strength of 0.3 T (Figures 5.6D, 5.6E, and 5.6F). From prior knowledge of nanoparticle composition with the tapping-mode images and XRD spectra, it is likely that the smaller nanoparticles are composed of iron oxide, and the larger particles are successfully synthesized composite intermetallic $FeNi_3$ nanoparticles. With the MSM views of amplitude and phase changes there clearly is a lesser amplitude viewed for the smaller iron oxide nanoparticles, indicated by the lighter color. The darker spots with greater amplitude response

correlate to larger-sized nanoparticles of $FeNi_3$. Unfortunately, this is not a direct comparison of identically sized nanoparticles, so the role of nanoparticle size can be used to rationalize the changes in MSM amplitude and phase contrasts. It is also clear that the larger nanoparticles and aggregate areas of clusters of nanoparticles have stronger vibrational amplitude, while the smaller nanoparticles have smaller responses. A collective, additive effect of stronger magnetic vibration is detected when the nanoparticles are clustered together, as one would predict for mass magnetization effects of coupling nanomagnets together.

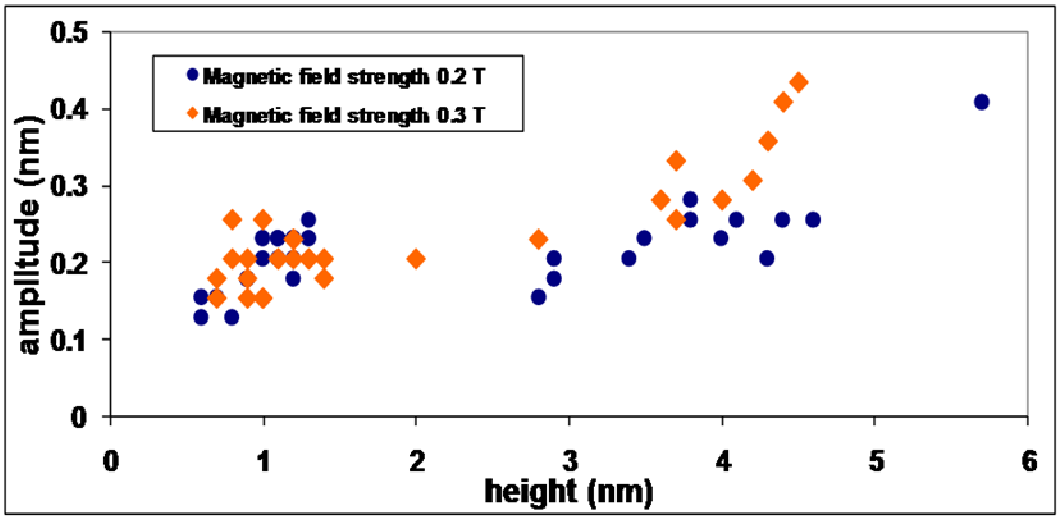

Figure 5.8. Comparison of the changes in average amplitude displacement of the tip caused by oscillation of nanoparticles with changes in the applied AC electromagnetic field measured from MSM-amplitude images.

The scaling relationship between the nanoparticle size and the magnetic response that is detected by the displacement of the AFM tip can be more quantitatively evaluated by plotting the amplitude versus nanoparticle diameter, as shown in Figure 5.8. Using the data from a single MSM-amplitude frame, the scaling behavior for 30 nanoparticles was plotted for measurments at 0.2 T and 0.3 T. At the lower field strength (blue circles) there is little difference in amplitude for particles ranging from 0.5 to 5 nm in diameter. However, when the field is ramped up to 0.3

T, the larger nanoparticles experience greater vibrational amplitude, and the mass magnetization effects for larger nanoparticles becomes apparent when the diameter is larger than 3 nm (orange diamonds).

5.4 Conclusion

When conducting AFM experiments, the dynamic conditions of the applied field strength, the force applied to the AFM probe and the frequency parameters can be systematically varied to visualize changes in the magnetic response of magnetic nanoparticles using MSM for characterizations at the level of individual nanoparticles. Changes of certain experimental parameters such as the driving frequency and the applied magnetic field strength directly influence the vibrational response of iron oxide and $FeNi_3$ nanoparticles when imaging with MSM. These preliminary results for mixtures of metal nanoparticles at the level of single nanoparticle measurements suggest intriguing new possibilities for characterizations with a hybrid MSM-AFM imaging mode and add a magnetic dimension to SPM methods for identification of magnetic nanomaterials. Although we have not satisfactorily addressed the question of whether MSM imaging can be used to discriminate differences in magnetic response for nanoparticles of different composition, it is clear that changes for different sized nanoparticles can be quantitatively evaluated. As with most measurements, the very small sizes of the nanoparticles pose a challenge for surface measurements, however, these results set a benchmark for detecting magnetic response for nanoparticles as small as 1.0 nm using the hybrid mode of MSM-AFM. We anticipate that using AFM tips with softer spring constants will provide a means to more clearly resolve differences for magnetic nanoparticles of different composition and size. In future experiments we plan to develop strategies to analyze mixtures of magnetic and non-magnetic nanomaterials or mixtures with different types of magnetic character, e.g. superparamagnetic versus ferromagnetic. Future quantitative protocols will be

developed for obtaining frequency sweeps for individual nanoparticles of different sizes under varied conditions of AC field strength and load force.

CHAPTER 6. SYNOPSIS AND FUTURE PROSPECTUS

Understanding and controlling molecular arrangement of molecules and nanomaterials on surfaces is a key step for successful fabrication of 3D nanostructures using bottom-up approaches. In Chapter 3, examples of nanografting were successfully demonstrated as a strategy for controlling the orientation of *n*-alkanethiols and α,ω-alkanedithiols within nanopatterns. Because of the effects of spatial confinement only crystalline phases (standing-up configuration) were observed to form for nanografted patterns of *n*-alkanethiols[211] and α,ω-alkanedithiols.[105, 313] Nanografting is accomplished with *in situ* AFM in liquid media containing thiols solution that are different from the matrix molecules of the surface. Following the trajectory of the AFM probe operated under small applied forces, molecules of the surface monolayer are displaced and are immediately replaced by new molecules from the surrounding solution.[38, 222, 314] Designed surfaces with local changes in surface properties are readily produced with nanografting. When α,ω-alkanedithiols form though natural self-assembly, a monolayer with a mixture of surface orientations were observed, where the majority of the molecules have both thiol groups chemisorbed to Au(111) and aligned parallel to the surface. However, when α,ω-alkanedithiols are nanografted, they directly adopt a standing up configuration with only one thiol group bound to the surface.[105] Alkanethiols with reactive head groups such as carboxyl and thiol were shown to form double layers when nanografted under certain conditions of concentration, however at low concentrations monolayers were produced. The precise mechanism for generating double layers is not fully understood, but based on results reported in Chapter 3, it is thought to occur by dimerization in solution prior to steps of nanografting.[313]

In a collaborative research project conducted at Eastman Kodak Company in Rochester, New York with Dr. Tommie L. Royster, dispersions of pigment nanoparticles were characterized using AFM, DLS and transmission spectrometry, as detailed in Chapter 4.[308] Organic pigment nanoparticles formulated in aqueous media remain well-dispersed and can therefore be used for inkjet printing.[262, 315-318] In contrast, formulating a dispersion composed of organic solvents and organic pigment nanoparticles with sizes smaller than 50 nm is a challenge because of self-aggregation. Chapter 4 describes development of a stable organic dispersion with dye nanoparticles smaller than 50 nm that was achieved by introduction of a synergist. In addition, an increase in aggregation of pigment nanoparticles diminishes the desired spectral properties. Spin-coated samples of the resulting dispersion were interrogated using AFM. At the end of the investigation, the organic dispersion was shown to be stable for three months; however, light aggregation among the nanoparticles were detected. Extending the stability to greater duration than three months with variations in the pigment concentration are directions for future investigations.

Development of methods to investigate the magnetic properties and measure the magnetic response of nanomaterials at fundamental size scales is important for both understanding the behavior of existing nanomaterials as well as for advancement in the development of new materials. Magnetic sample modulation (MSM), a newly developed AFM imaging mode, was applied for measuring the vibrational response of magnetic nanoparticles when the flux of an alternating electromagnetic field is applied to samples.[20,181] Described in Chapter 5, MSM was accomplished for iron(III)-nickel nanoparticles prepared on mica(0001). Varying the driving frequency and magnetic field strength of MSM provides new dynamic protocols for evaluating the magnetic response of iron oxide and $FeNi_3$ nanoparticles. Larger

nanoparticles were more easily detected with MSM imaging, whereas the smallest nanoparticles (1-2 nm diameter) required higher AC field strength to become visible.

The preliminary results in Chapter 5 demonstrating MSM imaging for mixtures of metal nanoparticles at the level of single nanoparticles add a magnetic dimension to SPM methods for identification of magnetic nanomaterials. Although we have not fully addressed the question of whether MSM imaging can be used to discriminate differences in magnetic response for nanoparticles of different composition, it is clear that changes for different sized nanoparticles can be quantitatively evaluated with exquisite sensitivity. The very small sizes of the nanoparticles (~ 1 nm) set a precedent for detecting magnetic response for ultra small nanoparticles using the hybrid mode of MSM-AFM. In future experiments we plan to develop strategies to analyze mixtures of magnetic and non-magnetic nanomaterials or mixtures with different types of magnetic character, e.g. superparamagnetic versus ferromagnetic.

A focus on chemical education was an integral component of the work described in this dissertation, with significant participation by several undergraduate researchers. My educational philosophy is that teaching should go beyond merely providing students with fixed concepts; rather, students should be taught how to critically and consciously reflect on the information set before them in order to arrive at the proper answer. Simply stated, an effective educator is one who must make sure that his pupils understand not only the 'whats', but also the 'wheres', 'whys', and 'hows' of the subject matter at hand. These are the educational ideals that I have employed as a graduate student, and I will continue to foster these principles in my academic life as a research professor.

REFERENCES

1. Butt, H. J.; Cappella, B.; Kappl, M., Force measurements with the atomic force microscope: Technique, interpretation and applications. *Surf. Sci. Rep.* **2005,** *59* (1-6), 1-152.

2. Hugel, T.; Seitz, M., The study of molecular interactions by AFM force spectroscopy. *Macromol. Rapid Commun.* **2001,** *22* (13), 989-1016.

3. Gimzewski, J. K.; Joachim, C., Nanoscale science of single molecules using local probes. *Science* **1999,** *283* (5408), 1683-1688.

4. Santos, N. C.; Castanho, M. A. R. B., An overview of the biophysical applications of atomic force microscopy. *Biophys. Chem.* **2004,** *107* (2), 133-149.

5. Muller, D. J.; Janovjak, H.; Lehto, T.; Kuerschner, L.; Anderson, K., Observing structure, function and assembly of single proteins by AFM. *Prog. Biophys. Mol. Biol.* **2002,** *79* (1-3), 1-43.

6. De Feyter, S.; De Schryver, F. C., Two-dimensional supramolecular self-assembly probed by scanning tunneling microscopy. *Chem. Soc. Rev.* **2003,** *32* (3), 139-150.

7. Gaboriaud, F.; Dufrene, Y. F., Atomic force microscopy of microbial cells: Application to nanomechanical properties, surface forces and molecular recognition forces. *Colloids Surf., B* **2007,** *54* (1), 10-19.

8. Palermo, V.; Liscio, A.; Palma, M.; Surin, M.; Lazzaroni, R.; Samori, P., Exploring nanoscale electrical and electronic properties of organic and polymeric functional materials by atomic force microscopy based approaches. *Chem. Commum.* **2007,** (32), 3326-3337.

9. Kramer, S.; Fuierer, R. R.; Gorman, C. B., Scanning probe lithography using self-assembled monolayers. *Chem. Rev.* **2003,** *103* (11), 4367-4418.

10. Wouters, D.; Schubert, U. S., Nanolithography and nanochemistry: Probe-related patterning techniques and chemical modification for nanometer-sized devices. *Angew. Chem. Int. Ed.* **2004,** *43* (19), 2480-2495.

11. Liu, M.; Amro, N. A.; Liu, G. Y., Nanografting for surface physical chemistry. *Annu. Rev. Phys. Chem.* **2008,** *59*, 367-386.

12. McCreery, R. L., Molecular electronic junctions. *Chem. Mater.* **2004,** *16* (23), 4477-4496.

13. Davis, J. J.; Morgan, D. A.; Wrathmell, C. L.; Axford, D. N.; Zhao, J.; Wang, N., Molecular bioelectronics. *J. Mater. Chem.* **2005,** *15* (22), 2160-2174.

14. Zotti, G.; Vercelli, B.; Berlin, A., Monolayers and multilayers of conjugated polymers as nanosized electronic components. *Acc. Chem. Res.* **2008,** *41* (9), 1098-1109.

15. Li, D.; Bonnell, D. A., Controlled patterning of ferroelectric domains: Fundamental concepts and applications. *Annu. Rev. Mater. Res.* **2008,** *38*, 351-368.

16. Xie, X. N.; Chung, H. J.; Sow, C. H.; Wee, A. T. S., Nanoscale materials patterning and engineering by atomic force microscopy nanolithography. *Mater. Sci. Eng., R* **2006,** *54* (1-2), 1-48.

17. Archakov, A. I.; Ivanov, Y. D., Analytical nanobiotechnology for medicine diagnostics. *Mol. Biosyst.* **2007,** *3* (5), 336-342.

18. Muller, D. J.; Dufrene, Y. F., Atomic force microscopy as a multifunctional molecular toolbox in nanobiotechnology. *Nat. Nanotechnol.* **2008,** *3* (5), 261-269.

19. Edwardson, J. M.; Henderson, R. M., Atomic force microscopy and drug discovery. *Drug Discovery Today* **2004,** *9* (2), 64-71.

20. Li, J.-R.; Lewandowski, B. R.; Xu, S.; Garno, J. C., Development of a new hybrid AFM imaging mode for selective mapping of magnetic nanomaterials. *Anal. Chem.* **2009,** *in submission*.

21. Daniels, S. L.; Ngunjiri, J. N.; Garno, J. C., Investigation of the magnetic properties of ferritin by combining AFM imaging with electromagnetic sample modulation. *Anal. Bioanal. Chem.* **2009,** *in press*.

22. Bhatia, S. K.; Hickman, J. J.; Ligler, F. S., New approach to producing patterned biomolecular assemblies. *J. Am. Chem. Soc.* **1992,** *114* (11), 4432-4433.

23. Delehanty, J. B.; Ligler, F. S., A microarray immunoassay for simultaneous detection of proteins and bacteria. *Anal. Chem.* **2002,** *74* (21), 5681-5687.

24. Xia, Y. N.; Whitesides, G. M., Soft lithography. *Annu. Rev. Mater. Sci.* **1998,** *28*, 153-184.

25. Shumaker-Parry, J. S.; Zareie, M. H.; Aebersold, R.; Campbell, C. T., Microspotting streptavidin and double-stranded DNA Arrays on gold for high-throughput studies of protein-DNA interactions by surface plasmon resonance microscopy. *Anal. Chem.* **2004,** *76* (4), 918-929.

26. Craighead, H. G.; Mankiewich, P. M., Ultra-small metal-particle arrays produced by high-resolution electron-beam lithography. *J. Appl. Phys.* **1982,** *53* (11), 7186-7188.

27. Pease, R. F. W., Nanolithography and its prospects as a manufacturing technology. *J. Vac. Sci. Technol. B* **1992,** *10* (1), 278-285.

28. Hulteen, J. C.; Vanduyne, R. P., Nanosphere Lithography - A materials general fabrication process for periodic particle array surfaces. *J. Vac. Sci. Technol. A-Vac. Surf. Films* **1995,** *13* (3), 1553-1558.

29. Li, J. R.; Garno, J. C., Elucidating the role of surface hydrolysis in preparing organosilane nanostructures via particle lithography. *Nano Letts.* **2008,** *8* (7), 1916-1922.

30. Li, J. R.; Garno, J. C., Nanostructures of octadecyltrisiloxane self-assembled monolayers produced on au(111) using particle lithography. *ACS Appl. Mater. Interfaces* **2009,** *1* (4), 969-976.

31. Li, J. R.; Lusker, K. L.; Yu, J. J.; Garno, J. C., Engineering the spatial selectivity of surfaces at the nanoscale using particle lithography combined with vapor deposition of organosilanes. *ACS Nano* **2009,** *3* (7), 2023-2035.

32. Xu, S.; Liu, G. Y., Nanometer-scale fabrication by simultaneous nanoshaving and molecular self-assembly. *Langmuir* **1997,** *13* (2), 127-129.

33. Liu, G. Y.; Xu, S.; Qian, Y. L., Nanofabrication of self-assembled monolayers using scanning probe lithography. *Acc. Chem. Res.* **2000,** *33* (7), 457-466.

34. Wouters, D.; Schubert, U. S., Large-scale local probe oxidation of OTS monolayers. *Nanotechnol.* **2007,** *18* (48).

35. Peter, M.; Li, X. M.; Huskens, J.; Reinhoudt, D. N., Catalytic probe lithography: Catalyst-functionalized scanning probes as nanopens for nanofabrication on self-assembled monolayers. *J. Am. Chem. Soc.* **2004,** *126* (37), 11684-11690.

36. Lee, K. B.; Park, S. J.; Mirkin, C. A.; Smith, J. C.; Mrksich, M., Protein nanoarrays generated by dip-pen nanolithography. *Science* **2002,** *295* (5560), 1702-1705.

37. Liu, G.-Y.; Xu, S.; Qian, Y., Nanofabrication of self-assembled monolayers using scanning probe lithography. *Acc. Chem. Res.* **2000,** *33*, 457-466.

38. Xu, S.; Liu, G. Y., Nanometer-scale fabrication by simultaneous nanoshaving and molecular self-assembly. *Langmuir* **1997,** *13*, 127-129.

39. Cresswell, S. L.; Haswell, S. J., Microwave ovens--out of the kitchen. *J. Chem. Educ.* **2001,** *78*, 900.

40. Parquet, E.; Lin, Q., Microwave assisted Wolff-Kishner reduction reaction. *J. Chem. Educ.* **1997,** *74*, 1225.

41. Shaw, R.; Severin, A.; Balfour, M.; Nettles, C., Diels-Alder cycloadditions: A more experiment in the organic laboratory including a diene identification exercise involving nmr spectroscopy and molecular modeling. *J. Chem. Educ.* **2005,** *82*, 625.

42. White, L. L.; Kittredge, K. W., A Microwave-assisted reduction of cyclohexanone using solid-state-supported sodium borohydride. *J. Chem. Educ.* **2005,** *82*, 1055.

43. Trehan, I. R.; Brar, J. S.; Arora, A. K.; Kad, G. L., Fries Rearrangement accelerated by microwave radiation in the undergraduate organic laboratory. *J. Chem. Educ.* **1997,** *74*, 324.

44. Mirafzal, G. A.; Summer, J. M., microwave irradiation reactions: synthesis of analgesic drugs. *J. Chem. Educ.* **2000,** *77*, 356.

45. Ardon, M.; Hayes, P. D.; Hogarth, G., Microwave-assisted reflux in organometallic chemistry: synthesis and structural determination of molybdenum carbonyl complexes. an intermediate-level organometallic–inorganic experiment. *J. Chem. Educ.* **2002,** *79*, 1249.

46. Kennedy Sr., A. P., Determination of enthalpy of vaporization using a microwave oven. *J. Chem. Educ.* **1997,** *74*, 1231.

47. Freeman, R. G.; McCurdy, D., Using microwave sample decomposition in undergraduate Anal. Chem.. *J. Chem. Educ.* **1998,** *75*, 1033.

48. Sheffield, M.-C.; Nahir, T. M., Analysis of selenium in brazil nuts by microwave digestion and fluorescence detection. *J. Chem. Educ.* **2002,** *79*, 1345.

49. Carmosini, N.; Ghoreshy, S.; Koether, M. C., The gravimetric analysis of nickel using a microwave oven. *J. Chem. Educ.* **1997,** *74*, 986.

50. Butt, H. J.; Cappella, B.; Kappl, M., Force measurements with the atomic force microscope: Technique, interpretation and applications. *Surf. Sci. Rep.* **2005,** *59* (1-6), 1-152.

51. vanderVegte, E. W.; Hadziioannou, G., Scanning force microscopy with chemical specificity: An extensive study of chemically specific tip-surface interactions and the chemical imaging of surface functional groups. *Langmuir* **1997,** *13*, 4357-4368.

52. Greene, M. E.; Kinser, C. R.; Kramer, D. E.; Pingree, L. S. C.; Hersam, M. C., Application of scanning probe microscopy to the characterization and fabrication of hybrid nanomaterials. *Microsc. Res. Tech.* **2004,** *64* (5-6), 415-434.

53. Grimsdale, A. C.; Mullen, K., The chemistry of organic nanomaterials. *Angew. Chem. Int. Ed.* **2005,** *44* (35), 5592-5629.

54. Binnig, G.; Rohrer, H.; Gerber, C.; Weibel, E., Tunneling through a controllable vacuum gap. *Appl. Phys. Lett.* **1982,** *40* (2), 178-180.

55. Binnig, G.; Quate, C. F.; Gerber, C., Atomic force microscope. *Phys. Rev. Lett.* **1986,** *56* (9), 930-933.

56. Wiesendanger, R., *Scanning probe microscopy and specroscopy*. Cambridge University Press: Cambridge, United Kingdom, 1994.

57. Radmacher, M.; Tillmann, R. W.; Fritz, M.; Gaub, H. E., From molecules to cells - imaging soft samples with the atomic force microscope. *Science* **1992,** *257* (5078), 1900-1905.

58. Drake, B.; Prater, C. B.; Weisenhorn, A. L.; Gould, S. A. C.; Albrecht, T. R.; Quate, C. F.; Cannell, D. S.; Hansma, H. G.; Hansma, P. K., Imaging crystals, polymers, and processes in water with the atomic force microscope. *Science* **1989,** *243* (4898), 1586-1589.

59. Tsukruk, V. V., Scanning probe microscopy of polymer surfaces. *Rubber Chem. Technol.* **1997,** *70* (3), 430-467.

60. Hansma, P. K.; Elings, V. B.; Marti, O.; Bracker, C. E., Scanning tunneling microscopy and atomic force microscopy - application to biology and technology. *Science* **1988,** *242* (4876), 209-216.

61. Schitter, G.; Menold, P.; Knapp, H. F.; Allgower, F.; Stemmer, A., High performance feedback for fast scanning atomic force microscopes. *Rev. Sci. Instrum.* **2001,** *72* (8), 3320-3327.

62. Ando, T.; Kodera, N.; Takai, E.; Maruyama, D.; Saito, K.; Toda, A., A high-speed atomic force microscope for studying biological macromolecules. *Proc. Nat. Acad. Sci. U.S.A.* **2001,** *98* (22), 12468-12472.

63. Schitter, G.; Allgower, F.; Stemmer, A., A new control strategy for high-speed atomic force miciroscopy. *Nanotechnol.* **2004,** *15* (1), 108-114.

64. Schitter, G.; Stark, R. W.; Stemmer, A., Fast contact-mode atomic force microscopy on biological specimen by model-based control. *Ultramicrosc.* **2004,** *100* (3-4), 253-257.

65. Zhong, Q.; Inniss, D.; Kjoller, K.; Elings, V. B., Fractured polymer silica fiber surface studied by tapping mode atomic-force microscopy. *Surf. Sci.* **1993,** *290* (1-2), L688-L692.

66. Putman, C. A. J.; Van der Werf, K. O.; De Grooth, B. G.; Van Hulst, N. F.; Greve, J., Tapping mode atomic-force microscopy in liquid. *Appl. Phys. Lett.* **1994,** *64* (18), 2454-2456.

67. Hansma, P. K.; Cleveland, J. P.; Radmacher, M.; Walters, D. A.; Hillner, P. E.; Bezanilla, M.; Fritz, M.; Vie, D.; Hansma, H. G.; Prater, C. B.; Massie, J.; Fukunaga, L.; Gurley, J.; Elings, V., Tapping mode atomic-force microscopy in liquids. *Appl. Phys. Lett.* **1994,** *64* (13), 1738-1740.

68. Tamayo, J.; Garcia, R., Deformation, contact time, and phase contrast in tapping mode scanning force microscopy. *Langmuir* **1996,** *12* (18), 4430-4435.

69. Moller, C.; Allen, M.; Elings, V.; Engel, A.; Muller, D. J., Tapping-mode atomic force microscopy produces faithful high-resolution images of protein surfaces. *Biophys. J.* **1999,** *77* (2), 1150-1158.

70. Thomson, N. H.; Fritz, M.; Radmacher, M.; Cleveland, J. P.; Schmidt, C. F.; Hansma, P. K., Protein tracking and detection of protein motion using atomic force microscopy. *Biophys. J.* **1996,** *70* (5), 2421-2431.

71. Kasas, S.; Thomson, N. H.; Smith, B. L.; Hansma, H. G.; Zhu, X.; Guthold, M.; Bustamante, C.; Kool, E. T.; Kashlev, M.; Hansma, P. K., Escherichia coli RNA polymerase activity observed using atomic force microscopy. *Biochemistry* **1997,** *36* (3), 461-468.

72. Gosal, W. S.; Myers, S. L.; Radford, S. E.; Thomson, N. H., Amyloid under the atomic force microscope. *Protein Pept. Lett.* **2006,** *13* (3), 261-270.

73. Stark, M.; Moller, C.; Muller, D. J.; Guckenberger, R., From images to interactions: High-resolution phase imaging in tapping-mode atomic force microscopy. *Biophys. J.* **2001,** *80* (6), 3009-3018.

74. Hierlemann, A.; Campbell, J. K.; Baker, L. A.; Crooks, R. M.; Ricco, A. J., Structural distortion of dendrimers on gold surfaces: A tapping-mode AFM investigation. *J. Am. Chem. Soc.* **1998,** *120* (21), 5323-5324.

75. Raghavan, D.; Gu, X.; Nguyen, T.; Van Landingham, M.; Karim, A., Mapping polymer heterogeneity using atomic force microscopy phase imaging and nanoscale indentation. *Macromol.* **2000,** *33* (7), 2573-2583.

76. Xia, Y. N.; Whitesides, G. M., Soft lithography. *Annu. Rev. Mater. Sci.* **1998,** *28*, 153-184.

77. Xia, Y. N.; Rogers, J. A.; Paul, K. E.; Whitesides, G. M., Unconventional methods for fabricating and patterning nanostructures. *Chem. Rev.* **1999,** *99* (7), 1823-1848.

78. Smith, R. K.; Lewis, P. A.; Weiss, P. S., Patterning self-assembled monolayers. *Prog. Surf. Sci.* **2004,** *75* (1-2), 1-68.

79. Dubois, L. H.; Nuzzo, R. G., Synthesis, structure and properties of model organic-surfaces. *Annu. Rev. Mater. Sci.* **1992,** *43*, 437-463.

80. Whitesides, G. M.; Laibinis, P. E., Wet chemical approaches to the characterization of organic surfaces: self-assembled monolayers, wetting, and the physical-organic chemistry of the solid-liquid interface *Langmuir* **1990,** *6* (1), 87-96.

81. Laibinis, P. E.; Whitesides, G. M., Self-assembled monolayers of n-alkanethiolates on copper are barrier films that protect the metal against oxidation by air. *J. Am. Chem. Soc.* **1992,** *114* (23), 9022-9028.

82. Dimilla, P. A.; Folkers, J. P.; Biebuyck, H. A.; Harter, R.; Lopez, G. P.; Whitesides, G. M., Wetting and protein adsorption of self-assembled monolayers of alkanethiolates supported on transparent films of gold. *J. Am. Chem. Soc.* **1994,** *116* (5), 2225-2226.

83. Crooks, R. M.; Ricco, A. J., New organic materials suitable for use in chemical sensor arrays. *Acc. Chem. Res.* **1998,** (31), 219.

84. Flink, S.; Van Veggel, F.; Reinhoudt, D. N., Sensor functionalities in self-assembled monolayers. *Adv. Mater.* **2000,** *12* (18), 1315-1328.

85. Willner, I.; Katz, E., Integration of layered redox proteins and conductive supports for bioelectronic applications. *Angew. Chem. Int. Ed.* **2000,** *39* (7), 1180-1218.

86. Tour, J. M., Molecular electronics. Synthesis and testing of components. *Acc. Chem. Res.* **2000,** *33* (11), 791-804.

87. Joachim, C.; Gimzewski, J. K.; Aviram, A., Electronics using hybrid-molecular and mono-molecular devices. *Nature* **2000,** *408* (6812), 541-548.

88. Sagiv, J., Organized monolayers by adsorption . 1. Formation and structure of oleophobic mixed monolayers on solid-surfaces. *J. Am. Chem. Soc.* **1980,** *102* (1), 92-98.

89. Poirier, G. E., Characterization of organosulfur molecular monolayers on Au(111) using scanning tunneling microscopy. *Chem. Rev.* **1997,** *97* (4), 1117-1127.

90. Liu, Y.; Mu, L.; Liu, B. H.; Kong, J. L., Controlled switchable surface. *Chem. Eur. J.* **2005,** *11* (9), 2622-2631.

91. Laibinis, P. E.; Whitesides, G. M.; Allara, D. L.; Tao, Y. T.; Parikh, A. N.; Nuzzo, R. G., Comparison of the structures and wetting properties of self-assembled monolayers of normal-

alkanethiols on the coinage metal-surfaces, Cu, Ag, Au. *J. Am. Chem. Soc.* **1991,** *113* (19), 7152-7167.

92. Love, J. C.; Estroff, L. A.; Kriebel, J. K.; Nuzzo, R. G.; Whitesides, G. M., Self-assembled monolayers of thiolates on metals as a form of nanotechnology. *Chem. Rev.* **2005,** *105* (4), 1103-1169.

93. Shaporenko, A.; Ulman, A.; Terfort, A.; Zharnikov, A., Self-assembled monolayers of alkaneselenolates on (111) gold and silver. *J. Phys. Chem. B* **2005,** *109* (9), 3898-3906.

94. Ulman, A., *An introduction to ultrathin organic films from Langmuir-Blodgett to self-assembly*. Academic Press, New York: 1991.

95. Schreiber, F., Structure and growth of self-assembling monolayers. *Prog. Surf. Sci.* **2000,** *65*, 151-257.

96. Ulman, A., Formation and structure of self-assembled monolayers. *Chem. Rev.* **1996,** *96* (4), 1533-1554.

97. Fendler, J. H., Chemical self-assembly for electronic applications. *Chem. Mater.* **2001,** *13* (10), 3196-3210.

98. Willey, T.; Vance, A.; Fadley, C. S., Rapid degradation of alkanethiol-based self-assembled monolayers on gold in ambient laboratory conditions. *Surf. Sci.* **2005,** *567*, 188-196.

99. Poirier, G. E.; Pylant, E. D., The Self-Assembly Mechanism of Alkanethiols on Au(111). *Science* **1996,** *272*, 1145-1148.

100. Poirier, G. E., Coverage-dependent phases and phase stability of decanethiol on Au(111). *Langmuir* **1999,** *15*, 1167-1175.

101. Yang, G. H.; Liu, G.-Y., New insights for self-assembled monolayers of organothiols on Au(111) revealed by scanning tunneling microscopy. *J. Phys. Chem. B* **2003,** *107* (34), 8746-8759.

102. Willey, T. M.; Vance, A. L.; van Buuren, T.; Bostedt, C.; Terminello, L. J.; Fadley, C. S., Rapid degradation of alkanethiol-based self-assembled monolayers on gold in ambient laboratory conditions. *Surf. Sci.* **2005,** *576* (1-3), 188-196.

103. Barrena, E.; Ocal, C.; Salmeron, M., Molecular packing changes of alkanethiols monolayers on Au(111) under applied pressure. *J. Chem. Phys.* **2000,** *113* (6), 2413-2418.

104. Barrena, E.; Ocal, C.; Salmeron, M., Structure and stability of tilted-chain phases of alkanethiols on Au(111). *J. Chem. Phys.* **2001,** *114* (9), 4210-4214.

105. Yu, J.-J.; Ngunjiri, J. N.; Kelley, A. T.; Garno, J. C., Nanografting versus solution self-assembly of α,ω-alkanedithiols on Au(111) investigated by AFM. *Langmuir* **2008,** *24* (20), 11661-11668.

106. Liang, J.; Rosa, L. G.; Scoles, G., Nanostructuring, imaging and molecular manipulation of dithiol monolayers on Au(111) surfaces by atomic force microscopy. *J. Phys. Chem. C* **2007,** *111* (46), 17275-17284.

107. Nuzzo, R. G.; Korenic, E. M.; Dubois, L. H., Studies of the temperature-dependent phase-behavior of long-chain normal-alkyl thiol monolayers on gold. *J. Chem. Phys.* **1990,** *93* (1), 767-773.

108. Himmelhaus, M.; Gauss, I.; Buck, M.; Eisert, F.; Woll, C.; Grunze, M., Adsorption of docosanethiol from solution on polycrystalline silver surfaces: an XPS and NEXAFS study. *J. Electron. Spectrosc. Relat. Phenom.* **1998,** *92* (1-3), 139-149.

109. Tillman, N.; Ulman, A.; Schildkraut, J. S.; Penner, T. L., Incorporation of phenoxy groups in self-assembled monolayers of trichlorosilane derivatives - effects on film thickness, wettability and molecular-orientation. *J. Am. Chem. Soc.* **1988,** *110* (18), 6136-6144.

110. Peanasky, J.; Schneider, H. M.; Granick, S.; Kessel, C. R., Self-assembled monolayers on mica for experiments utilizing the surface forces apparatus. *Langmuir* **1995,** *11* (3), 953-962.

111. Schwartz, D. K.; Steinberg, S.; Israelachvili, J.; Zasadzinski, J. A. N., Growth of a self-assembled monolayer by fractal aggregation. *Phys. Rev. Lett.* **1992,** *69* (23), 3354-3357.

112. Lavrich, D.; Wetterer, S.; Bernasek, S.; Scoles, G., Physisorption and chemisorption of alkanethiols and alkylsulfides on Au (111). *J. Phys. Chem. B.* **1998,** *102* (18), 3456-3465.

113. Xu, S.; Cruchon-Dupeyrat, S. J. N.; Garno, J. C.; Liu, G. Y.; Jennings, G. K.; Yong, T. H.; Laibinis, P. E., In situ studies of thiol self-assembly on gold from solution using atomic force microscopy. *J. Chem. Phys.* **1998,** *108*, 5002-5012.

114. Schreiber, F., Self-assembled monolayers: from ''simple'' model systems to biofunctionalized interfaces. *J. Phys.: Condens. Matter* **2004,** *16*, R881-R900.

115. Porter, M. D.; Bright, T. B.; Allara, D. L.; Chidsey, C. E. D., Spontaneously organized molecular assemblies .4. Structural characterization of normal-alkyl thiol monolayers on gold by optical ellipsometry, infrared-spectroscopy and electrochemistry. *J. Am. Chem. Soc.* **1987,** *109* (12), 3559-3568.

116. Fenter, P.; Eberhardt, A.; Liang, K. S.; Eisenberger, P., Epitaxy and chainlength dependent strain in self-assembled monolayers. *J. Chem. Phys.* **1997,** *106* (4), 1600-1608.

117. Poirier, G. E., Mechanism of Formation of Au Vacancy Islands in Alkanethiol Monolayers on Au(111). *Langmuir* **1997,** *13*, 2019.

118. Qian, Y. L.; Yang, G. H.; Yu, J. J.; Jung, T. A.; Liu, G.-Y., Structures of annealed decanethiol self-assembled monolayers on Au(111): An ultrahigh vacuum scanning tunneling microscopy study. *Langmuir* **2003,** *19* (15), 6056-6065.

119. Camillone, N.; Eisenberger, P.; Leung, T. Y. B.; Schwartz, P.; Scoles, G.; Poirier, G. E.; Tarlov, M. J., New monolayer phases of n-alkane thiols self-assembled on Au(111) - preparation, surface characterization, and imaging. *J. Chem. Phys.* **1994,** *101* (12), 11031-11036.

120. Vieu, C.; Carcenac, F.; Pépin, A.; Chen, Y.; Mejias, M.; Lebib, A.; Manin-Ferlazzo, L.; Couraud, L.; Launois, H., Electron beam lithography: resolution limits and applications. *Appl. Surf. Sci.* **2000,** *164* (1-4), 111-117.

121. Gölzhäuser, A.; Eck, W.; Geyer, W.; Stadler, V.; Thomas Weimann; Hinze, P.; Grunze, M., Chemical nanolithography with electron beams. *Adv. Mater.* **2001,** *13* (11), 806-809.

122. Smith, H. I.; Schattenburg, M. L.; Hector, S. D.; Ferrera, J.; Moon, E. E.; Yang, I. Y.; Burkhardt, M., X-ray nanolithography: Extension to the limits of the lithographic process *Microelectron. Eng.* **1996,** *32* (1-4), 143-158.

123. Smith, H. I.; Schattenburg, M. L., X-Ray Lithography, from 500 to 30 nm - X-ray Nanolithography. *IBM J. Res. Development* **1993,** *37* (3), 319-329.

124. Pallandre, A.; Glinel, K.; Jonas, A. M.; Nysten, B., Binary nanopatterned surfaces prepared from silane monolayers. *Nano Lett.* **2004,** *4* (2), 365-371.

125. Mendes, P. M.; Preece, J. A., Precision chemical engineering: integrating nanolithography and nanoassembly. *Curr. Opin. Colloid Interface Sci.* **2004,** *9*, 236-248.

126. Zharnikov, M.; Grunze, M., Modification of thiol-derived self-assembling monolayers by electron and x-ray irradiation: Scientific and lithographic aspects. *J. Vac. Sci. Technol. B* **2002,** *20* (5), 1793-1807.

127. Li, J.-R.; Garno, J. C., Elucidating the role of surface hydrolysis in preparing organosilane nanostructures via particle lithography. *Nano Lett.* **2008,** *8* (7), 1916-1922.

128. Li, J.-R.; Henry, G. C.; Garno, J. C., Fabrication of nanopatterned films of bovine serum albumin and staphylococcal protein A using latex particle lithography *Analyst* **2006,** *131* (2), 244-250.

129. Ngunjiri, J. N.; Daniels, S. L.; Li, J.-R.; Serem, W. K.; Garno, J. C., Controlling the surface coverage and arrangement of proteins using particle lithography. *Nanomedicine* **2008,** *3* (4), 529-541.

130. Garno, J. C.; Amro, N. A.; Wadu-Mesthrige, K.; Liu, G.-Y., Production of periodic arrays of protein nanostructures using particle lithography. *Langmuir* **2002,** *18* (21), 8186-8192.

131. Yang, S.-M.; Jang, S. G.; Choi, D.-G.; Kim, S.; Yu, K. H., Nanomachining by colloidal lithography. *Small* **2006,** *2* (4), 458-475.

132. Cai, Y. G.; Ocko, B. M., Large-scale fabrication of protein nanoarrays based on nanosphere lithography *Langmuir* **2005,** *21* (20), 9274-9279.

133. Hulteen, J. C.; VanDuyne, R. P., Nanosphere Lithography - A materials general fabrication process for periodic particle array surfaces. *J. Vac. Sci. Technol. A* **1995,** *13* (3), 1553-1558.

134. Haynes, C. L.; Van Duyne, R. P., Nanosphere lithography: A versatile nanofabrication tool for studies of size-dependent nanoparticle optics *J. Phys. Chem. B* **2001,** *105* (24), 5599-5611.

135. Xie, X. N.; Chung, H. J.; Sow, C. H.; Wee, A. T. S., Nanoscale materials patterning and engineering by atomic force microscopy nanolithography. *Mater. Sci. Eng., R.* **2006,** *54* (1-2), 1-48.

136. Quate, C. F., Scanning probes as a lithography tool for nanostructures. *Surf. Sci.* **1997,** *386* (1-3), 259-264.

137. Lyo, I. W.; Avouris, P., Field-induced nanometer-scale to atomic-scale manipulation of silicon surfaces with the STM. *Science* **1991,** *253* (5016), 173-176.

138. Ho, W., Single-molecule chemistry. *J. Chem. Phys.* **2002,** *117* (24), 11033-11061.

139. Stipe, B. C.; Rezaei, M. A.; Ho, W., Single-molecule vibrational spectroscopy and microscopy. *Science* **1998,** *280* (5370), 1732-1735.

140. Eigler, D. M.; Schweizer, E. K., Positioning single atoms with a scanning tunneling microscope. *Nature* **1990,** *344* (6266), 524-526.

141. Jaschke, M.; Butt, H. J., Deposition of Organic Material by the Tip of a Scanning Force Microscope *Langmuir* **1995,** *11* (4), 1061-1064.

142. Piner, R. D.; Zhu, J.; Xu, F.; Hong, S. H.; Mirkin, C. A., Dip-Pen Nanolithography. *Science* **1999,** *283*, 661.

143. Salaita, K.; Wang, Y. H.; Mirkin, C. A., Applications of dip-pen nanolithography. *Nature Nanotechnol.* **2007,** *2* (3), 145-155.

144. Calleja, M.; Garcia, R., Nano-oxidation of silicon surfaces by noncontact atomic-force microscopy: Size dependence on voltage and pulse duration. *Appl. Phys. Lett.* **2000,** *76* (23), 3427-3429.

145. Held, R.; Vancura, T.; Heinzel, T.; Ensslin, K.; Holland, M.; Wegscheider, W., In-plane gates and nanostructures fabricated by direct oxidation of semiconductor heterostructures with an atomic force microscope. *App. Phys. Letts.* **1998,** *73* (2), 262-264.

146. Garcia, R.; Martinez, R. V.; Martinez, J., Nano-chemistry and scanning probe nanolithographies. *Chem. Soc. Rev.* **2005,** *35*, 29-38.

147. Xie, X. N.; Chung, H. J.; Sow, C. H.; Wee, A. T. S., Nanoscale materials patterning and engineering by atomic force microscopy nanolithography. *Mater. Sci. Eng., R* **2006,** *54* (1-2), 1-48.

148. Blackledge, C.; Engebretson, D. A.; McDonald, J. D., Nanoscale site-selective catalysis of surface assemblies by palladium-coated atomic force microscopy tips: Chemical lithography without electrical current. *Langmuir* **2000,** *16* (22), 8317-8323.

149. Hua, Y.; King, W. P.; Henderson, C. L., Nanopatterning materials using area selective atomic layer deposition in conjunction with thermochemical surface modification via heated AFM cantilever probe lithography. *Microelectron. Eng.* **2008,** *85*, 934-936.

150. Sheehan, P. E.; Whitman, L. J.; King, W. P.; Nelson, B. A., Nanoscale deposition of solid inks via thermal dip pen nanolithography. *Appl. Phys. Lett.* **2004,** *85*, 1589-1591.

151. Yang, M.; Sheehan, P. E.; King, W. P.; Whitman, L. J., Direct writing of a conducting polymer with molecular-level control of physical dimensions and orientation. *J. Am. Chem. Soc.* **2006,** *128*, 6774-6775.

152. Bakbak, S.; Leech, P. J.; Carson, B. E.; Saxena, S.; King, W. P.; Bunz, U. H. F., 1,3-Dipolar cycloaddition for the generation of nanostructured semiconductors by heated probe tips. *Macromol.* **2006,** *39*, 6793-6795.

153. Zhou, D.; Bruckbauer, A.; Ying, L.; Abell, C.; Klenerman, D., Building Three-dimensional surface biological assemblies on the nanometer scale. *Nano Lett.* **2003,** *3*, 1517-1520.

154. Shi, J.; Chen, J.; Cremer, P. S., Sub-100 nm patterning of supported bilayers by nanoshaving lithography. *J. Am. Chem. Soc.* **2008,** *130*, 2718-2719.

155. Jang, C.-H.; Stevens, B. D.; Carlier, P. R.; Calter, M. A.; Ducker, W. A., Immobilized enzymes as catalytically-active tools for nanofabrication. *J. Am. Chem. Soc.* **2002,** *124*, 12114-12115.

156. Liang, J.; Rosa, L. G.; Scoles, G., Nanostructuring, imaging and molecular manipulation of dithiol monolayers on Au(111) Surfaces by atomic force microscopy. *J. Phys. Chem. C* **2007,** *111*, 17275-17284.

157. Liu, M.; Amro, N. A.; Liu, G.-Y., Nanografting for surface physical chemistry *Annu. Rev. Phys. Chem.* **2008,** *59*, 367-386.

158. Brower, T. L.; Garno, J. C.; Ulman, A.; Liu, G. Y.; Yan, C.; Golzhauser, A.; Grunze, M., Self-assembled multilayers of 4,4 '-dimercaptobiphenyl formed by Cu(II)-catalyzed oxidation. *Langmuir* **2002,** *18* (16), 6207-6216.

159. Xiao, X. D.; Liu, G.-Y.; Charych, D. H.; Salmeron, M., Preparation, structure and mechanical stability of alkylsilane monolayers on mica. *Langmuir* **1995,** *11* (5), 1600-1604.

160. Liu, G. Y.; Salmeron, M., Reversible displacement of chemisorbed n-alkanethiol molecules on Au(111) surface:an atomic force microscopy study. *Langmuir* **1994,** *10* (2), 367-370.

161. Xiao, X. D.; Liu, G. Y.; Charych, D. H.; Salmeron, M., Preparation, structure, and mechanical stability of alkylsilane monolayers on mica. *Langmuir* **1995,** *11* (5), 1600-1604.

162. Milic, T.; Garno, J. C.; Batteas, J. D.; Smeureanu, G.; Drain, C. M., Self-organization of self-assembled tetrameric porphyrin arrays on surfaces. *Langmuir* **2004,** *20* (10), 3974-3983.

163. Headrick, J. E.; Armstrong, M.; Cratty, J.; Hammond, S.; Sheriff, B. A.; Berrie, C. L., Nanoscale patterning of alkyl monolayers on silicon using the atomic force microscope. *Langmuir* **2005,** *21* (9), 4117-4122.

164. Jourdan, J. S.; Cruchon-Dupeyrat, S. J.; Huan, Y.; Kuo, P. K.; Liu, G.-Y., Imaging nanoscopic elasticity of thin film materials by atomic force microscopy: Effects of force modulation frequency and amplitude. *Langmuir* **1999,** *15* (19), 6495-6504.

165. Chwang, A. B.; Granstrom, E. L.; Frisbie, C. D., Fabrication of a sexithiophene semiconducting wire: Nanoshaving with an atomic force microscope tip. *Adv. Mater.* **2000,** *12* (4), 285-288.

166. Brower, T. L.; Garno, J. C.; Ulman, A.; Liu, G.-Y.; Yan, C.; Golzhauser, A.; Grunze, M., Self-assembled multilayers of 4,4 '-dimercaptobiphenyl formed by Cu(II)-catalyzed oxidation. *Langmuir* **2002,** *18* (16), 6207-6216.

167. Zhou, D.; Bruckbauer, A.; Ying, L. M.; Abell, C.; Klenerman, D., Building three-dimensional surface biological assemblies on the nanometer scale. *Nano Lett.* **2003,** *3* (11), 1517-1520.

168. Garno, J. C.; Yang, Y.; Amro, N. A.; Cruchon-Dupeyrat, S.; Chen, S.; Liu, G.-Y., Precise positioning of nanoparticles on surfaces using scanning probe lithography. *Nano Lett.* **2003,** *3*, 389-395

169. Hansma, H. G.; Vesenka, J.; Siegerist, C.; Kelderman, G.; Morrett, H.; Sinsheimer, R. L.; Elings, V.; Bustamante, C.; Hansma, P. K., Reproducible imaging and dissection of plasmid dna under liquid with the atomic force microscope. *Science* **1992,** *256*, 1180-1184.

170. Weisenhorn, A. L.; Maivald, P.; Butt, H. J.; Hansma, P. K., Measuring adhesion, attraction, and repulsion between surfaces in liquids with an atomic-force microscope. *Phys. Rev. B.* **1992,** *45*, 11226-11232.

171. Xu, S.; Laibinis, P. E.; Liu, G.-Y., Accelerating the kinetics of thiol self-assembly on gold - a spatial confinement effect. *J. Am. Chem. Soc.* **1998,** *120* (36), 9356-9361.

172. Ryu, S.; Schatz, G., Nanografting: modeling and simulation. *J. Am. Chem. Soc* **2006,** *128* (35), 11563-11573.

173. Rugar, D.; Yannoni, C. S.; Sidles, J. A., Mechanical detection of magnetic-resonance. *Nature* **1992,** *360* (6404), 563-566.

174. Sidles, J. A.; Garbini, J. L.; Bruland, K. J.; Rugar, D.; Zuger, O.; Hoen, S.; Yannoni, C. S., Magnetic-resonance force microscopy. *Rev. Mod. Phys.* **1995,** *67* (1), 249-265.

175. Zhang, Z.; Hammel, P. C.; Wigen, P. E., Observation of ferromagnetic resonance in a microscopic sample using magnetic resonance force microscopy. *Appl. Phys. Lett.* **1996,** *68* (14), 2005-2007.

176. Rugar, D.; Budakian, R.; Mamin, H. J.; Chui, B. W., Single spin detection by magnetic resonance force microscopy. *Nature* **2004,** *430* (6997), 329-332.

177. Florin, E. L.; Radmacher, M.; Fleck, B.; Gaub, H. E., Atomic-force microscope with magnetic force modulation. *Rev. Sci. Instrum.* **1994,** *65* (3), 639-643.

178. Yamamoto, S.; Yamada, H., Interpretation of direct and indirect force modulation methods using polymer films. *Langmuir* **1997,** *13* (18), 4861-4864.

179. Schemmel, A.; Gaub, H. E., Single molecule force spectrometer with magnetic force control and inductive detection. *Rev. Sci. Instrum.* **1999,** *70* (2), 1313-1317.

180. Scherer, M. P.; Gummer, A. W., Impedance analysis of the organ of corti with magnetically actuated probes. *Biophys. J.* **2004,** *87* (2), 1378-1391.

181. Kelley, A. T.; Daniels, S. L.; Serem, W.; Lusker, K.; Flurry, N.; Okudzeto, E.; Chan, J. Y.; Garno, J. C., Microwave synthesis and AFM characterization of iron(III) nickel nanoparticles. *Chem. Mater., In preparation* **2009**.

182. Love, J. C.; Estroff, L. A.; Kriebel, J. K.; Nuzzo, R. G.; Whitesides, G. M., Self-assembled monolayers of thiolates on metals as a form of nanotechnology. *Chem. Rev.* **2005,** *105*, 1103-1169.

183. Schreiber, F., Structure and growth of self-assembling monolayers. *Prog. Surf. Sci.* **2000,** *65*, 151-256.

184. Ulman, A., Formation and structure of self-assembled monolayers. *Chem. Rev.* **1996,** *96*, 1533-1554.

185. Bain, C. D.; Whitesides, G. M., Formation of monolayers by the coadsorption of thiols on gold - variation in the length of the alkyl chain. *J. Am. Chem. Soc.* **1989,** *111*, 7164-7175.

186. Bain, C. D.; Evall, J.; Whitesides, G. M., Formation of monolayers by the coadsorption of thiols on gold - variation in the head group, tail group, and solvent. *J. Am. Chem. Soc.* **1989,** *111*, 7155-7164.

187. Folkers, J. P.; Laibinis, P. E.; Whitesides, G. M., Self-assembled monolayers of alkanethiols on gold - comparisons of monolayers containing mixtures of short-chain and long-chain constituents with ch3 and ch2oh terminal groups. *Langmuir* **1992,** *8*, 1330-1341.

188. Kakiuchi, T.; Iida, M.; Gon, N.; Hobara, D.; Imabayashi, S.-i.; Niki, K., Miscibility of adsorbed 1-undecanethiol and 11-mercaptoundecanoic acid species in binary self-assembled monolayers on Au(111). *Langmuir* **2001,** *17*, 1599-1603.

189. Hobara, D.; Ota, M.; Imabayashi, S.; Niki, K.; Kakiuchi, T., Phase separation of binary self-assembled thiol monolayers composed of 1-hexadecanethiol and 3-mercaptopropionic acid on Au(111) studied by scanning tunneling microscopy and cyclic voltammetry. *J. Electroanal. Chem* **1998,** *444*, 113-119.

190. Kakiuchi, T.; Sato, K.; Lida, M.; Hobara, D.; Imabayashi, S.; Niki, K., Phase Separation of Alkanethiol Self-Assembled Monolayers during the Replacement of Adsorbed Thiolates on Au(111) with Thiols in Solution *Langmuir* **2000,** *16*, 7238-7244.

191. Chen, S. F.; Li, L. Y.; Boozer, C. L.; Jiang, S. Y., controlled chemical and structural properties of mixed self-assembled monolayers by coadsorption of symmetric and asymmetric disulfides on Au(111). *J. Phys. Chem. B* **2001,** *105*, 2975-2980.

192. Klein, H.; Battaglini, N.; Bellini, B.; Dumas, P., STM of mixed alkylthiol self-assembled monolayers on Au(111). *Mater. Sci. Eng., C* **2002,** *19*, 279-283.

193. Stranick, S. J.; Parikh, A. N.; Tao, Y. T.; Allara, D. L.; Weiss, P. S., Phase-separation of mixed-composition self-assembled monolayers into nanometer-scale molecular domains. *J. Phys. Chem.* **1994,** *98*, 7636-7646.

194. Smith, R. K.; Lewis, P. A.; Weiss, P. S., Patterning self-assembled monolayers. *Prog. Surf. Sci.* **2004,** *75*, 1-68.

195. Xia, Y. N.; Rogers, J. A.; Paul, K. E.; Whitesides, G. M., Unconventional methods for fabricating and patterning nanostructures. *Chem. Rev.* **1999,** *99*, 1823-1848.

196. Laibinis, P. E.; Whitesides, G. M., Self-assembled monolayers of n-alkanethiolates on copper are barrier films that protect the metal against oxidation by air. *J. Am. Chem. Soc.* **1992,** *114*, 9022-9028.

197. Whitesides, G. M.; Laibinis, P. E., Wet chemical approaches to the characterization of organic-surfaces - self-assembled monolayers, wetting, and the physical organic-chemistry of the solid liquid interface. *Langmuir* **1990,** *6*, 87-96.

198. Schreiber, F., Self-assembled monolayers: from "simple" model systems to biofunctionalized interfaces. *J. Phys. Condens. Matter* **2004,** *16*, R881-900.

199. Willner, I.; Katz, E., Integration of layered redox proteins and conductive supports for bioelectronic applications. *Angew. Chem. Int. Ed.* **2000,** *39*, 1180-1218.

200. Flink, S.; Van Veggel, F.; Reinhoudt, D. N., Sensor functionalities in self-assembled monolayers. *Adv. Mater.* **2000,** *12*, 1315-1328.

201. Crooks, R. M.; Ricco, A. J., New organic materials suitable for use in chemical sensor arrays. *Acc. Chem. Res.* **1998,** *31*, 219.

202. Dimilla, P. A.; Folkers, J. P.; Biebuyck, H. A.; Harter, R.; Lopez, G. P.; Whitesides, G. M., Wetting and protein adsorption of self-assembled monolayers of alkanethiolates supported on transparent films of gold. *J. Am. Chem. Soc.* **1994,** *116*, 2225-2226.

203. Chidsey, C. E. D.; Loiacono, D. N., Chemical functionality in self-assembled monolayers - structural and electrochemical properties. *Langmuir* **1990,** *6*, 682-691.

204. Troughton, E. B.; Bain, C. D.; Whitesides, G. M.; Nuzzo, R. G.; Allara, D. L.; Porter, M. D., Monolayer films prepared by the spontaneous self-assembly of symmetrical and unsymmetrical dialkyl sulfides from solution onto gold substrates - Structure, properties, and reactivity of constituent functional-groups. *Langmuir* **1988,** *4*, 365-385.

205. Bain, C. D.; Troughton, E. B.; Tao, Y. T.; Evall, J.; Whitesides, G. M.; Nuzzo, R. G., Formation of monolayer films by the spontaneous assembly of organic thiols from solution onto gold. *J. Am. Chem. Soc.* **1989,** *111*, 321-335.

206. Fenter, P.; Eberhardt, A.; Eisenberger, P., Self-assembly of n-alkyl thiols as disulfides on Au(111). *Science* **1994,** *266*, 1216-1218.

207. Nuzzo, R. G.; Zegarski, B. R.; Dubois, L. H., fundamental-studies of the chemisorption of organosulfur compounds on Au(111) - Implications for molecular self-assembly on gold surfaces. *J. Am. Chem. Soc.* **1987,** *109*, 733-740.

208. Joachim, C.; Gimzewski, J. K.; Aviram, A., Electronics using hybrid-molecular and mono-molecular devices. *Nature* **2000,** *408*, 541-548.

209. Tour, J. M., Molecular electronics. Synthesis and testing of components. *Acc. Chem. Res.* **2000,** *33*, 791-804.

210. Poirier, G. E., Characterization of organosulfur molecular monolayers on Au(111) using scanning tunneling microscopy. *Chem. Rev.* **1997,** *97*, 1117-1127.

211. Liu, G. Y.; Xu, S.; Qian, Y. L., Nanofabrication of self-assembled monolayers using scanning probe lithography. *Acc. Chem. Res.* **2000,** *33*, 457-466.

212. Liu, M.; Amro, N. A.; Liu, G.-Y., Nanografting for Surface Physical Chemistry. *Annu. Rev. Phys. Chem.* **2008,** *59*, 367-386.

213. Amro, N. A.; Xu, S.; Liu, G.-Y., Patterning surfaces using tip-directed displacement and self-assembly. *Langmuir* **2000,** *16*, 3006-3009.

214. Piner, R. D.; Zhu, J.; Xu, F.; Hong, S.; Mirkin, C. A., Dip pen nanolithography. *Science* **1999,** *283*, 661-663.

215. Whitesides, G. M.; Ostuni, E.; Takayama, S.; Jiang, X. Y.; Ingber, D. E., Soft lithography in biology and biochemistry. *Annu. Rev. Biomed. Eng.* **2001,** *3*, 335-373.

216. Xia, Y. N.; Whitesides, G. M., Soft lithography *Annu. Rev. Mater. Sci.* **1998,** *28*, 153-184.

217. Quist, A. P.; Pavlovic, E.; Oscarsson, S., Recent advances in microcontact printing. *Anal. Bioanal. Chem.* **2005,** *381*, 591-600.

218. Xia, Y. N.; Zhao, X. M.; Whitesides, G. M., Pattern transfer: Self-assembled monolayers as ultrathin resists. *Microelectron. Eng.* **1996,** *32*, 255-268.

219. Zhao, X. M.; Xia, Y. N.; Whitesides, G. M., Soft lithographic methods for nano-fabrication. *J. Mater. Chem.* **1997,** *7*, 1069-1074.

220. Sugimura, H.; Ushiyama, K.; Hozumi, A.; Takai, O., Micropatterning of alkyl- and fluoroalkylsilane self-assembled monolayers using vacuum ultraviolet light. *Langmuir* **2000,** *16*, 885-888.

221. Xu, S.; Miller, S.; Laibinis, P. E.; Liu, G. Y., Fabrication of nanometer scale patterns within self-assembled monolayers by nanografting. *Langmuir* **1999,** *15*, 7244-7251.

222. Xu, S.; Laibinis, P. E.; Liu, G. Y., Accelerating the kinetics of thiol self-assembly on gold - A spatial confinement effect. *J. Am. Chem. Soc.* **1998,** *120*, 9356-9361.

223. Porter, M. D.; Bright, T. B.; Allara, D. L.; Chidsey, C. E. D., Spontaneously organized molecular assemblies .4. Structural characterization of normal-alkyl thiol monolayers on gold by

optical ellipsometry, infrared-spectroscopy and electrochemistry. *J. Am. Chem. Soc.* **1987,** *109*, 3559-3568.

224. Lavrich, D. J.; Wetterer, S. M.; Bernasek, S. L.; Scoles, G., Physisorption and chemisorption of alkanethiols and alkyl sulfides on Au(111). *J. Phys. Chem. B* **1998,** *102*, 3456-3465.

225. Nuzzo, R. G.; Korenic, E. M.; Dubois, L. H., Studies of the temperature-dependent phase-behavior of long-chain normal-alkyl thiol monolayers on gold. *J. Chem. Phys.* **1990,** *93*, 767-773.

226. Fenter, P.; Eisenberger, P.; Liang, K. S., Chain-length dependence of the structures and phases of $CH_3(CH_2)$N-1SH self-assembled on Au(111). *Phys. Rev. Lett.* **1993,** *70*, 2447-2450.

227. Dannenberger, O.; Weiss, K.; Himmel, H. J.; Jager, B.; Buck, M.; Woll, C., An orientation analysis of differently endgroup-functionalised alkanethiols adsorbed on Au substrates. *Thin Solid Films* **1997,** *307*, 183-191.

228. Poirier, G. E.; Pylant, E. D.; White, J. M., Crystalline structures of pristine and hydrated mercaptohexanol self-assembled monolayers on Au(111) *J. Chem. Phys.* **1996,** *105*, 2089-2092.

229. Riposan, A.; Li, Y.; Tan, Y. H.; Galli, G.; Liu, G.-Y., Structural characterization of aldehyde-terminated self-assembled monolayers. *J. Phys. Chem. A* **2007,** *111*, 12727-12739.

230. Fendler, J. H., Chemical self-assembly for electronic applications. *Chem. Mater.* **2001,** *13*, 3196-3210.

231. Willey, T.; Vance, A.; Fadley, C. S., Rapid degradation of alkanethiol-based self-assembled monolayers on gold in ambient laboratory conditions. *Surf. Sci.* **2005,** *567*, 188-196.

232. Cruchon-Dupeyrat, S. J. N.; Porthun, S.; Liu, G.-Y., Nanofabrication using computer-assisted design and automated vector-scanning probe lithography. *Appl. Surf. Sci.* **2001,** *175-176*, 636-642.

233. Klapetek, P. N. *http://gwyddion.net/*, Czech Metrology Institute: Czech Republic, 2007.

234. Hacker, C. A.; Batteas, J. D.; Garno, J. C.; Marquez, M.; Richter, C. A.; Richter, L. J.; vanZee, R. D.; Zangmeister, C. D., Structural and Chemical characterization of monofluoro-substituted oligo(phenylene-ethynylene) thiolate self-assembled monolayers on Gold. *Langmuir* **2004,** *20*, 6195-6205.

235. Mendoza, S. M.; Arfaoui, I.; Zanarini, S.; Paolucci, F.; Rudolf, P., Improvements in the characterization of the crystalline structure of acid-terminated alkanethiol self-assembled monolayers on Au(111). *Langmuir* **2007,** *23*, 582-588.

236. Cheng, Q.; Brajter-Toth, A., Permselectivity and high sensitivity at ultrathin monolayers. effect of film hydrophobicity. *Anal. Chem.* **1995,** *67*, 2767-2775.

237. Pflaum, J.; Bracco, G.; Schreiber, F.; Colorado, R.; Shmakova, O. E.; Lee, T. R.; Scoles, G.; Kahn, A., Structure and electronic properties of CH3- and CF3-terminated alkanethiol

monolayers on Au(111): a scanning tunneling microscopy, surface X-ray and helium scattering study. *Surf. Sci.* **2002,** *498*, 89-104.

238. Godin, M.; Williams, P. J.; Tabard-Cossa, V.; Laroche, O.; Beaulieu, L. Y.; Lennox, R. B.; Grutter, P., Surface stress, kinetics, and structure of alkanethiol self-assembled monolayers. *Langmuir* **2004,** *20*, 7090-7096.

239. Yang, G.; Amro, N. A.; Starkewolfe, Z. B.; Liu, G.-Y., Molecular-level approach to inhibit degradations of alkanethiol self-assembled monolayers in aqueous media. *Langmuir* **2004,** *20*, 3995-4003.

240. Garno, J. C.; Zangmeister, C. D.; Batteas, J. D., Directed electroless growth of metal nanostructures on patterned self-assembled monolayers. *Langmuir* **2007,** *23*, 7874-7879.

241. Zhou, D.; Wang, X.; Birch, L.; Rayment, T.; Abell, C., AFM study on protein immobilization on charged surfaces at the nanoscale: toward the fabrication of three-dimensional protein nanostructures. *Langmuir* **2003,** *19*, 10557-10562.

242. Tao, F.; Goswami, J.; Bernasek, S. L., Self-assembly and odd-even effects of cis-unsaturated carboxylic acids on highly oriented pyrolytic graphite. *J. Phys. Chem. B* **2006,** *110*, 4199-4206.

243. Bilgili, E.; Hamey, R.; Scarlett, B., Nano-milling of pigment agglomerates using a wet stiffed media mill: Elucidation of the kinetics and breakage mechanisms. *Chem. Eng. Sci* **2006,** *61*, 149-157.

244. Horn, D.; Rieger, J., Organic nanoparticles in the aqueous phase - theory, experiment, and use. *Angew. Chem.-Int. Edit.* **2001,** *40* (23), 4331-4361.

245. Mendel, J.; Bugner, D.; Bermel, A. D., Particle generation and ink particle size effects in pigmented inkjet inks – part II. *J. Nanopart. Res.* **1999,** *1* (3), 421-424.

246. Zheng, T. H.; Choy, W. C. H.; Sun, Y. X., Nanoparticle-induced resonant tunneling behaviors in small molecule organic light-emitting devices. *Appl. Phys. Lett.* **2009,** *94* (12), 3.

247. Carotenuto, G.; Her, Y. S.; Matijevic, E., Preparation and characterization of nanocomposite thin films for optical devices. *Ind. Eng. Chem. Res.* **1996,** *35* (9), 2929-2932.

248. Qu, D.; Duncan, J. W., Study on pigment dispersion in color cosmetics: Milling process and scale-up. *J. Cosmet. Sci.* **2000,** *51*, 323-341.

249. Baez, E.; Quazi, N.; Ivanov, I.; Bhattacharya, S. N., Stability study of nanopigment dispersions. *Adv. Powder Technol.* **2009,** *20* (3), 267-272.

250. Fu, S. H.; Fang, K. J., Preparation of ultrafine pigment dispersion and effect on xi-potentials. *J. Dispersion Sci. Technol.* **2006,** *27* (7), 971-974.

251. Hao, Z. M.; Iqbal, A., Some aspects of organic pigments. *Chem. Soc. Rev.* **1997,** *26* (3), 203-213.

252. Haq, I.; Fraser, I.; Matijevic, E., Preparation and characterization of finely dispersed pigment particles. *Colloid Polym. Sci.* **2003,** *281* (6), 542-549.

253. Hong, L.; Guo, J.; Gao, Y.; Yuan, W.-K., Precipitation of Microparticulate organic pigment powders by a supercritical antisolvent process. *Ind. Eng. Chem. Res.* **2000,** *39* (12), 4882-4887.

254. Ishibashi, M.; Hotta, Y.; Ushirogochi, T.; Akiyama, R.; Kawakami, Y.; Ohtsu, K.; Kiyomoto, H.; Tanuma, C., Nano-stabilized photo-curable inkjet ink for printing and printable electronics. *J. Photopolym Sci. Technol.* **2006,** *19* (5), 653-656.

255. Mukhopadhyay, P.; Desbaumes, L.; Schreiber, H. P.; Hor, A. M.; DipaolaBaranyi, G., Component interactions and the stability of some pigment/polymer dispersions. *J. Appl. Polym. Sci.* **1998,** *67* (2), 245-253.

256. Van, S. T.; Velamakanni, B. V.; Adkins, R. R., Comparison of methods to assess pigment dispersion. *J. Coat. Technol.* **2001,** *73*, 61-70.

257. Widiyandari, H.; Iskandar, F.; Hagura, N.; Okuyarna, K., Preparation and characterization of nanopigment-poly(styrene-co-n-butyl acrylate-co-methacrylic acid) composite particles by high speed homogenization-assisted suspension polymerization. *J. Appl. Polym. Sci.* **2008,** *108* (2), 1288-1297.

258. Grubenmann, A., Particle size distribution and aspect ratio of organic pigments. *Part. Part. Syst. Char.* **1986,** *3* (4), 179-186.

259. Spinelli, H. J., Polymeric dispersants in ink jet technology. *Adv. Mater.* **1998,** *10* (15), 1215-218

260. Maikowski, M., Effect of colloidal distribution states on the normal properties of organic pigments *Prog. Colloid Polym. Sci.* **1976,** *59*, 70-81.

261. Cheng, W. T.; Hsu, C. W.; Chih, Y. W., Dispersion of organic pigments using supercritical carbon dioxide. *J. Colloid Interface Sci.* **2004,** *270* (1), 106-112.

262. Bilgili, E.; Hamey, R.; Scarlett, B., Production of pigment nanoparticles using a wet stirred mill with polymeric media. *China Particuology* **2004,** *2* (3), 93-100.

263. Chang, C. J.; Chang, S. J.; Tsou, S.; Chen, S. I.; Wu, F. M.; Hsu, M. W., Effects of polymeric dispersants and surfactants on the dispersing stability and high-speed-jetting properties of aqueous-pigment-based ink-jet inks. *J. Polym. Sci. Pt. B-Polym. Phys.* **2003,** *41* (16), 1909-1920.

264. Schoff, C. K., Organic coatings: the paradoxical materials. *Prog. Org. Coat.* **2005,** *52*, 21-27.

265. Schofield, J. D., Extending the boundaries of dispersant technology. *Prog. Org. Coat.* **2002,** *45* (2-3), 249-257.

266. Tsubokawa, N.; Kobayashi, M.; Ogasawara, T., Graft polymerization of vinyl monomers initiated by azo groups introduced onto organic pigment surface. *Prog. Org. Coat.* **1999,** *36* (1-2), 39-44.

267. Zhang, T. Y.; Fei, X. N.; Wang, S. R.; Zhou, C. L., Pigmentation of Vat Blue RS by ball milling in solvents. *Dyes Pigm.* **2000,** *45* (1), 15-21.

268. Subra, P.; Jestin, P., Powders elaboration in supercritical media: comparison with conventional routes. *Powder Technol.* **1999,** *103* (1), 2-9.

269. Hayashi, K.; Morii, H.; Iwasaki, K.; Horie, S.; Horiishi, N.; Ichimura, K., Uniformed nano-downsizing of organic pigments through core-shell structuring. *J. Mater. Chem.* **2007,** *17* (6), 527-530.

270. Horiuchi, S.; Horie, S.; Ichimura, K., Coreâ^'Shell structures of silicaâ^'organic pigment nanohybrids visualized by electron spectroscopic imaging. *ACS Appl. Mat. Interfaces* **2009,** *1* (5), 977-981.

271. Park, J. W.; Ullah, M. H.; Park, S. S.; Ha, C. S., Organic electroluminescent devices using quantum-size silver nanoparticles. *J. Mater. Sci - Mater. Electron.* **2007,** *18*, S393-S397.

272. Sun, C. J.; Wu, Y.; Xu, Z. H.; Hu, B.; Bai, J. M.; Wang, J. P.; Shen, J., Enhancement of quantum efficiency of organic light emitting devices by doping magnetic nanoparticles. *Appl. Phys. Lett.* **2007,** *90* (23), 3.

273. Mayer, T.; Weiler, U.; Kelting, C.; Schlettwein, D.; Makarov, S.; Wöhrle, D.; Abdallah, O.; Kunst, M.; Jaegermann, W., Silicon-organic pigment material hybrids for photovoltaic application. *Sol. Energy Mater. Sol. Cells* **2007,** *91* (20), 1873-1886.

274. Barth, H., G., *Modern Methods of Particle Size Analysis*. John Wiley & Sons: New York, 1984; Vol. 74.

275. Hyeon, T., Chemical synthesis of magnetic nanoparticles. *Chem. Commun.* **2003,** (8), 927-934.

276. Darling, S. B.; Bader, S. D., A materials chemistry perspective on nanomagnetism. *Journal of Materials Chemistry* **2005,** *15* (39), 4189-4195.

277. Terris, B. D.; Thomson, T., Nanofabricated and self-assembled magnetic structures as data storage media. *J. Phys. D: Appl. Phys.* **2005,** *38* (12), R199-R222.

278. Roger, J.; Pons, J. N.; Massart, R.; Halbreich, A.; Bacri, J. C., Some biomedical applications of ferrofluids. *Eur. Phys. J. Appl. Phys* **1999,** *5*, 321-325.

279. Shen, L.; Laibinis, P. E.; Hatton, T. A., Bilayer surfactant stabilized magnetic fluids: synthesis and interactions at interfaces. *Langmuir* **1998,** *15* (2), 447-453.

280. Sousa, M. H.; Tourinho, F. A.; Depeyrot, J.; da Silva, G. J.; Lara, M. C. F. L., New electric double-layered magnetic fluids based on copper, nickel, and zinc ferrite nanostructures. *J. Phys. Chem. B* **2001,** *105* (6), 1168-1175.

281. Morup, S., Superferromagnetic nanostructures. *Hyperfine Interactions* **1994,** *90*, 171-185.

282. Mornet, S.; Vasseur, S.; Grasset, F.; Duguet, E., Magnetic nanoparticle design for medical diagnosis and therapy. *J. Mater. Chem.* **2004,** *14* (14), 2161-2175.

283. Pankhurst, Q. A.; Connolly, J.; Jones, S. K.; Dobson, J., Applications of magnetic nanoparticles in biomedicine. *J. Phys. D: Appl. Phys.* **2003,** *36* (13), R167-R181.

284. Wang, Y. X. J.; Hussain, S. M.; Krestin, G. P., Superparamagnetic iron oxide contrast agents: physicochemical characteristics and applications in MR imaging. *Eur. Radiol.* **2001,** *11* (11), 2319-2331.

285. Chang, E.; Chalikonda, S.; Friedl, J.; Xu, H.; Phan, G. Q.; Marincola, F. M.; Alexander, H. R.; Bartlett, D. L., Targeting vaccinia to solid tumors with local hyperthermia. *Human Gene Therapy* **2005,** *16* (4), 435-444.

286. Ito, A.; Shinkai, M.; Honda, H.; Yoshikawa, K.; Saga, S.; Wakabayashi, T.; Yoshida, J.; Kobayashi, T., Heat shock protein 70 expression induces antitumor immunity during intracellular hyperthermia using magnetite nanoparticles. *Cancer Immunology Immunotherapy* **2003,** *52* (2), 80-88.

287. Latham, A. H.; Williams, M. E., Controlling transport and chemical functionality of magnetic nanoparticles. *Acc. Chem. Res.* **2008,** *41* (3), 411-420.

288. Berry, C. C.; Curtis, A. S. G., Functionalisation of magnetic nanoparticles for applications in biomedicine. *J. Phys. D: Appl. Phys.* **2003,** *36* (13), R198-R206.

289. Iglesias, O.; Batlle, X.; Labarta, A., Particle size and cooling field dependence of exchange bias in core/shell magnetic nanoparticles. *J. Phys. D: Appl. Phys.* **2008,** *41*, 1-5.

290. Gibbs, M. R. J., Nanomagnetism - nascent or fully formed? *Curr. Opin. Solid State Mater. Sci* **2003,** *7* (2), 83-86.

291. Lu, A. H.; Salabas, E. L.; Schuth, F., Magnetic nanoparticles: Synthesis, protection, functionalization, and application. *Angew. Chem.-Int. Edit.* **2007,** *46* (8), 1222-1244.

292. Kodama, R. H., Magnetic nanoparticles. *J. Magn. Magn. Mater.* **1999,** *200* (1-3), 359-372.

293. Respaud, M.; Broto, J. M.; Rakoto, H.; Fert, A. R.; Thomas, L.; Barbara, B.; Verelst, M.; Snoeck, E.; Lecante, P.; Mosset, A.; Osuna, J.; Ely, T. O.; Amiens, C.; Chaudret, B., Surface effects on the magnetic properties of ultrafine cobalt particles. *Phys. Rev. B* **1998,** *57* (5), 2925-2935.

294. Datta, A.; Pal, M.; Chakravorty, D.; Das, D.; Chintalapudi, S. N., Disorder in nanocrystalline Ni3Fe. *J. Magn. Magn. Mater.* **1999,** *205* (2-3), 301-306.

295. Li, X. G.; Chiba, A.; Takahashi, S., Preparation and magnetic properties of ultrafine particles of Fe-Ni alloys. *J. Magn. Magn. Mater.* **1997,** *170* (3), 339-345.

296. Liao, Q. L.; Tannenbaum, R.; Wang, Z. L., Synthesis of FeNi3 alloyed nanoparticles by hydrothermal reduction. *J. Phys. Chem. B* **2006,** *110* (29), 14262-14265.

297. Skumryev, V.; Stoyanov, S.; Zhang, Y.; Hadjipanayis, G.; Givord, D.; Nogues, J., Beating the superparamagnetic limit with exchange bias. *Nature* **2003,** *423* (6942), 850-853.

298. Xiao, J. Q.; Jiang, J. S.; Chien, C. L., Giant magnetoresistance in nonmultilayer magnetic systems. *Phys. Rev. Lett.* **1992,** *68* (25), 3749-3752.

299. Cushing, B. L.; Kolesnichenko, V. L.; O'Connor, C. J., Recent advances in the liquid-phase syntheses of inorganic nanoparticles. *Chem. Rev.* **2004,** *104* (9), 3893-3946.

300. Dahl, J. A.; Maddux, B. L. S.; Hutchison, J. E., Toward greener nanosynthesis. *Chem. Rev.* **2007,** *107* (6), 2228-2269.

301. Gerbec, J. A.; Magana, D.; Washington, A.; Strouse, G. F., Microwave-enhanced reaction rates for nanoparticle synthesis. *J. Am. Chem. Soc.* **2005,** *127* (45), 15791-15800.

302. Glaspell, G.; Fuoco, L.; El-Shall, M. S., Microwave synthesis of supported Au and Pd nanoparticle catalysts for CO oxidation. *J. Phys. Chem. B* **2005,** *109* (37), 17350-17355.

303. Lidstrom, P.; Tierney, J.; Wathey, B.; Westman, J., Microwave assisted organic synthesis - a review. *Tetrahedron* **2001,** *57* (45), 9225-9283.

304. Liu, F. K.; Huang, P. W.; Chang, Y. C.; Ko, C. J.; Ko, F. H.; Chu, T. C., Formation of silver nanorods by microwave heating in the presence of gold seeds. *J. Cryst. Growth* **2005,** *273* (3-4), 439-445.

305. Perreux, L.; Loupy, A., A tentative rationalization of microwave effects in organic synthesis according to the reaction medium, and mechanistic considerations. *Tetrahedron* **2001,** *57* (45), 9199-9223.

306. Tsuji, M.; Hashimoto, M.; Nishizawa, Y.; Kubokawa, M.; Tsuji, T., Microwave-assisted synthesis of metallic nanostructures in solution. *Chem. Eur. J.* **2005,** *11* (2), 440-452.

307. Zhu, Y. J.; Wang, W. W.; Qi, R. J.; Hu, X. L., Microwave-assisted synthesis of single-crystalline tellurium nanorods and nanowires in ionic liquids. *Angew. Chem. Int. Ed.* **2004,** *43* (11), 1410-1414.

308. Kelley, A. T.; Alessie, P.; Fornalik, J. E.; Bessey, P. G.; Garno, J. C.; Royster, T. L., Investigation and Application of Nanoparticle Dispersions of Pigment Yellow 185 using Organic Solvents. *ACS Appl. Mater. Interfaces* **2009,** *submitted*.

309. Daniels, S. L.; Ngunjiri, J. N.; Garno, J. C., Investigation of the magnetic properties of ferritin by AFM imaging with magnetic sample modulation. *Anal. Bioanal. Chem.* **2009,** *394*, 215-223.

310. http://gwyddion.net/download.php#stable-windows, **2007**.

311. Li, J.-R.; Lewandowski, B. R.; Xu, S.; Garno, J. C., Detecting the Magnetic Response of Iron Oxide Capped Organosilane Nanostructures Using Magnetic Sample Modulation and Atomic Force Microscopy. *Anal. Chem.* **2009,** *81*, 4792-4802.

312. Daniels, S. L.; Ngunjiri, J. N.; Garno, J. C., Investigation of the magnetic properties of ferritin by AFM imaging with magnetic sample modulation. *Anal. Bioanal. Chem.* **2009,** *394*, 215-223.

313. Kelley, A. T.; Ngunjiri, J. N.; Lawrence, S. O.; Crowe, W.; Garno, J. C., In situ AFM investigation of the effects of concentration and head groups when nanografting ω-functionalized n-alkanethiols. *Langmuir, accepted pending minor revision* **2009**.

314. Xu, S.; Miller, S.; Laibinis, P. E.; Liu, G.-Y., Fabrication of nanometer scale patterns within self-assembled monolayers by nanografting. *Langmuir* **1999,** *15*, 7244-7251.

315. Baez, E.; Quazi, N.; Ivanov, I.; Bhattacharya, S. N., Stability study of nanopigment dispersions. *Adv. Powder Technol.* **2009,** *in press*.

316. Bilgili, E.; Hamey, R.; Scarlett, B., Nano-milling of pigment agglomerates using a wet stiffed media mill: Elucidation of the kinetics and breakage mechanisms. *Chem. Eng. Sci* **2006,** *61*, 149-157.

317. Chang, C. J.; Chang, S.-J.; Tsou, S.; Chen, S.-I.; Wu, F.-M.; Hsu, M.-W., Effects of polymeric dispersants and surfactants on the dispersing stability and high-speed-jetting properties of aqueous-pigment-based ink-jet inks. *J. Polym. Sci. B-Polym. Phys.* **2003,** *41*, 1909-1920.

318. Spinelli, H. J., Polymeric dispersants in ink jet technology. *Adv. Mater.* **1998,** *10*, 1215-1218.

APPENDIX A: MICROWAVE DIGESTION OF CEREAL FOR METAL ANALYSIS

1. First, clean all of the glassware and microwave vessels with deionized water or dilute acid solutions.

2. Using a mortar and pestle, grind the cereal sample into a fine powder. Weigh ~1.0 g of sample into an OMNI vessel and record the weight of the sample to 4 significant figures.

3. **Carefully** add 10 mL of concentrated nitric acid to each microwave vessel, including the control vessel.

4. Place the vessels into the sample holder, and tightly close the lid. Next, tighten the screw attached to the sample holder first by hand and then by using a monkey wrench, until a clicking noise is heard.

5. Insert the temperature probe only into the control vessel through the top opening. **Please handle the temperature probe carefully, these are fragile and the glass sensor will break if dropped. Be extremely careful, as the probes are expensive!**

6. Place the pressure sensor probe into the vertical opening located on the control vessel. **Again, please handle with care.**

7. Place the control vessel into the microwave, and insert the temperature probe into positions within the interior of the oven as shown.

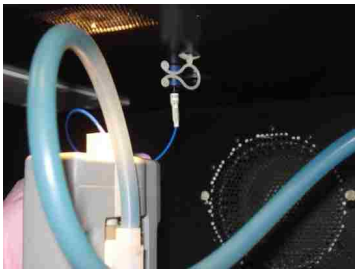

8. Next, attach the pressure probe within the oven as shown.

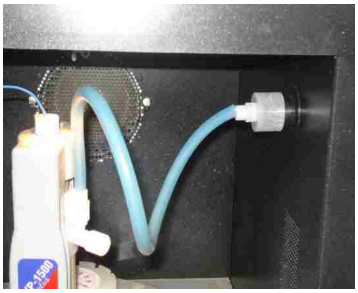

9. Place the vessels into the carousel of the microwave. Make sure the vessels are securely in place on the turntable. Note: the control vessel should be placed into the designated spot labeled 'control vessel.'

10. Close the oven door.

11. Check to see if the model numbers for the probes are correct.
    a. Choose "Set up" and select "Select Sensor."
    b. Select "Pressure Sensor," and the display should indicate **ESP-1500 Plus**.
    c. Select "Home."
    d. Select "Set up," and select "Select Sensor."
    e. Select "Temperature Sensor," which should show **RTP-300 Plus**.
    f. Check the Gauge Factor (GF number) and be sure it is the same number as shown on the package of the probe.
    g. If it is the same, click "Home;" if not, enter the correct GF number.
    h. Select "Home."

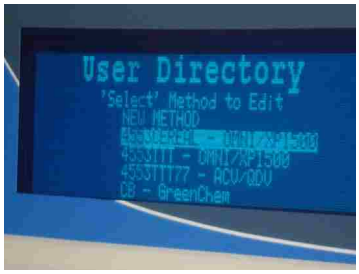

12. To start the instrument:
    a. From the menu, select "Load Method."
    b. Select "User Directory."
    c. Select "**4553Cereal**" method by using arrows.
    d. Click on Start (green arrow).

The cereal program will heat the samples at 80 C for 15 minutes at a pressure of 50 atm.

13. When the digestion is complete, let the vessels cool down until the temperature is ~50 C. Then, place the vessels into the hood.

14. Release the pressure by turning the knob on the side of the vessel very slowly. Make sure the vessel is inside the hood. **Be careful, the contents of the vessels are still under pressure**.

15. Open the vessels carefully. **Please make sure to avoid any fumes that might be released when the container lid is removed!**

16. Let the vessel cool down until it is cool to the touch (i.e. room temperature).

17. Set up the filtering system, clean the filtering vials, and place filter paper on the bottom of each vial. Obtain clean vials from storage and place them directly under the filtering vials.

18. Pour the contents of the vessels into the filtering vials, apply pressure by installing the filtering caps, and collect the sample. Bring the sample to the desired final liquid volume, e.g. 50 mLs. The sample is ready for AAS analysis.

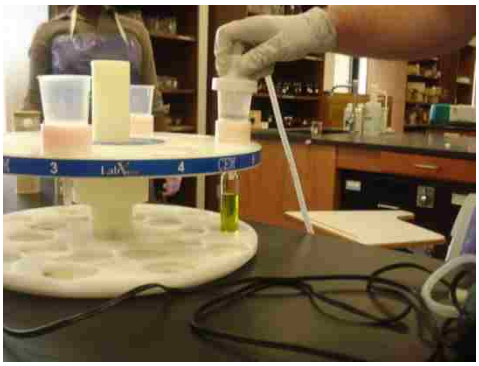

APPENDIX B: LETTERS OF PERMISSION

American Chemical Society's Policy on Theses and Dissertations

If your university requires a signed copy of this letter see contact information below.

Thank you for your request for permission to include **your** paper(s) or portions of text from **your** paper(s) in your thesis. Permission is now automatically granted; please pay special attention to the implications paragraph below. The Copyright Subcommittee of the Joint Board/Council Committees on Publications approved the following:

> Copyright permission for published and submitted material from theses and dissertations
> ACS extends blanket permission to students to include in their theses and dissertations their own articles, or portions thereof, that have been published in ACS journals or submitted to ACS journals for publication, provided that the ACS copyright credit line is noted on the appropriate page(s).
>
> Publishing implications of electronic publication of theses and dissertation material
> Students and their mentors should be aware that posting of theses and dissertation material on the Web prior to submission of material from that thesis or dissertation to an ACS journal may affect publication in that journal. Whether Web posting is considered prior publication may be evaluated on a case-by-case basis by the journal's editor. If an ACS journal editor considers Web posting to be "prior publication", the paper will not be accepted for publication in that journal. If you intend to submit your unpublished paper to ACS for publication, check with the appropriate editor prior to posting your manuscript electronically.

If your paper has **not** yet been published by ACS, we have no objection to your including the text or portions of the text in your thesis/dissertation in **print and microfilm formats**; please note, however, that electronic distribution or Web posting of the unpublished paper as part of your thesis in electronic formats might jeopardize publication of your paper by ACS. Please print the following credit line on the first page of your article: "Reproduced (or 'Reproduced in part') with permission from [JOURNAL NAME], in press (or 'submitted for publication'). Unpublished work copyright [CURRENT YEAR] American Chemical Society." Include appropriate information.

If your paper has already been published by ACS and you want to include the text or portions of the text in your thesis/dissertation in **print or microfilm formats**, please print the ACS copyright credit line on the first page of your article: "Reproduced (or 'Reproduced in part') with permission from [FULL REFERENCE CITATION.] Copyright [YEAR] American Chemical Society." Include appropriate information.

Submission to a Dissertation Distributor: If you plan to submit your thesis to UMI or to another dissertation distributor, you should not include the unpublished ACS paper in your thesis if the thesis will be disseminated electronically, until ACS has published your paper. After publication of the paper by ACS, you may release the entire thesis (**not the individual ACS article by itself**) for electronic dissemination through the distributor; ACS's copyright credit line should be printed on the first page of the ACS paper.

Use on an Intranet: The inclusion of your ACS unpublished or published manuscript is permitted in your thesis in print and microfilm formats. If ACS has published your paper you may include the manuscript in your thesis on an intranet that is not publicly available. Your ACS article cannot be posted electronically on a publicly available medium (i.e. one that is not password protected), such as but not limited to, electronic archives, Internet, library server, etc. The only material from your paper that can be posted on a public electronic medium is the article abstract, figures, and tables, and you may link to the article's DOI or post the article's author-directed URL link provided by ACS. This paragraph does not pertain to the dissertation distributor paragraph above.

Questions? Call +1 202/872-4368/4367. Send e-mail to copyright@acs.org or fax to +1 202-776-8112. 10/10/03, 01/15/04, 06/07/06

VITA

Algernon Tremayne Kelley was born in Stamford, Connecticut, in 1981 to the late Ethel Pearl Kelley-Roach and Hezekiah Roach. He graduated from Stamford High School in 1999 and was featured in Stamford's local newspaper, *The Stamford Advocate*. In addition, Algernon was named a Jackie Robinson Foundation Scholar that same year, which was sponsored by the Nike Corporation. He graduated *cum laude* from Xavier University of Louisiana with a Bachelor of Science degree in chemistry in May 2004. When he graduated, Algernon was the recipient of Xavier University's highest honor, *The Saint Katherine Drexel Award*, and he was featured in New Orleans' local newspaper, *The Times-Picayune*. In the fall of 2004, he enrolled in the doctoral program in the Department of Chemistry at Louisiana State University where he joined the research group of Dr. Jayne C. Garno. During his tenure at LSU, Algernon was lead author of three articles and co-author of five publications, with two further first-author manuscripts in preparation. He participated in international, regional, and local conferences, giving 8 oral presentations, 7 first-author poster presentations and co-authoring 10 posters. Algernon received two travel awards (Coates and Pfizer). Algernon completed a six-month internship at Eastman Kodak Company in Rochester, New York, working under the direction of Dr. Tommie L. Royster from July 2008 to January 2009. Algernon plans to pursue a career in academia where he will develop new science courses and teaching materials geared towards students who have learning disabilities.